EXPLORING ELECTRIDES AS ANION STORAGE MATERIALS

Lauren Marie McRae

A dissertation submitted to the faculty at the University of North Carolina at Chapel Hill in partial fulfillment of the requirements for the degree of Doctor of Philosophy in the Department of Chemistry.

Chapel Hill
2023

Approved by:

James F. Cahoon

Joanna M. Atkin

Yosuke Kenai

Carrie L. Donley

Scott C. Warren

© 2023
Lauren Marie McRae
ALL RIGHTS RESERVED

ABSTRACT

Lauren M. McRae: Exploring electrides as anion storage materials
(Under the direction of Scott C. Warren)

Many next-generation technologies rely on increasing the capacity of storage materials. Although lithium-ion batteries have attracted the most attention for energy storage, materials that store anions remain relatively unexplored.

Anion shuttle batteries may offer high capacity and be made from abundant materials; however, all known anion battery electrodes are conversion-based, causing short lifetimes. We propose that electrides, exotic materials that have electrons present in well-defined lattice sites rather than within atoms, could be used as intercalation-type electrodes to fill this gap. Additionally, it is widely assumed that the gain or loss of electrons in a material must be accompanied by its reduction or oxidation. Here, we report a system in which the insertion/deinsertion of an electron occurs without any reduction or oxidation.

Although all known electrides have an electropositive metal cation adjacent to the electride site, the effect of cation electronegativity on the properties of electrides is not yet known. Understanding these affects could lead to the discovery of novel electrides with higher capacities or more abundant elements than Y_2C. Therefore, we examine trivalent metal carbides with varying degrees of electronegativity and experimentally synthesize Sc_2C. Our studies identify the material as a two-dimensional (2D) electride, even though Sc is more electronegative than any metal previously found adjacent to an electride site. Further, by exploring Sc_2C and Al_2C computationally, we find that higher electronegativity of the cation drives greater hybridization between metal and electride orbitals, which opens a band gap in these materials. Sc_2C is the first 2D electride semiconductor, and we propose a design rule that cation electronegativity drives the change in its band structure.

High-capacity hydrogen storage materials may enable the use of hydrogen fuel cells in mobile applications; however, all known hydrogen storage materials are low capacity. Therefore, with the predicted high hydrogen storage capacity of 2D Sc_2C, we experimentally explore the hydrogenation of Sc_2C. We find

that reacting Sc_2C with H_2 gas creates Sc_2CH_x, and that this process might be reversible at room temperature.

It is not the answer that enlightens, but the question.

ACKNOWLEDGEMENTS

To Professor Scott Warren: Thank you for always pushing me to be a better scientist while allowing me the freedom to explore my scientific and professional goals. All of my accomplishments in these 5 years are tied back to your support and your belief in me, even when I struggled to believe in myself.

To all of my lab mates: Thank you for all of our desk conversations, science discussions, and most importantly, the laughs and friendship. I especially want to thank Dan and Jacob for their mentorship and teaching during my first few years. Thank you to Jack for all our conversations about computation and your mentorship. And lastly, thank you Becca for listening and helping me work through tough problems, and for your work on all our joint efforts.

To my longtime friends and mentors: Thank you for your support through this whole journey. You all have been in my life long before I started grad school, and have supported me every step of the way. I would not have made it here without our life talks and all of the advice I received. I especially want to thank a few people: Rachel and Benjamin – my roommates – you both are a huge reason I decided to get my Ph.D. in the first place. You are amazing scientists whom I've always wanted to emulate; I can't wait to see the way you change the world. Annie – my college roommate and chemistry buddy – you are one of my inspirations. All our Facetime dates throughout grad school and your unconditional support got me here today, and I'm so proud to call you one of my best friends. Davina, Arjun, and Quincy – lab mates in college turned family – each of you is special to me. We started this grad school journey together, and I'm thankful we've remained friends throughout it all. Although we've each found different paths throughout grad school, we've all found our way and I'm proud of how far we've come. Professor Carol Parish – my undergrad research mentor – I absolutely would not have found this path without you. Thank you for mentoring me so well, and helping me find myself and realize my career goals. You opened my eyes to a career I only could've dreamed of, and you guided me to get there. I'll forever be grateful to you for taking a chance on a freshman you barely knew by letting me join your lab and supporting me every step since then.

To my graduate school friends: Thank you for your constant support throughout these five years. Having people so close that were going through the same journey was invaluable. I'll never forget our Shadowood gatherings, Back Bar Thursdays, and the many tough UNC games we watched together. Sarah, Emilie, Corban, Emglack, and Doug – you are all remarkable scientists and people, and I couldn't ask for a better group of people to go through graduate school with.

To my family: I could not have done this without you. It's hard to express how grateful I am for each of you. Although you didn't understand my science, you would always listen to me and remind me that I was capable when I got too deep into my research to realize it myself. I especially want to thank: Dani and Erin – my siblings – you are absolutely the best siblings a girl could ask for. You love me so well and I couldn't imagine being here without you. Grandma and Debbie – thank you for always attempting to read my papers and for being so supportive of this journey. Carol, Tanner, Evan, and Linder – thank you for all the holidays spent together and for making me feel so welcome in Durham. And finally, Mom and Dad – I think you make a run for the best parents ever. You were always there to talk and you have been supportive of every one of my dreams. I couldn't ask for anything more, and I love you so much.

To CJ: I know you've only been in my life for a small part of this journey, but I am endlessly grateful for you. You are an amazing partner and have been supportive of all my dreams, even when they bring me far from you. Thank you for loving me so well and for bearing with all of my quirks. You have made this last piece of my Ph.D. so much fun and I can't wait to see where we go from here.

TABLE OF CONTENTS

LIST OF FIGURES xi

LIST OF TABLES xiii

LIST OF ABBREVIATIONS AND SYMBOLS xiv

CHAPTER 1: INTRODUCTION 1

1.1 Motivation 1

1.2 Fluoride-ion batteries 2

1.3 Background of electrides 4

1.4 Hydrogen storage 5

1.5 Understanding the use of computation with experiment 6

1.5.1 The importance of a feedback loop 7

1.5.2 Probing electride character 8

1.5.3 Exploring highly disordered systems 10

1.6 Overview of the research described in this thesis 11

REFERENCES 12

CHAPTER 2: METHODS 19

2.1 Introduction 19

2.2 Computational methods 19

2.2.1 Density Functional Theory 19

2.2.1.1 Electronic structure 20

2.2.1.2 Dynamic stability 21

2.2.1.3 Electrical conductivity 22

2.2.1.4 Work function 23

2.2.1.5 Mechanical properties 24

2.2.1.6 Diffusion analysis 25

2.2.1.7 DFT methods for Chapter 3 26
2.2.2 Evolutionary algorithm 28
2.2.2.1 USPEX 28
2.2.3 Cluster expansion 28
2.2.3.1 CLEASE 31
2.2.3.2 CLEASE with Simmate 33
2.3 Synthesis methods 34
2.3.1 Sc_2C 34
2.3.2 Hydrogenation of Sc_2C 35
2.4 Characterization methods 35
2.4.1 Powder x-ray diffraction with Rietveld refinement 35
2.4.1.1 Sc_2C and Sc_2CH_2 39
2.4.2 X-ray photoelectron spectroscopy 39
2.4.2.1 Sc_2C 40
REFERENCES 43
CHAPTER 3: 2D ELECTRIDES AS FLUORIDE INTERCALATION ELECTRODES0F0F 50
3.1 Introduction 50
3.2 Results and Discussion 52
3.3 Conclusions 60
REFERENCES 62
CHAPTER 4: Sc_2C – A 2D SEMICONDUCTING ELECTRIDE1F1F 64
4.1 Introduction 64
4.2 Results and Discussion 67
4.2.1 Phase diagram exploration 67
4.2.2 Assessment of electride character and electronic structure 70
4.2.3 Emergence of semiconducting behavior in electrides 72
4.2.4 Exfoliation potential 73
4.2.5 Stability in air 74

4.3 Conclusions 76
REFERENCES 78
CHAPTER 5: HYDROGENATION OF Sc_2C 82
5.1 Introduction 82
5.2 Computational properties exploration 83
5.3 Synthesis 84
5.4 Exfoliation potential 87
5.5 Outlook 87
REFERENCES 89
APPENDIX: SUPPORTING INFORMATION FOR CHAPTER 3 2F2F 91
A3.1 Phases in the $[Y_2C]^{2+}(e^-)_2$-Y_2CF_2 system 91
A3.2 Characteristics of the $[Y_2C]^{2+}(e^-)_2$-Y_2CF_2 as an anode in a fluoride-ion battery 93
A3.3 Cluster expansion models 96
REFERENCES 97
APPENDIX: SUPPORTING INFORMATION FOR CHAPTER 4 3F3F 98
A4.1 Historical diffraction data 98
A4.2 Supplementary results and discussion 99
REFERENCES 108
APPENDIX: SUPPORTING INFORMATION FOR CHAPTER 5 109
A5.1 Band structure of Sc_2CF_2 109
REFERENCES 110

LIST OF FIGURES

Figure 2-1. Electron density isosurfaces at the Fermi level (± 0.1 eV vs. E_f) for a single F atom in a 5×5×1 supercell of Y_2C 27

Figure 3-1. Concept of electron−anion exchange. 52

Figure 3-2. Mechanism of electron−anion exchange 53

Figure 3-3. Polarization of valence electrons at and near the Fermi level. 55

Figure 3-4. Application of electron−anion exchange 57

Figure 3-5. Convex hull and voltage profile from cluster expansion 58

Figure 4-1. An adapted periodic table highlighting the valency of various cations 65

Figure 4-2. Phase diagram of the Sc-C system. 67

Figure 4-3. X-ray diffraction patterns of the experimental structure compared to the calculated layered and cubic Sc_2C phases. 69

Figure 4-4. TEM images of Sc_2C 70

Figure 4-5. Electronic structure of Sc_2C compared to Al_2C and Y_2C 71

Figure 4-6. PXRD of Sc_2C oxidation 75

Figure 4-7. X-ray photoelectron spectroscopy spectra of scandium and carbon as-made, after 1 day in air, and after 11 days in air 76

Figure 5-1. NEB calculation of Sc_2CH_x 83

Figure 5-2. Band structure and DOS of Sc_2CH_2 84

Figure 5-3. PXRD pattern of Sc_2C hydrogenation 85

Figure 5-4. Representative HRTEM images of attempted exfoliation of Sc_2CH_2 87

Figure A3-1. The two stacking sequences of Y_2C and Y_2CF_2 92

Figure A3-2. Crystal structures of the T1, O3, and H1-3 phases considered in our cluster expansion. 93

Figure A3-3. The cluster expansion models for the T1, O3, and H1-3 phases 96

Figure A4-1. An illustration of electride-atom hybridization. 100

Figure A4-2. XRD pattern of typical arc-melting synthesis without annealing 100

Figure A4-3. XRD pattern of $Sc_2C_{0.95}$ 101

Figure A4-4. XRD pattern of $Sc_2C_{1.13}$ 101

Figure A4-5. The band structure of Y_2C. 102

Figure A4-6. The band structure of Al_2C. 102

Figure A4-7. The band structure of Sc_2C compared to that of Sc-substituted Al_2C. 103
Figure A4-8. The calculated work function of Sc_2C for (0001). 104
Figure A4-9. The calculated work function of Sc2C for (11-20). 104
Figure A4-10. TEM images of sonication experiments. 106
Figure A4-11. High-resolution XPS spectra of oxygen after 0, 1, and 11 days of sitting in air. 107
Figure A5-1. Band structure calculation of Sc_2CF_2 109

LIST OF TABLES

Table 2-1. Charges on the constituent atoms in the Y_2C systemfor $[Y_2C]^{2+}(e^-)_2$ taken from literature, Y_2CF_2 calculated using Bader charge analysis, Y_2CF_2 calculated using WS-LDOS charge analysis, and F^--deficient Y_2CF_2 in its ground-state (GS) and its transition state (TS, with F^- halfway between tetrahedral sites) calculated using PDOS charge analysis. 27

Table 2-2. Scandium XPS peak positions 41

Table 2-3. Scandium XPS peak splitting 41

Table 2-4. Scandium XPS FWHM $2p^{3/2}$:$2p^{1/2}$ 41

Table 3-1. Atomic Distances in $[Y_2C]^{2+}(e^-)_2$[18] and Y_2CF_2[11] 56

Table 5-1. EDS comparing oxygen:scandium of Sc_2C to Sc_2CH_x sample. 86

Table A4-1. Comparison of diffraction patterns for ScC_x. 98

Table A4-2. Interlayer and Intralayer stiffness tensors for Sc_2C and Y_2C. 105

Table A4-3. Various moduli of Sc_2C and Y_2C. 105

LIST OF ABBREVIATIONS AND SYMBOLS

2D	two-dimensional
2DEG	two-dimensional electron gas
ACET	anion-coupled electron transfer
AIMD	*ab-initio* molecular dynamics
AMSET	*ab-initio* scattering and transport software
ASE	atomic simulation environment
CLEASE	cluster expansion in atomic simulation environment
CV	cross-validation
CVD	chemical vapor deposition
DFT	density functional theory
DFPT	density functional perturbation theory
DOS	density of states
EAX	electride-anion exchange
ECI	effective cluster interaction
EDS	energy dispersive x-ray spectroscopy
ELF	electron localization function
FDM	finite displacement method
FFT	fast Fourier transform
FIB	fluoride-ion battery
FWHM	full width at half maximum
GGA	generalized gradient approximation
GS	ground state
HRTEM	high-resolution transmission electron microscopy
LIB	lithium-ion battery
LOO	leave-one-out
LST	linear synchronous transite
NEB	nudged elastic band

PAW	Projector-augmented wave
PBE	Perdew–Burke-Ernzerhof
PCET	proton-coupled electron transfer
PDOS	projected density of states
PXRD	powder x-ray diffraction
PyMatGen	Python Package for Material Genomics
QST	quadratic synchronous transit
SAED	selected area electron diffraction
Simmate	The Simulated Materials Ecosystem
TS	transition state
USPEX	universal structure predictor: evolutionary xtallography
VASP	Vienna *ab initio* software package
XC	exchange-correlation
XPS	x-ray photoelectron spectroscopy

CHAPTER 1: INTRODUCTION

1.1 Motivation

Within the past half-century, society has begun to study and understand the effects of human-driven climate change. Initially, most research was focused on the intersection of humanity with climate change and identifying how our society contributes to this phenomenon. Activities such as burning coal, oil, and natural gas in heating, electrical power generation, and cement production were identified as contributing to an increase in greenhouse warming[1]. Additionally, deforestation and land clearing negatively impact the amount of carbon dioxide that the earth can convert to other byproducts, thus contributing to the increased amount of atmospheric carbon dioxide. Many studies have identified a causal relationship between human emissions and temperature[2–5].

Recently, the focus has shifted to searching for solutions to mitigate our impact. An important area for innovation is alternative energy generation. Burning coal and oil has dominated energy production for most of our industrialized history, but both methods produce carbon dioxide as a byproduct, contributing to global greenhouse emissions. Natural gas has been used to mitigate some of these effects, as natural gas emits ~50% less CO_2 than coal, according to the U.S. Energy Information Administration[6]. While this figure is significantly better in natural gas than other sources of energy, burning natural gas also produces other byproducts such as carbon monoxide and methane, another greenhouse gas. Additionally, the process of obtaining natural gas, fracking, is harmful to the environment and human health[7]. Thus, this motivates the search for energy sources that produce little to no greenhouse gas emissions and the least possible harm to surrounding ecosystems.

The most promising alternative sources currently being explored derive energy from wind and solar, among others[8]. These sources are inherently intermittent, creating problems with grid stability. Integrated power facilities for energy production at all times of day have been proposed recently[9]. An alternative is an energy storage system that is large enough to store energy for use at all times of day, and commercial

lithium-ion batteries (LIBs) are currently the best candidates. While LIBs have many promising qualities, such as a long-life cycle and high energy density, they have several drawbacks that necessitate the search for alternatives. These include high costs, safety concerns, lithium shortages, and a lack of end-of-life recycling infrastructure[10]. There has been much research in improving current lithium-ion batteries to address these concerns since they were proposed just over 40 years ago[11], but my thesis has taken a different approach. Herein, I explore two alternative energy storage systems: fluoride-ion batteries (FIBs), which have little history but could offer exciting new applications and insights to the field of rechargeable batteries, and hydrogen storage systems, a field that has grown in recent years but still faces several challenges for large-scale commercialization.

1.2 Fluoride-ion batteries

Fluoride shuttle batteries (FIB) were first proposed just over a decade ago because fluorine has high electronegativity and low weight[12]. Fluorine has high chemical reactivity and is gaseous, making it unsuitable as a shuttle, but the fluoride anion could be used to shuttle between two electrodes because it is electrochemically stable. Compared to commercial LIBs, theoretical FIBs offer higher energy density, which is particularly of interest for large-scale energy storage[13]. Additionally, because fluorine is so electronegative, the fluoride ion is very redox-stable, enabling a wide electrochemical potential window and the potential to provide a higher open circuit voltage compared to many alternatives to LIBs. Typically, fluoride-containing materials are more abundant compared to lithium reserves[13]. Given all of these possible advantages of FIBs compared to other technologies, their realization is warranted.

Currently, there are no standard anode, cathode, or electrolyte materials for fluoride-ion batteries. Solid-state electrolytes have dominated the field thus far[14–18], but recently, the first room-temperature liquid electrolyte that can shuttle fluoride ions reversibly was discovered[19]. Solid-state batteries tend to be safer than liquid electrolyte batteries, and fluoride shows high mobility in many solid-state materials. During my time at UNC-Chapel Hill, we published a high-throughput study on the diffusion of fluoride in various materials, where we proposed that solid electrolyte materials should have high ionic conductivity, a high band gap (low electrical conductivity), and low cost. Additionally, electrolytes should have a high electrochemical stability window and must be compatible with the electrode materials. From this, we

discovered several promising candidates for solid-state electrolytes[20]. My research, however, has focused on the discovery of novel electrode materials.

There are two possible reaction mechanisms for the storage of ions in electrodes: conversion or intercalation. Conversion electrodes typically offer higher capacities[13,21] and during my thesis, we discovered 168 new conversion-based cathode materials using a high-throughput study considering the thermodynamics of the fluorination/defluorination process[22]. However, in a conversion reaction, the material undergoes a reaction during cycling, thus changing the structure and volume. This tends to decrease the lifetime of the FIB to only a few cycles. Conversion-based electrodes have been widely studied in the last decade[23], whereas fewer intercalation-based electrodes have been found.

Early examples of intercalation-based electrodes for FIBs were found using $YBa_2Cu_3O_{7-x}$[(24)] and La_2CuO_4[(25)], but no reversibility was observed. Currently, three different structure types have been studied as intercalation-based material types: Schafarzikite, perovskite, and Ruddlesden-Popper. Scharfarzikite-type compounds were studied for reversible electrochemical fluorination[26], where this structure has one-dimensional channels of fluoride rather than the typical ion layer seen in most intercalation-type electrodes, but saw poor cycling with solid electrolytes. Clemens *et al.* attempted to develop a solid-state cell with an intercalation mechanism using a perovskite-related $BaFeO_{2.5}$, but this showed poor performance[27]. In 2017, the first reversible electrochemical intercalation was observed in the Ruddlesden-Popper structure type using $LaSrMnO_4$[28]. Successful reversible insertion of fluoride ions in this structure type was proof of principle for developing intercalation-based cathodes, and since then, many Ruddlesden-Popper-type materials have been studied as cathodes for FIBs[13].

Overall, very little work has been done in the space of intercalation-based FIB anodes. The only known intercalation anodes are Ruddlesden-Popper-type oxides[29–31]. Topochemical modification of Ruddlesden-Popper oxyfluorides has been investigated, but significant redox activity has been found only for a Ni-based compound[32]. Therefore, much of my work has focused on exploring intercalation in a different class of materials, electrides.

1.3 Background of electrides

Electrides are ionic solids where electrons are completely separated from surrounding atoms, sitting in distinct lattice sites and acting as anions. These 'electride' electrons are not bound to a nucleus, typically resulting in high conductivities and low work functions. Because of their impressive properties, these materials have potential applications in catalysis[33–35], electron emitters[36], optics[37,38], superconductors[39] and battery electrodes[40]. I will give a brief history of electride materials below, but for a more in-depth history of electrides, refer to reviews by Druffel *et al.*[41], Liu *et al.*[42], Zhang *et al.*[43], and Hosono *et al.*[44].

The earliest reported system with unbound electrons was found in a solvated system where potassium is dissolved in liquid ammonia[45], producing solvated electrons. These solutions exhibited several physical changes, such as a change in color, but it was not until many decades later that researchers were able to characterize these electrons[46–50].

These same ideas were explored in solids, where researchers found point defects causing transparent crystals to absorb visible light, called color centers[51,52]. Perhaps the most notable is the F-center, where an electron fills an anion vacancy[53]. Electrides are fundamentally different from f-centers because, while f-centers are disordered and tend to have a low concentration, the electride electrons are periodic, allowing them to interact with each other[44,54]. In the early 1980s, Dye demonstrated that Cs^+ contained anionic electrons in a high concentration and coined the term "electride"[47–50]. Following these studies, many other electrides were reported with other organic ligands and alkali metals[55–58].

Up to this point, all electrides decomposed at room temperature. It was not until 2003 that the first thermally-stable electride was synthesized using the nanoporous crystal of mayenite, which is made up of $[Ca_{24}Al_{28}O_{64}]^{4+}$ with 2 oxygen anions compensating for the framework's overall positive charge. Matsuishi *et. al.* extracted the free anions by chemical reduction and injected free electrons, making $[Ca_{24}Al_{28}O_{64}]^{4+}4e^-$ [(59)]. Because the electride must be "activated" via chemical reduction, it is considered an activated electride. The mayenite structure can be used to make a number of different activated electrides with substitutions[60,61].

In addition to using physical or chemical treatments to activate electride character, pressure can be used to activate electride character. Initially, this was exploited in alkali metals[62–65], but computationally, many more complex systems have been predicted to form electrides at high pressure[66–70]. We can think of high-pressure and activated electrides as materials with nonground-state configurations that are permanently populated[42]. Because these states are accessed by some treatment, they exhibit tunable electronic properties as the treatment changes[63,65].

The mayenite-based electrides are also considered 0D, which is characterized based on the degree of freedom of the electride density; 0D electrides have electrons localized to a single point, 1D electrides have electride electron delocalization along a channel, and 2D electrides contain electron density delocalized in a plane. In some 0D electrides, diffusion of electride electrons can still occur via a hopping mechanism[71]. 0D, 1D, and 2D can be used to classify the electron density in any electride.

Because of our group's interest in layered materials, we focused on 2D electrides. The first 2D electrides were synthesized in the 1950s and 1960s (Ca_2N[72], Ba_2N[73], and Sr_2N[73]), but were not identified as electrides until 2000[74,75]. Since then, the structures and properties of six experimentally demonstrated 2D electrides have been studied in great depth[76–85], and we have begun to develop a rudimentary understanding of how the 2D electride structure and composition drive properties[44,86]; however, because so few are known, robust design rules for 2D electrides based on the relationship between composition and properties have yet to be developed. In particular, we noticed that all known 2D electrides are metallic, but we hypothesized that compositional changes based on systematic changes in electronegativity could lead to new electronic properties. Given this gap in knowledge, I have focused on understanding the synthesis and properties of Sc_2C, a 2D electride with the most electronegative metal yet incorporated adjacent to the electride site. Additionally, because Sc_2C is predicted to be a good hydrogen storage material[87,88], I explored its ability to store hydride between its layers.

1.4 Hydrogen storage

Hydrogen energy is being explored as an alternative to fossil fuels because it has negligible emissions and high energy density[89,90]. Hydrogen is a great synthetic fuel because it is lightweight and abundant, and when burnt with oxygen, hydrogen produces water vapor. Hydrogen energy can be changed

into electrical energy using fuel cells[91,92]; however, hydrogen storage remains a key problem for the commercialization of hydrogen-powered vehicles. High-pressure gas storage is one possible storage method, but it comes with safety risks[93]. Another method is low-temperature liquid storage, but because the hydrogen must be kept below -250°C, this method is costly[94–98].

Solid hydrogen storage uses solid materials to absorb hydrogen and can be kept under ambient temperature and pressure, so it would be more suitable than other commercial hydrogen storage methods for mobile applications. Typically, hydrogen is released from these materials through pyrolysis. Rare earth metals are stable at room temperature but tend to have a high cost and low storage density [99]. Titanium and iron hydrogen storage materials are lower cost but still have a low density[100]. Magnesium is low cost and has a high storage density, but hydrogen pyrolysis occurs only at high temperatures[101]. Other systems being explored include metal borohydrides, metal alanates, metal amides, and amine metal borohydrides, but still, none of the materials discussed meet the DOE standards for mobile applications[102]. Herein, I demonstrate how Sc_2C might be used to fill this gap.

1.5 Understanding the use of computation with experiment

One of the most important lessons throughout my thesis work was learning how computational and experimental results together can inform our understanding of chemistry. In this section, I will discuss the interplay between computation and experiments in inorganic materials systems, and offer my thoughts on how using both can give insight into areas that we could not understand using only one.

Computational experiments can offer insight into the structure and properties of solid-state materials, small molecules, and larger systems such as proteins. In this section, I will focus on the use of density functional theory (DFT) to model crystalline materials, as this was the primary method I used in my thesis work. Currently, DFT can be used to calculate a system's total energy, potential energy, electronic structure, mechanical properties, and phonon spectra, among other properties. I will discuss the implementation of DFT to calculate various properties in section 2.2.1. While DFT can reliably solve for a variety of properties, it also has limitations, which can be supplemented in some cases through experiment.

1.5.1 The importance of a feedback loop

One challenge of DFT is it lacks a set of universal parameters. Based on computational studies in other systems (which are benchmarked according to experiment), we can make an informed guess for what our input parameters should be; however, there is always a tradeoff between calculating the most accurate possible energy (using the best input parameters) versus using a reasonable amount of computational time. One can obtain less accurate energy using less time, but without benchmarking the computational parameters to experiment, it wouldn't be clear how inaccurate the output is.

Additionally, there is another problem in using DFT without experiment: different functionals are optimized to solve for different properties. Practical realizations of DFT rely on an approximation of the unknown exchange-correlation (XC) functional of the charge density[103], and functionals will approach this approximation in different ways. As I discussed previously, there is always a tradeoff between calculation time and accuracy; functionals that tend to be more accurate require more computing power. Therefore, users must understand the tradeoffs of each functional to determine which will be best for their system. Additionally, it can be a good idea to benchmark values obtained using a particular functional on a given system against experimental values to ensure it is accurate enough in its approximation of the system's energy/properties.

With these limitations in DFT, experiments are necessary to assess calculation accuracy. A property that is easy to measure experimentally can be used to benchmark whether a set of input parameters outputs sufficient accuracy. This benchmark gives assurance that the calculation will give sufficient accuracy for other properties that are harder and/or impossible to experimentally probe. One example of this idea's importance is in band structure calculations. Many researchers have sought ways to characterize the band gap using conductivity measurements and/or optical spectroscopy because these are widely accessible methods. Optical spectroscopy can only measure the direct band gap of a material, while conductivity measurements will give the lowest energy band gap, whether direct or indirect. The challenge with both methods in my systems has been the presence of a second metallic phase. This second phase is present in a sufficient amount of sample to create a network of conduction throughout the sample; therefore, both techniques fail to measure a band gap experimentally. Therefore, the band structure of

phase-impure materials must be calculated reliably with DFT. It is widely known that GGA functionals severely underestimate band gaps[104,105], so it is crucial that the desired functional is benchmarked to experiment. In this case, HSE-06 has been sufficiently optimized for small-band gap semiconductors[105]; therefore, I can calculate the band gap of one phase accurately without needing to measure it experimentally.

This example highlights the importance of a feedback loop between computation and experiment. There are properties that we cannot probe experimentally that must be calculated computationally, like band gap for phase impure materials; in tandem, we cannot verify a calculated synthetic approach or material properties without experiment. A good experimental design will include properties that can be studied both computationally and experimentally to corroborate the methods used. Then, any properties that can be explored only using calculations or experiments can be studied reliably. The next two sections will discuss how computation and experiment can complement one another to understand properties that we could not study using only one.

1.5.2 Probing electride character

A challenging area for DFT is in the modeling of systems with non-traditional ions, such as electrides. Visualizing the localized electron in DFT can be a challenge, and GGA functionals tend to overestimate the delocalization of the confined electron[106]. Given this overestimation, incorporating a fraction of the Hartree-Fock exchange can increase the localization of the electron. Therefore, calculating the electron localization in electrides requires the use of a hybrid functional. To confirm the electride character, where the crystal structure contains localized electrons in distinct lattice sites, one can run an electron localization function (ELF) calculation using HSE-06. This method calculates the likelihood of finding an electron near a reference electron at a given point in space with the same spin. In the ELF of an electride material, we expect to find an area of high electron localization that is not associated with an atom. This calculation gives information about the system that no current experimental method can; however, to confirm electride character, the properties of the experimental structure must align with expected properties for electrides.

One additional area in which conventional computational methods fail is in accurately quantifying the oxidation state of each atom in a system with non-traditional ions. Bader charge analysis has conventionally been used to parse electron density within a system[107], but it fails for species that are not associated with a traditional ion. We have used a dummy atom in place of the electride site for calculating the oxidation state of ions and electride electrons in electride systems to quantify the oxidation state in the Y_2C-Y_2CF_2 system[108], but this method still requires an arbitrary placement of the dummy atom. Given these challenges, we must use experiments to corroborate our calculations of the oxidation state and electride character.

A characterization technique that I've used to develop an understanding of atomic oxidation states is X-ray photoelectron spectroscopy (XPS). I discuss this technique in more detail in section 2.4.2. XPS gives core-level electronic binding energy, which can be used to understand the chemical environment of any atom in the system. Specifically, by comparing the binding energy for an atom in an unknown system to the binding energy for the same atom in well-studied systems, one can elucidate the atom's approximate oxidation state. For systems like the carbide electrides, this can provide indirect evidence of electride character because atoms in these structures tend to have non-traditional oxidation states (yttrium is +2 and carbon is -2, giving the overall lattice a +2 charge without accounting for electride density). In addition, pairing XPS with a composition characterization method, such as elemental analysis and/or Rietveld refinement in PXRD, which gives additional information about the stoichiometry of the product, can provide good evidence that there is excess electron density present in the sample. This method is relatively straightforward but is an indirect measurement of electride character; therefore, confirming electride character most directly and efficiently requires building an understanding through computation and experiment.

Pairing calculations of the ELF and Bader charge analysis with a measure of stoichiometry and oxidation state can provide great evidence of electride character in an experimental sample using widely available methods. The experiment indicates that there is excess electron density in a material with a stoichiometry that matches the calculation and confirms the structure input into the calculation, and the calculation offers insight into the location of electron localization in the experimental structure and quantifies

the oxidation state of the structure's atoms. This interplay allows us to confirm structures as electrides (chapter 4) and study their properties as storage materials (chapters 3 and 5) using widely available methods.

1.5.3 Exploring highly disordered systems

An important consideration when designing DFT experiments is that computational time scales with the number of atoms[109]; therefore, running DFT on large systems is expensive and inefficient. Consequently, calculating large, highly disordered structures requires an alternative method; to accomplish this, I've used a method called cluster expansion, which I describe in section 2.2.3. In summary, this method decreases computational cost by mapping DFT to a simple equation that is much quicker to evaluate, allowing the study of large structures. However, even methods such as cluster expansion require some experimental insight to output meaningful data; building a cluster expansion model requires the input of a structural framework, which cannot be done without additional insight from calculations and syntheses to understand the system's thermodynamics. Therefore, the most efficient method of understanding highly disordered crystalline systems requires a combination of computation and experiment.

To characterize the bulk structure of inorganic structures, I have primarily used powder x-ray diffraction (PXRD). The use of PXRD in an experiment is described in more detail in section 2.4.1; in summary, it provides crystallographic data for a powdered sample that can be used to identify phases and determine unit cell dimensions. The structures that I study are crystalline overall but have a small amount of disorder in the interlayer, so I can investigate the bulk structural framework using PXRD and obtain the overall stoichiometry using elemental analysis/Rietveld refinement[110]. However, PXRD cannot give information about the local disorder (i.e. disorder between the layers) in my materials of interest. Therefore, describing local disorder in a largely crystalline material requires a combination of computation to probe the local structure and experiment to develop the overall structural model. This interplay allows us to develop a structural model of disorder that can be useful for electrochemical experiments (chapter 3) and for understanding sample properties (chapters 4 and 5).

1.6 Overview of the research described in this thesis

Given the gaps in knowledge described in sections 1.2, 1.3, and 1.4, my thesis seeks to use 2D electrides, which are layered, as intercalation anodes in FIBs and hydrogen storage cells.

I first demonstrate a novel electrochemical mechanism that shows 2D electrides, when applied as FIB anodes, do not undergo redox during cycling. This is a fundamentally new mechanism of intercalation, and it gives little volume change with cycling. I show that the Y_2C could be a good intercalation-based anode for FIBs because it has fast fluoride diffusion, little volume change, a large energetic driving force for F^- insertion, and a similar capacity to commercial LIB electrodes. I also explore the energetics of F^- insertion to create a voltage profile, which will be useful to our experiments.

Additionally, I explore how compositional changes in 2D electrides change their electronic properties. Specifically, I substitute Sc into the Y site in Y_2C and find that this material is thermodynamically stable. I corroborate my calculations with experiments exploring the synthesis of the new phase. I then use a combination of computation and experiment to explore the properties of Sc_2C, which results in a new design rule for 2D electride materials using simple chemistry concepts.

Lastly, I show that Sc_2C can store hydrogen between its layers, and share evidence that shows fast hydride diffusion in Sc_2C through computation and experiment. The knowledge generated by this thesis will guide future synthetic efforts for finding new 2D electrides, which might be used in various applications, including as commercially viable intercalation anodes.

REFERENCES

(1) Redlin, M.; Gries, T. Anthropogenic Climate Change: The Impact of the Global Carbon Budget. *Theor Appl Climatol* **2021**, *146* (1–2), 713–721.

(2) Kodra, E.; Chatterjee, S.; Ganguly, A. R. Exploring Granger Causality between Global Average Observed Time Series of Carbon Dioxide and Temperature. *Theor Appl Climatol* **2011**, *104* (3–4), 325–335.

(3) Attanasio, A. Testing for Linear Granger Causality from Natural/Anthropogenic Forcings to Global Temperature Anomalies. *Theor Appl Climatol* **2012**, *110*, 281–289.

(4) Attanasio, A.; Pasini, A.; Triacca, U. Granger Causality Analyses for Climatic Attribution. *Atmospheric and Climate Sciences* **2013**, *03* (04), 515–522.

(5) Triacca, U.; Attanasio, A.; Pasini, A. Anthropogenic Global Warming Hypothesis: Testing Its Robustness by Granger Causality Analysis. *Environmetrics* **2013**, *24* (4), 260–268.

(6) How much carbon dioxide is produced when different fuels are burned? *U.S. Energy Information Administration*.

(7) Wollin, K. M.; Damm, G.; Foth, H.; Freyberger, A.; Gebel, T.; Mangerich, A.; Gundert-Remy, U.; Partosch, F.; Röhl, C.; Schupp, T.; Hengstler, J. G. Critical Evaluation of Human Health Risks Due to Hydraulic Fracturing in Natural Gas and Petroleum Production. *Arch Toxicol* **2020**, *94* (4), 967.

(8) New Energy Outlook 2022 | BloombergNEF | Bloomberg Finance LP.

(9) Sánchez, A.; Zhang, Q.; Martín, M.; Vega, P. Towards a New Renewable Power System Using Energy Storage: An Economic and Social Analysis. *Energy Convers Manag* **2022**, *252*, 115056.

(10) Fan, X.; Liu, B.; Liu, J.; Ding, J.; Han, X.; Deng, Y.; Lv, X.; Xie, Y.; Chen, B.; Hu, W.; Zhong, C. Battery Technologies for Grid-Level Large-Scale Electrical Energy Storage. *Trans Tianjin Univ* **2019**, *26* (2), 92–103.

(11) Mizushima, K.; Jones, P. C.; Wiseman, P. J.; Goodenough, J. B. LixCoO2 (0<x≤1): A New Cathode Material for Batteries of High Energy Density. *Solid State Ion* **1981**, *3–4* (C), 171–174.

(12) Anji Reddy, M.; Fichtner, M. Batteries Based on Fluoride Shuttle. *J Mater Chem* **2011**, *21* (43), 17059–17062.

(13) Nowroozi, M. A.; Mohammad, I.; Molaiyan, P.; Wissel, K.; Munnangi, A. R.; Clemens, O. Fluoride Ion Batteries - Past, Present, and Future. *J Mater Chem A* **2021**, 5980–6012.

(14) Mohammad, I.; Witter, R.; Fichtner, M.; Reddy, M. A. Introducing Interlayer Electrolytes: Toward Room-Temperature High-Potential Solid-State Rechargeable Fluoride Ion Batteries. *ACS Appl Energy Mater* **2019**, *2* (2), 1553–1562.

(15) Mohammad, I.; Witter, R.; Fichtner, M.; Anji Reddy, M. Room-Temperature, Rechargeable Solid-State Fluoride-Ion Batteries. *ACS Appl Energy Mater* **2018**, *1* (9), 4766–4775.

(16) Mohammad, I.; Chable, J.; Witter, R.; Fichtner, M.; Reddy, M. A. Synthesis of Fast Fluoride-Ion-Conductive Fluorite-Type $Ba_{1-X}Sb_xF_{2+x}$ ($0.1 \leq x \leq 0.4$): A Potential Solid Electrolyte for Fluoride-Ion Batteries. *ACS Appl Mater Interfaces* **2018**, *10* (20), 17249–17256.

(17) Molaiyan, P.; Witter, R. Surface Defect-Enhanced Conductivity of Calcium Fluoride for Electrochemical Applications. *Mater Des Proc Comm* **2019**, *1* (4), e44.

(18) Murray, E.; Brougham, D. F.; Stankovic, J.; Abrahams, I. Conductivity and Fluoride Ion Dynamics in α-$PbSnF_4$; 19F Field-Cycling NMR and Diffraction Studies. *J Phys Chem C* **2008**, *112* (14), 5672–5678.

(19) Davis, V. K.; Bates, C. M.; Omichi, K.; Savoie, B. M.; Momčilović, N.; Xu, Q.; Wolf, W. J.; Webb, M. A.; Billings, K. J.; Hawn Chou, N.; Alayoglu, S.; McKenney, R. K.; Darolles, I. M.; Nair, N. G.; Hightower, A.; Rosenberg, D.; Ahmed, M.; Brooks, C. J.; Miller III, T. F.; Grubbs, R. H.; Jones, S. C. Room-Temperature Cycling of Metal Fluoride Electrodes: Liquid Electrolytes for High-Energy Fluoride Ion Cells. *Science* **2018**, *362* (6419), 1144–1148.

(20) Sundberg, J. D.; Druffel, D. L.; McRae, L. M.; Lanetti, M. G.; Pawlik, J. T.; Warren, S. C. High-Throughput Discovery of Fluoride-Ion Conductors via a Decoupled, Dynamic, and Iterative (DDI) Framework. *NPJ Comput Mater* **2022**, *8* (1).

(21) Xiao, A. W.; Galatolo, G.; Pasta, M. The Case for Fluoride-Ion Batteries. *Joule* **2021**, *5* (11), 2823–2844.

(22) McTaggart, D. H.; Sundberg, J. D.; McRae, L. M.; Warren, S. C. Assessing Ternary Materials for Fluoride-Ion Batteries. *Sci Data* **2023**, *10* (1), 1–8.

(23) Gschwind, F.; Rodriguez-Garcia, G.; Sandbeck, D. J. S.; Gross, A.; Weil, M.; Fichtner, M.; Hörmann, N. Fluoride Ion Batteries: Theoretical Performance, Safety, Toxicity, and a Combinatorial Screening of New Electrodes. *J Fluor Chem* **2016**, *182*, 76–90.

(24) MacManus, J. L.; Fray, D. J.; Evetts, J. E. Fluorination of $Y_1Ba_2Cu_3O_{7-x}$ by a Solid State Electrochemical Method. *Physica C: Superconductivity and its Applications* **1991**, *184* (1–3), 172–184.

(25) Delville, M. H.; Barbut, D.; Wattiaux, A.; Bassat, J. M.; Ménétrier, M.; Labrugère, C.; Grenier, J. C.; Etourneau, J. Electrochemical Fluorination of La_2CuO_4: A Mild “Chimie Douce” Route to Superconducting Oxyfluoride Materials. *Inorg Chem* **2009**, *48* (16), 7962–7969.

(26) Nowroozi, M. A.; de Laune, B.; Clemens, O. Reversible Electrochemical Intercalation and Deintercalation of Fluoride Ions into Host Lattices with Schafarzikite-Type Structure. *ChemistryOpen* **2018**, *7* (8), 617–623.

(27) Clemens, O.; Rongeat, C.; Reddy, M. A.; Giehr, A.; Fichtner, M.; Hahn, H. Electrochemical Fluorination of Perovskite Type $BaFeO_{2.5}$. *Dalton Transactions* **2014**, *43* (42), 15771–15778.

(28) Nowroozi, M. A.; Wissel, K.; Rohrer, J.; Munnangi, A. R.; Clemens, O. LaSrMnO4: Reversible Electrochemical Intercalation of Fluoride Ions in the Context of Fluoride Ion Batteries. *Chem Mater* **2017**, *29* (8), 3441–3453.

(29) Wissel, K.; Vogel, T.; Dasgupta, S.; Fortes, A. D.; Slater, P. R.; Clemens, O. Topochemical Fluorination of n = 2 Ruddlesden-Popper Type $Sr_3Ti_2O_7$ to $Sr_3Ti_2O_5F_4$ and Its Reductive Defluorination. *Inorg Chem* **2020**, *59* (2), 1153–1163.

(30) Wissel, K.; Malik, A. M.; Vasala, S.; Plana-Ruiz, S.; Kolb, U.; Slater, P. R.; da Silva, I.; Alff, L.; Rohrer, J.; Clemens, O. Topochemical Reduction of La2NiO3F2: The First Ni-Based Ruddlesden-Popper n = 1 T′-Type Structure and the Impact of Reduction on Magnetic Ordering. *Chem Mater* **2020**, *32* (7), 3160–3179.

(31) Wissel, K.; Dasgupta, S.; Benes, A.; Schoch, R.; Bauer, M.; Witte, R.; Fortes, A. D.; Erdem, E.; Rohrer, J.; Clemens, O. Developing Intercalation Based Anode Materials for Fluoride-Ion Batteries:

Topochemical Reduction of Sr2TiO3F2 via a Hydride Based Defluorination Process. *J Mater Chem A* **2018**, *6* (44), 22013–22026.

(32) Nowroozi, M. A.; Clemens, O. Insights on the Behavior of Conversion-Based Anode Materials for Fluoride Ion Batteries by Testing against an Intercalation-Based Reference Cathode. *ACS Appl Energy Mater* **2018**, *1* (11), 6626–6637.

(33) Ye, T. N.; Li, J.; Kitano, M.; Hosono, H. Unique Nanocages of 12CaO·7Al2O3 Boost Heterolytic Hydrogen Activation and Selective Hydrogenation of Heteroarenes over Ruthenium Catalyst. *Green Chem* **2017**, *19* (3), 749–756.

(34) Kitano, M.; Inoue, Y.; Yamazaki, Y.; Hayashi, F.; Kanbara, S.; Matsuishi, S.; Yokoyama, T.; Kim, S. W.; Hara, M.; Hosono, H. Ammonia Synthesis Using a Stable Electride as an Electron Donor and Reversible Hydrogen Store. *Nat Chem* **2012**, *4* (11), 934–940.

(35) Toda, Y.; Hirayama, H.; Kuganathan, N.; Torrisi, A.; Sushko, P. v.; Hosono, H. Activation and Splitting of Carbon Dioxide on the Surface of an Inorganic Electride Material. *Nat Commun* **2013**, *4* (1), 1–8.

(36) Huang, R. H.; Dye, J. L. Low Temperature (−80°C) Thermionic Electron Emission from Alkalides and Electrides. *Chem Phys Lett* **1990**, *166* (2), 133–136.

(37) He, H. M.; Li, Y.; Yang, H.; Yu, D.; Li, S. Y.; Wu, D.; Hou, J. H.; Zhong, R. L.; Zhou, Z. J.; Gu, F. L.; Luis, J. M.; Li, Z. R. Efficient External Electric Field Manipulated Nonlinear Optical Switches of All-Metal Electride Molecules with Infrared Transparency: Nonbonding Electron Transfer Forms an Excess Electron Lone Pair. *J Phys Chem C* **2017**, *121* (1), 958–968.

(38) Guan, S.; Huang, S. Y.; Yao, Y.; Yang, S. A. Tunable Hyperbolic Dispersion and Negative Refraction in Natural Electride Materials. *Phys Rev B* **2017**, *95* (16), 165436.

(39) Hosono, H.; Kim, S. W.; Matsuishi, S.; Tanaka, S.; Miyake, A.; Kagayama, T.; Shimizu, K. Superconductivity in Room-Temperature Stable Electride and High-Pressure Phases of Alkali Metals. *Philo Trans R Soc A* **2015**, *373* (2037).

(40) Hu, J.; Xu, B.; Yang, S. A.; Guan, S.; Ouyang, C.; Yao, Y. 2D Electrides as Promising Anode Materials for Na-Ion Batteries from First-Principles Study. *ACS Appl Mater Interfaces* **2015**, *7* (43), 24016–24022.

(41) Druffel, D. L.; Woomer, A. H.; Kuntz, K. L.; Pawlik, J. T.; Warren, S. C. Electrons on the Surface of 2D Materials: From Layered Electrides to 2D Electrenes. *J Mater Chem C* **2017**, *5*, 11196–11213.

(42) Liu, C.; Nikolaev, S. A.; Ren, W.; Burton, L. A. Electrides: A Review. *J Mater Chem C* **2020**, *8* (31), 10551–10567.

(43) Zhang, X.; Yang, G. Recent Advances and Applications of Inorganic Electrides. *J Phys Chem Lett* **2020**, *11* (10), 3841–3852.

(44) Hosono, H.; Kitano, M. Advances in Materials and Applications of Inorganic Electrides. *Chem Rev* **2021**, *121*, 3121–3185.

(45) Kraus, C. A. Solutions of Metals in Non-Metallic Solvents; Material Effects Accompanying the Passage of an Electrical Current through Solutions of Metals in Liquid Ammonia. Migration Experiments. *J Am Chem Soc* **1908**, *30* (9), 1323–1344.

(46) Dye, J. L.; Debacker, M. G. Physical and Chemical Properties of Alkalides and Electrides. *Ann Rev Phys Chem* **1987**, *38* (1), 271–299.

(47) Dye, J. L. Recent Developments in the Synthesis of Alkalides and Electrides. *J Phys Chem* **1984**, *88* (17), 3842–3846.

(48) Issa, D.; Dye, J. L. Synthesis of Cesium 18-Crown-6: The First Single-Crystal Electride? *J Am Chem Soc* **1982**, *104* (13), 3781–3782.

(49) Ellaboudy, A.; Dye, J. L.; Smith, P. B. Cesium 18-Crown-6 Compounds. A Crystalline Ceside and a Crystalline Electride. *J Am Chem Soc* **1983**, *105* (21), 6490–6491.

(50) Dye, J. L.; Yemen, M. R.; DaGue, M. G.; Lehn, J. M. Optical Spectra of Alkali Metal Anion and "electride" Films. *J Chem Phys* **1978**, *68* (4), 1665–1670. https://doi.org/10.1063/1.435932.

(51) van der Marck, S. C.; Diao, Y.; Hinson, K.; Arsuaga, J. Semi-Conductors with Partially and with Completely Filled 3d-Lattice Bands. *Proc Phys Soc* **1937**, *49* (4S), 59.

(52) Mott, N. F.; Peierls, R. Discussion of the Paper by de Boer and Verwey. *Proc Phys Soc* **1937**, 49 (4S), 72.

(53) Landau, L. D. Electron Motion in Crystal Lattices. *Phys Z Sowjet* **1933**, *3*, 664.

(54) Landau, L. D. The Movement of Electrons in the Crystal Lattice. *Phys Z Sowjet* **1933**, *3*, 644–645.

(55) Ward, D. L.; Huang, R. H.; Dye, J. L. Structures of Alkalides and Electrides. I. Structure of Potassium Cryptand[2.2.2] Electride. *Acta Crystallogr* **1988**, *44* (8), 1374–1376.

(56) Wagner, M. J.; Huang, R. H.; Eglin, J. L.; Dye, J. L. An Electride with a Large Six-Electron Ring. *Nature* **1994**, *368* (6473), 726–729.

(57) Huang, R. H.; Wagner, M. J.; Gilbert, D. J.; Reidy-Cedergren, K. A.; Ward, D. L.; Faber, M. K.; Dye, J. L. Structure and Properties of Li+(Cryptand [2.1.1])e-, an Electride with a 1D "spin-Ladder-like" Cavity-Channel Geometry. *J Am Chem Soc* **1997**, *119* (16), 3765–3772.

(58) Xie, Q.; Huang, R. H.; Ichimura, A. S.; Phillips, R. C.; Pratt, W. P.; Dye, J. L. Structure and Properties of a New Electride, Rb^+(Cryptand[2.2.2])e^-. *J Am Chem Soc* **2000**, *122* (29), 6971–6978.

(59) Matsuishi, S., Toda, Y., Miyakawa, M., Hayashi, K., Kamiya, T., Hirano, M., Tanaka, I., Hosono, H. High-Density Electron Anions in a Nanoporous Single Crystal : $[Ca_{24}Al_{28}O_{64}]^{4+}(4e^-)$. Science **2003**, *301*, 626–630.

(60) Miyakawa, M.; Kamioka, H.; Hirano, M.; Kamiya, T.; Sushko, P. v.; Shluger, A. L.; Matsunami, N.; Hosono, H. Photoluminescence from Au Ion-Implanted Nanoporous Single-Crystal $12CaO_7Al_2O_3$. *Phys Rev B Condens Matter Mater Phys* **2006**, *73* (20), 205108.

(61) Ye, T. N.; Xiao, Z.; Li, J.; Gong, Y.; Abe, H.; Niwa, Y.; Sasase, M.; Kitano, M.; Hosono, H. Stable Single Platinum Atoms Trapped in Sub-Nanometer Cavities in $12CaO{\cdot}7Al_2O_3$ for Chemoselective Hydrogenation of Nitroarenes. *Nat Commun* **2020**, *11* (1), 1–10.

(62) Miao, M. S.; Hoffmann, R. High-Pressure Electrides: The Chemical Nature of Interstitial Quasiatoms. *J Am Chem Soc* **2015**, *137* (10), 3631–3637.

(63) Matsuoka, T.; Shimizu, K. Direct Observation of a Pressure-Induced Metal-to-Semiconductor Transition in Lithium. *Nature* **2009**, *458* (7235), 186–189.

(64) Marqués, M.; Ackland, G. J.; Lundegaard, L. F.; Stinton, G.; Nelmes, R. J.; McMahon, M. I.; Contreras-García, J. Potassium under Pressure: A Pseudobinary Ionic Compound. *Phys Rev Lett* **2009**, *103* (11), 115501.

(65) Ma, Y.; Eremets, M.; Oganov, A. R.; Xie, Y.; Trojan, I.; Medvedev, S.; Lyakhov, A. O.; Valle, M.; Prakapenka, V. Transparent Dense Sodium. *Nature* **2009**, *458* (7235), 182–185.

(66) Dong, X.; Hou, J.; Kong, J.; Cui, H.; Li, Y. L.; Oganov, A. R.; Li, K.; Zheng, H.; Zhou, X. F.; Wang, H. T. Predicted Lithium Oxide Compounds and Superconducting Low-Pressure LiO_4. *Phys Rev B* **2019**, *100* (14), 144104.

(67) Zhang, W.; Oganov, A. R.; Goncharov, A. F.; Zhu, Q.; Boulfelfel, S. E.; Lyakhov, A. O.; Stavrou, E.; Somayazulu, M.; Prakapenka, V. B.; Konopkᷠová, Z. Unexpected Stable Stoichiometries of Sodium Chlorides. *Science* **2013**, *342* (6165), 1502–1505.

(68) Zhu, Q.; Oganov, A. R.; Lyakhov, A. O. Novel Stable Compounds in the Mg–O System under High Pressure. *Phys Chem Chem Phys* **2013**, *15* (20), 7696–7700.

(69) Chen, Y.-M.; Geng, H.-Y.; Yan, X.-Z.; Wang, Z.-W.; Chen, X.-R.; Wu, Q. Predicted Novel Insulating Electride Compound between Alkali Metals Lithium and Sodium under High Pressure. *Chinese Physics B* **2017**, *26* (5), 056102.

(70) Shao, S.; Zhu, W.; Lv, J.; Wang, Y.; Chen, Y.; Ma, Y. The Exotically Stoichiometric Compounds in Al–S System under High Pressure. *NPJ Comput Mater* **2020**, *6* (1), 1–6.

(71) Sushko, P. v.; Shluger, A. L.; Hayashi, K.; Hirano, M.; Hosono, H. Hopping and Optical Absorption of Electrons in Nano-Porous Crystal $12CaO{\cdot}7Al_2O_3$. *Thin Solid Films* **2003**, *445* (2), 161–167.

(72) Ahmad, I. Ca_2N, Imperial College of London, **1963**.

(73) Ariya, S.; Prokofyeva, E.; Matveeva, I. Investigation of Metallic Nitrides II. the Subnitrides of Strontium and Barium. *Journal of General Chemistry of the USSR* **1955**, *25*, 609–612.

(74) Keve, E. T.; Skapski, A. C. The Crystal Structure of Dicalcium Nitride. *Inorg Chem* **1968**, *7* (9), 1757–1761.

(75) Steinbrenner, U.; Adler, P.; Hölle, W.; Simon, A. Electronic Structure and Chemical Bonding in Alkaline Earth Metal Subnitrides: Photoemission Studies and Band Structure Calculations. *J Phys Chem Solids* **1998**, *59* (9), 1527–1536.

(76) Gregory, D. H.; Bowman, A.; Baker, C. F.; Weston, D. P. Dicalcium Nitride, Ca_2N - A 2D “excess Electron” Compound; Synthetic Rotates and Crystal Chemistry. *J Mater Chem* **2000**, *10* (7), 1635–1641.

(77) Brese, N. E.; O’Keeffe, M. Synthesis, Crystal and Physical Properties of Sr_2N. *J Solid State Chem* **1990**, *87*, 134–140.

(78) Reckeweg, O.; DiSalvo, F. J. Crystal Structure of Dibarium Mononitride, Ba2N, an Alkaline Earth Metal Subnitride. *Zeitschrift fur Kristallographie - New Crystal Structures* **2005**, *220* (1–4), 549–550.

(79) Atoji, M.; Kikuchi, M. Crystal Structures of Cubic and Trigonal Yttrium Hypocarbides; A Dimorphically Interphased Single-Crystal Study. *J Chem Phys* **1969**, *51* (9), 3863–3872.

(80) Zhang, X.; Xiao, Z.; Lei, H.; Toda, Y.; Matsuishi, S.; Kamiya, T.; Ueda, S.; Hosono, H. Two-Dimensional Transition-Metal Electride Y_2C. *Chem Mater* **2014**, *26* (22), 6638–6643.

(81) Kang, S. H.; Kang, S. H.; Bang, J.; Chung, K.; Nandadasa, C. N.; Han, G.; Lee, S.; Lee, K. H.; Lee, K.; Ma, Y.; Ma, Y.; Oh, S. H.; Kim, S. G.; Kim, Y. M.; Kim, Y. M.; Kim, S. W.; Kim, S. W. Water- And Acid-Stable Self-Passivated Dihafnium Sulfide Electride and Its Persistent Electrocatalytic Reaction. *Sci Adv* **2020**, *6* (23).

(82) Mudryk, Y.; Paudyal, D.; Pecharsky, V. K.; Gschneidner, K. A. Magnetic Properties of Gd2C: Experiment and First Principles Calculations. *J Appl Phys* **2011**, *109* (7), 2–5.

(83) Lee, S. Y.; Hwang, J. Y.; Park, J.; Nandadasa, C. N.; Kim, Y.; Bang, J.; Lee, K.; Lee, K. H.; Zhang, Y.; Ma, Y.; Hosono, H.; Lee, Y. H.; Kim, S. G.; Kim, S. W. Ferromagnetic Quasi-Atomic Electrons in Two-Dimensional Electride. *Nat Commun* **2020**, *11* (1), 1–8.

(84) Horiba, K.; Yukawa, R.; Mitsuhashi, T.; Kitamura, M.; Inoshita, T.; Hamada, N.; Otani, S.; Ohashi, N.; Maki, S.; Yamaura, J. I.; Hosono, H.; Murakami, Y.; Kumigashira, H. Semimetallic Bands Derived from Interlayer Electrons in the Quasi-Two-Dimensional Electride Y_2C. *Phys Rev B* **2017**, *96* (4), 045101.

(85) Oh, J. S.; Kang, C. J.; Kim, Y. J.; Sinn, S.; Han, M.; Chang, Y. J.; Park, B. G.; Kim, S. W.; Min, B. Il; Kim, H. Do; Noh, T. W. Evidence for Anionic Excess Electrons in a Quasi-Two-Dimensional Ca_2N Electride by Angle-Resolved Photoemission Spectroscopy. *J Am Chem Soc* **2016**, *138* (8), 2496–2499.

(86) Dale, S. G.; Johnson, E. R. Theoretical Descriptors of Electrides. *J Phys Chem A* **2018**, *122* (49), 9371–9391.

(87) Hu, Q.; Sun, D.; Wu, Q.; Wang, H.; Wang, L.; Liu, B.; Zhou, A.; He, J. MXene: A New Family of Promising Hydrogen Storage Medium. *J Phys Chem A* **2013**, *117* (51), 14253–14260.

(88) Hu, Q.; Wang, H.; Wu, Q.; Ye, X.; Zhou, A.; Sun, D.; Wang, L.; Liu, B.; He, J. Two-Dimensional Sc2C: A Reversible and High-Capacity Hydrogen Storage Material Predicted by First-Principles Calculations. *Int J Hydrogen Energy* **2014**, *39* (20), 10606–10612.

(89) He, T.; Pachfule, P.; Wu, H.; Xu, Q.; Chen, P. Hydrogen Carriers. *Nat Rev Mater* **2016**, *1* (12), 1–17.

(90) Schlapbach, L.; Züttel, A. Hydrogen-Storage Materials for Mobile Applications. *Nature* **2001**, *414* (6861), 353–358.

(91) Fan, L.; Tu, Z.; Chan, S. H. Recent Development of Hydrogen and Fuel Cell Technologies: A Review. *Energy Reports* **2021**, *7*, 8421–8446.

(92) Dash, S. K.; Chakraborty, S.; Roccotelli, M.; Sahu, U. K. Hydrogen Fuel for Future Mobility: Challenges and Future Aspects. *Sustainability* **2022**, *14* (14), 8285.

(93) Rivard, E.; Trudeau, M.; Zaghib, K. Hydrogen Storage for Mobility: A Review. *Materials* **2019**, *12* (12).

(94) Mori, D.; Hirose, K. Recent Challenges of Hydrogen Storage Technologies for Fuel Cell Vehicles. *Int J Hydrogen Energy* **2009**, *34* (10), 4569–4574.

(95) Crabtree, R. H. Hydrogen Storage in Liquid Organic Heterocycles. *Energy Environ Sci* **2008**, *1* (1), 134–138.

(96) Eberle, U.; Arnold, G.; von Helmolt, R. Hydrogen Storage in Metal–Hydrogen Systems and Their Derivatives. *J Power Sources* **2006**, *154* (2), 456–460.

(97) Aardahl, C. L.; Rassat, S. D. Overview of Systems Considerations for On-Board Chemical Hydrogen Storage. *Int J Hydrogen Energy* **2009**, *34* (16), 6676–6683.

(98) Zhang, J.; Fisher, T. S.; Ramachandran, P. V.; Gore, J. P.; Mudawar, I. A Review of Heat Transfer Issues in Hydrogen Storage Technologies. *J Heat Transfer* **2005**, *127* (12), 1391–1399.

(99) Asano, K.; Yamazaki, Y.; Iijima, Y. Hydriding and Dehydriding Processes of LaNi5−xCox (X=0–2) Alloys under Hydrogen Pressure of 1–5 MPa. *Intermetallics* **2003**, *11* (9), 911–916.

(100) Reilly, J. J.; Wiswall, R. H. Formation and Properties of Iron Titanium Hydride. *Inorg Chem* **1974**, *13* (1), 218–222.

(101) Zhou, S.; Chen, H.; Ding, C.; Niu, H.; Zhang, T.; Wang, N.; Zhang, Q.; Liu, D.; Han, S.; Yu, H. Effectiveness of Crystallitic Carbon from Coal as Milling Aid and for Hydrogen Storage during Milling with Magnesium. *Fuel* **2013**, *109*, 68–75.

(102) Huang, Y.; Cheng, Y.; Zhang, J. A Review of High Density Solid Hydrogen Storage Materials by Pyrolysis for Promising Mobile Applications. *Ind Eng Chem Res* **2021**, 2737–2771.

(103) Bachelet, G. B. Model Static Structure Factors and Pair-Correlation Functions for the Unpolarized Homogeneous Electron Gas. *AIP Conf Proc* **2003**, *577* (1), 21–37.

(104) Borlido, P.; Schmidt, J.; Huran, A. W.; Tran, F.; Marques, M. A. L.; Botti, S. Exchange-Correlation Functionals for Band Gaps of Solids: Benchmark, Reparametrization and Machine Learning. *NPJ Comp Mater* **2020**, *6* (1), 1–17.

(105) Sabnick, H. D.; Cocchi, C. Electronic Structure of Cesium-Based Photocathode Materials from Density Functional Theory: Performance of PBE, SCAN, and HSE06 Functionals. *Electronic Structure* **2021**, *3* (2), 027001.

(106) Johnson, E. R.; Otero-De-La-Roza, A.; Dale, S. G. Extreme Density-Driven Delocalization Error for a Model Solvated-Electron System. *J Chem Phys* **2013**, *139* (18), 184116.

(107) R. F. W. Bader. Atoms in Molecules. Encyclopedia of Computational Chemistry; *John Wiley & Sons, Ltd.*: Chichester, U.K., **2002**; 64–64.

(108) Druffel, D. L.; Pawlik, J. T.; Sundberg, J. D.; McRae, L. M.; Lanetti, M. G.; Warren, S. C. First-Principles Prediction of Electrochemical Electron–Anion Exchange: Ion Insertion without Redox. *J Phys Chem Lett* **2020**, *1*, 9210–9214.

(109) Schuch, N.; Verstraete, F. Computational Complexity of Interacting Electrons and Fundamental Limitations of Density Functional Theory. *Nat Phys* **2009**, *5* (10), 732–735.

(110) Rietveld, H. M. The Rietveld Method. *Phys Scr* **2014**, *89* (9).

CHAPTER 2: METHODS

2.1 Introduction

During my time at UNC-Chapel Hill, I have developed expertise in DFT, cluster expansion, high-temperature solid-state synthesis of 2D electrides, and powder x-ray diffraction with Rietveld refinement. Herein, I present details that are not included elsewhere in my dissertation. First, I discuss computational methods for understanding the structure and properties of bulk materials systems, including electrides. Second, I share my developed methods for the synthesis of novel 2D electride Sc_2C and subsequent hydrogenation. Third, I present the preparation and characterization of materials using powder x-ray diffraction and x-ray photoelectron spectroscopy.

2.2 Computational methods

2.2.1 Density Functional Theory

DFT is considered one of the best computational tools to explore the structure and properties of small molecules and crystalline systems. Therefore, in this dissertation, I discuss the application of DFT calculations to the prediction of electronic structure, structural kinetics, electrical and ionic conductivities, work function, and mechanical properties. Structure optimizations were performed in the Vienna *ab-initio* Simulation Package (VASP) using the projector-augmented wave (PAW) potentials to describe core electrons[1,2]. The generalized gradient approximation (GGA) PBE functional was used for relaxing structures and calculating energies[3], and the PBEsol functional was used to calculate lattice parameters[4]. A hybrid functional, HSE-06, was used to calculate the electronic structure[5].

For each DFT calculation, a structural relaxation was performed followed by a more rigorous single-point energy calculation using the desired functional before the calculation of any property. All calculations were set up using the Python Package for Materials Genomics software (PyMatGen)[6]. The plane-wave energy cutoff that should be used will depend on the system, but for all calculations on Sc_2CX_2 (X=e, F, H), I used 650 eV and a Monkhorst-Pack k-point grid. The break condition for the energy in the electronic SC-

loop in the relaxation steps was 10^{-8} eV and for the single point energy calculation was 10^{-9} eV. The zero damping DFT-D3 dispersion correction of Grimme was used to account for long-range van der Waals forces[7] and a U parameter correction of 3 eV was placed on Sc since the Sc *3d* orbitals are localized[8]. For a more complete discussion of the DFT-D3 method, see the dissertation of my colleague, Dr. Adam Woomer from the Scott Warren lab, section 2.5.2. A U parameter must be used to correct self-interaction for highly localized *d* and *f* orbitals on the *3d* and *4f* metals[9–15].

2.2.1.1 Electronic structure

There are two main features that I've calculated to understand the electronic structure of electride materials: the band structure and electron localization function (ELF). Rather than a GGA functional like PBE, which tends to underestimate the band gap, we must use a hybrid functional[16]. This underestimation occurs because the Hartree energy included when using Kohn-Sham orbitals has an unphysical self-interaction of the electron with itself[17]. Therefore, hybrid functionals, like HSE-06[5], that incorporate different fractions of Hartree-Fock exchange, are the most accurate predictors of band structure[18,19].

To calculate the band structure and density of states (DOS), I used the Materials Project[20] HSE band structure set to create my input files. I used "line" mode to create my k-point grid, which will run the band structure calculation along high symmetry points. This mode creates the grid with both a uniform grid with appropriate weights and a path along the lines weighted 0, which are necessary for self-consistency. To evaluate the band structure after the calculation, I used the PyMatGen band structure plotter tool to create a plot. Band structure and DOS can also be set up and evaluated with VASPKIT[21].

For most materials, calculating the projected density of states (PDOS) for each element is straightforward using PyMatGen; however, electrides have electron density outside the orbitals of any atom. Therefore, the electron density in these systems must be parsed by modeling the electride like an atom. To calculate the partial density of the electride states for Sc_2C, I identified a sphere with a radius 1.2 Å centered at the electride lattice site and integrated the charge density within this radius.

Lastly, to identify the existence of electride electrons, or electron density that isn't associated with surrounding atomic orbitals, I've calculated the ELF. This measures the degree of electron spatial localization compared to a reference electron with the same spin and provides a map of electron probability

across a system[22–24]. Calculating the ELF in VASP involves updating one flag, *LELF*, to true, which uses the scheme first introduced by Silvi & Savin[25]. This will output a file that can be visualized in various software, including VESTA[26].

2.2.1.2 Dynamic stability

Typically, DFT calculates a motionless lattice – at 0K – which approximates overall lattice energy and other equilibrium properties well; however, at finite temperatures, atoms will vibrate from their equilibrium position. Lattice vibrations are involved in a number of material properties and can be used to identify and characterize solid-state materials[27,28]. Therefore, I have combined DFT with lattice vibration calculations to model vibrational effects[29]. I've explored the dynamic stability in two ways: phonon mode calculations and *ab-initio* Molecular Dynamics (AIMD)[30].

Phonopy can be used to analyze the forces associated with a systematic set of displacements via two methods: finite displacement method (FDM)[31,32] or density functional perturbation theory (DFPT)[33,34]. DFPT and FDM give similar phonon modes for most systems[35], so I chose to run my calculations with FDM. I used Phonopy to build a supercell and output a series of structures with small atomic distortions. The supercell must be large enough to ensure there is no self-interaction of the displaced atom with itself, so I ensured each calculation was converged with respect to the supercell size. I then set up a single-point calculation for each in VASP, and used Phonopy again for post-processing and plotting the phonon band structure. The potential energy of any system should increase with atomic displacements, so if a structure contains imaginary or negative phonon modes, it is dynamically unstable. If all phonon modes are positive, it is dynamically stable.

Another approach to studying dynamic stability is AIMD, and this approach can be used in addition to the phonon mode calculations described. AIMD generates finite-temperature trajectories in which the forces are obtained from electronic structure calculations that are performed at each timestep[36]. A dynamically stable material should not undergo structural changes to lower its energy, so the structure should not change over a converged AIMD simulation. AIMD can be performed using VASP with a few flags to run AIMD (*IBRION=0*), no symmetry (*ISYM=0*), define the thermostat (*MDALGO=2* for the Nose-Hoover thermostat), set step-size (*POTIM=1* where the unit is fs), control velocity for the chosen algorithm

(*SMASS=1* for the canonical ensemble using the Nose algorithm), and the beginning and end temperatures of the simulation (*TEBEG/TEEND=300* where the unit is K). The potential energy at each time step can be obtained from the OSZICAR file.

2.2.1.3 Electrical conductivity

The VASP band structure can be used to calculate the electrical conductivity with the *ab-initio* scattering and transport (AMSET) software[37]. In the VASP calculations, the k-point mesh must be uniform rather than calculated along symmetry lines and the wave function coefficients must be calculated (by setting *LWAVE=true* in the INCAR); otherwise, the band structure input for AMSET is the same as the band structure calculation described in section 2.1.1.1. It is important to note that the k-point mesh must be large enough to converge the transport properties, and the typical k-point density will be at least twice that needed to converge the total energy. Additionally, the structure's elastic constants, deformation potential, dielectric constants, and polar-phonon frequency must be calculated.

The elastic constants are calculated by a non-SCF VASP calculation using FDM with *IBRION=6*. In its current version, VASP outputs the elastic constants separated into symmetrized elastic moduli and elastic moduli from ionic relaxation, and the total elastic constant is given by their sum. The output should be a matrix, which can be input into AMSET in its entirety.

The deformation potential is the change in band energy with volume change (Eqn. 2.1) and should be averaged over the contraction and expansion of the lattice for each component of the strain tensor[1].

$$D_{nk} = \frac{\delta \varepsilon_{nk}}{\delta S_{\alpha\beta}} \qquad (2.1)$$

In Eqn. 2.1, ε is the electron energy, n is the band index, k is a wave vector, α and β are denoted by Cartesian coordinates, and $S_{\alpha\beta}$ is the uniform stress tensor. AMSET includes a tool that will generate deformed structures as a list of POSCARs, each corresponding to a strain tensor[37]. Following the generation of POSCARs, a single-point energy calculation should be run using VASP, with *ICORELEVEL=1* to output core levels. After all calculations have finished, AMSET can read the output and write the deformation potential to a separate file.

Dielectric constants and the effective polar phonon frequency can be calculated using DFPT if using the PBE functional, and FDM if using a hybrid functional. DFPT can be run using a single-point energy calculation set-up with the flags *IBRION=8* and *LEPSILON=true*. There are two dielectric constants needed for AMSET calculations: the high-frequency dielectric constant, which is the value deduced from the refraction of electromagnetic waves with frequencies high compared to lattice vibrations, and the static-dielectric constant, which is the total dielectric screening from the high-frequency response and the vibrational response. The language used by VASP for the dielectric constants is not very precise. With a DFPT calculation, the OUTCAR will contain several dielectric constants, each with similar names. In the OUTCAR, the "macroscopic static dielectric tensor" is the high-frequency dielectric constant matrix and the "macroscopic static dielectric tensor ionic contribution" is the ionic contribution to the static dielectric matrix. To get the final static constant matrix, the high-frequency dielectric is added to the ionic contribution.

This OUTCAR will also contain the polar-phonon frequency. In the area labeled "Eigenvectors and eigenvalues of the dynamical matrix", there should be a value in THz, which is the polar-phonon frequency. In optical vibrations, atoms will vibrate against each other, which can cause polar effects[38,39]. This value is necessary to accurately model the transport characteristics in a crystal structure.

Once all of the values are obtained, they can be included in the input python script for AMSET along with the desired temperature range and several other inputs described in the AMSET documentation. The electrical conductivity is calculated from Eqn. 2.2, where e is the electron charge and ε is the electron energy.

$$\sigma_{\alpha\beta} = e^2 \int \sum\nolimits_{\alpha\beta}(\varepsilon) \left[-\frac{\partial f^0}{\partial \varepsilon}\right] \partial\varepsilon \qquad (2.2)$$

2.2.1.4 Work function

The work function is defined as the minimum energy required to remove an electron from the Fermi level of a solid to the vacuum level following Eqn. 2.3, where V_{el} is the electrostatic potential energy of the electron at the vacuum level[40], ΔV_{el} is the mean electrostatic potential across the material surface, and E_F is the Fermi level relative to the mean electrostatic potential energy in the material interior.

$$W = \Delta V_{el} - E_F \quad (2.3)$$

The work function can be calculated using this expression by calculating the Fermi level of thin slabs with respect to the potential of the vacuum region[41]. To accomplish this, I used PyMatGen to build thin slabs and ran VASP to relax the structure and get accurate energies. Post-processing involved pulling the Fermi level from the OUTCAR and using VASPKIT[21] to calculate the vacuum level. Lastly, the work function can be calculated by taking the difference between the vacuum and Fermi levels. These values should be converged with respect to the number of layers. For Sc_2C, work functions from thin slabs of 12 (hkl) planes surrounded by 12 (hkl) planes of vacuum were calculated.

2.2.1.5 Mechanical properties

Mechanical properties of materials show their response/deformation to an applied force[42], and those that can be calculated using VASP include interlayer and intralayer stiffness tensors, bulk modulus, shear modulus, Young's modulus, and Poisson's ratio. The stiffness tensors measure the metal's resistance to deformation in the interlayer and the intralayer, respectively. The bulk modulus defines the material's response to hydrostatic pressure at a constant temperature. This is shown in Eqn. 2.4, where *K* is the bulk modulus, *V* is the initial material volume, and *P* is the pressure.

$$K = -V\frac{dP}{dV} \quad (2.4)$$

The shear modulus, or the modulus of rigidity, describes the material's response to a load applied tangentially to shear it off across the resisting section[43]. Eqn. 2.5 shows how this value is calculated, where *G* is the shear modulus, *F* is the force, *A* is the area on which the force is acting, *l* is the initial length, and *Δx* is the transverse displacement.

$$G = \frac{Fl}{A\Delta x} \quad (2.5)$$

Young's modulus, or the modulus of elasticity, describes a material's resistance to elastic deformation. Eqn. 2.6 defines the modulus *E* as the relationship between compressive stress *σ* and axial strain *ε*.

$$E = \frac{\sigma}{\varepsilon} \quad (2.6)$$

Lastly, Poisson's ratio measures the Poisson effect, which is the expansion or contraction of a material in the directions perpendicular to the direction of the force. Eqn. 2.7 defines Poisson's ratio (v), where ε_{trans} is the transverse strain and ε_{axial} is the axial strain.

$$v = -\frac{\varepsilon_{trans}}{\varepsilon_{axial}} \tag{2.7}$$

These values can be calculated using VASPKIT to set up and process the calculations and VASP to run the calculation. VASPKIT is used to create the k-point grid and set up calculations within a strain range that I input. A DFT optimization and single-point energy calculation are then run in each directory (containing different strain values). Finally, VASPKIT performs post-processing and the property values are output into the terminal. All values will be calculated using three different methods, but I used the method described in Hill[44] because it combines the methods of Voigt[45] and Reuss[46] to give the most accurate value.

2.2.1.6 Diffusion analysis

To understand the diffusion of ions in a crystal structure, I performed nudged elastic band (NEB) calculations[47]. These calculations are based on transition state theory, which asserts that the transition state can be obtained using a statistical approach. This is founded on two basic assumptions: the transition rate is slow enough that a Boltzmann distribution is maintained and a dividing surface (with dimensionality of *n-1*, where *n* is the number of degrees of freedom) can be found so that the trajectory from the initial to final state only crosses the surface once[48–50]. In crystalline systems, the typical temperature of interest is much lower than the melting temperature, so this simplifies the estimation of rates[51]. Estimation requires finding the lowest saddle point along the potential energy basin edge containing the initial state, or the minimum energy path. To find this path, I used the image-dependent pair potential surface, which will relax the midpoint structures prior to NEB to improve our starting point[52]. NEB includes a force projection to ensure spring forces do not interfere with the convergence of elastic band to the minimum energy path. This includes only the perpendicular component to the true force and the parallel component to the spring force, which allows the images and surrounding atoms to relax and better estimate the true energy of the transition state[53].

2.2.1.7 DFT methods for Chapter 3

DFT calculations were performed using the CASTEP[54] code with plane-wave basis set approximations, except where noted. To describe core electrons, ultrasoft pseudopotentials[55] were used with a cut-off energy of 500 eV. For this cut-off energy, calculations were convergent with $dE_{tot}/dlnE_{cut}$ less than 0.01 meV/atom. Geometry optimizations of all structures were performed first. A GGA PBE functional[4] was used for the exchange-correlation contribution to total energy, and Tkatchenko and Scheffle's correction[56] was used to account for long-range dispersion forces for all calculations except where noted. A Monkhorst-Pack grid[57] of 16×16×8 k-points was used and structures were optimized using a BFGS algorithm with a convergence tolerance of 5.0×10^{-7} eV/atom for energy, 0.01 eV/Å for max force, 0.02 GPa for max stress, and 5.0×10^{-4} Å for max displacement. For the calculations of the activation barrier for F^- diffusion, we used a 3×3×2 supercell with a single fluorine atom removed and an anionic electron occupying its tetrahedral F^- site ($Y_2CF_{1.94}(e^-)_{0.06}$). Periodic images were separated by 10.8 Å to minimize self-interactions. The positions of the atoms in the starting and ending structures were geometry optimized with the lattice fixed using the parameters described above but with a Monkhorst-Pack grid of 5×5×4 k-points. The transition state was identified using the complete linear synchronous transit/quadratic synchronous transit (LST/QST) method[58] and confirmed using the NEB method[59] with a convergence tolerance of 1.0×10^{-5} eV/atom for energy, 0.05 eVÅ for max force, 0.04 GPa for max stress, and 7.5×10^{-5} Å for max displacement. Projected density of states and band-decomposed charge densities were calculated with the $Y_2CF_{1.94}(e^-)_{0.06}$ structures determined from NEB analysis using VASP[60] with PAW[61] PBE potentials and a DFT-D3[2] van der Waals correction. Calculations used an energy cut-off of both 500 eV and 600 eV in both spin-polarized and non-spin-polarized forms. Non-spin-polarized calculations were performed with a Monkhorst-Pack mesh density of 0.020 2π/Å, while spin-polarized calculations used a density of 0.025 2π/Å. All calculations used Gaussian smearing with a width of 60 meV. The calculation used 576 bands and 713 electrons. Calculations were converged to 1.0×10^{-7} eV/atom for energy. No residual spin density was found using spin-polarized calculations and all results were identical to non-spin-polarized calculations. Projected density of states (PDOS) was performed using radii determined from Bader charge densities in $[Y2C]^{2+}(e^-)_2$ and Y_2CF_2. The C, Y, and F radii used throughout all calculations were 1.632, 1.553, and 1.515 Å, respectively. In the case of Y_2CF_2, these radii led to oxidation states in C, Y, and F of -2.06, +1.91, and

-0.88. This analysis revealed oxidation states of Y, C, and F for the $Y_2CF_{1.94}(e^-)_{0.06}$ structures reported in Table 2-1. In the case of $[Y2C]^{2+}(e^-)_2$, these radii led to oxidation states in C and Y of -2.10, +1.95, from which an electride electron density of 1.80 electrons per Y_2C was calculated. These oxidation states are identical to values reported previously[62,63]. The isosurfaces in Figure 2-1 were plotted with an electron density of 0.0036 e− per Å^3. To examine the electron density at compositions close to $[Y_2C]^{2+}(e^-)_2$, we used the same methods to calculate oxidation states and electron distributions using 3×3×2 supercells with a single F atom. As in the compositions close to Y_2CF_2, the oxidation states and electron distributions of the composition close to $[Y_2C]^{2+}(e^-)_2$ do not change throughout the process of EAX (Figure 2-1).

Table 2-1. Charges on the constituent atoms in the Y_2C system for $[Y_2C]^{2+}(e^-)_2$ taken from literature, Y_2CF_2 calculated using Bader charge analysis, Y_2CF_2 calculated using WS-LDOS charge analysis, and F^--deficient Y_2CF_2 in its ground-state (GS) and its transition state (TS, with F^- halfway between tetrahedral sites) calculated using PDOS charge analysis. The oxidation states for the F^--deficient Y_2CF_2 are reported as an average and with the atoms nearest to the electron-anion exchange ("proximal").

Atoms	Charges			
	$[Y_2C]^{2+}(e^-)_2$ PDOS	Y_2CF_2 Bader PDOS	$Y_2CF_{1.94}(e^-)_{0.06}$ GS PDOS Average Proximal	$Y_2CF_{1.94}(e^-)_{0.06}$ TS PDOS Average Proximal
Y	+1.94	+ 1.91 +1.95	+1.87 +1.77	+1.89 +1.79
C	-2.04	-2.14 -2.10	-2.11 -2.07	-2.12 -2.07
e/F	-0.91	-0.85 -0.88	-0.88 -0.80	-0.88 -0.85

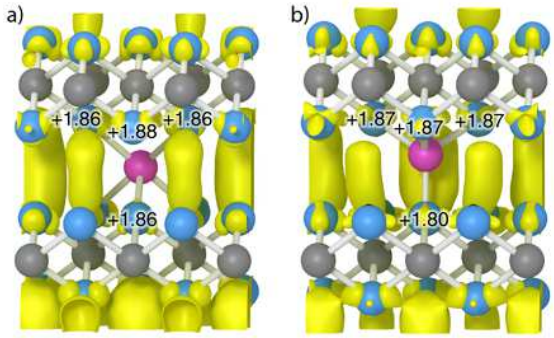


Figure 2-1. Electron density isosurfaces at the Fermi level (± 0.1 eV vs. E_f) for a single F atom in a 5×5×1 supercell of Y_2C. a) Ground state of F in Y_2C, showing F in an octahedral coordination geometry. b) Transition state of F in Y_2C, showing F in a tetrahedral coordination geometry. The largest change in the oxidation state of the surrounding Y atoms is 0.086. The isosurfaces are plotted with an electron density of 0.015 e− per Å^3.

2.2.2 Evolutionary algorithm

Evolutionary algorithms can be used to predict stable and metastable phases within a given materials system on small unit cells (<30 atoms). A detailed description of evolutionary algorithms is not within the scope of this thesis; for a more detailed explanation, see the dissertation of my colleague Dr. Jack Sundberg from the Scott Warren lab, chapter 6.

2.2.2.1 USPEX

I explored the phase diagram of Sc-C computationally using the Universal Structure Predictor: Evolutionary Xtallography (USPEX) software[64]. Structure optimizations were performed in VASP with the PBE functional. I performed convergence tests for each USPEX structure. I ran a variable composition USPEX calculation where we allowed 5-10 atoms in the unit cell, and each generation had 1000 structures. The calculation for Sc-C ran for 60 generations before stopping, producing 60,000 structures. I found that there were many compositions with structures close to the hull, so we then ran fixed composition calculations on these compositions, where we explored unit cells up to 25 atoms.

2.2.3 Cluster expansion

While evolutionary algorithms are known to correctly predict phase diagrams for ordered systems (small unit cells), DFT is too computationally costly to run on structures with a high amount of disorder (which must be modeled with larger unit cells). Additionally, DFT predicts energies at 0K, but we want to study phases at a finite temperature in a real system. Given this, a statistical method – cluster expansion – for predicting the energy of disordered systems at non-zero temperature has been developed[65–70].

Cluster expansion assumes that we can express the energy of a lattice as a sum of various atomic clusters and is based on the Ising model, which describes discrete variables as classical spins (+1 or -1) on a lattice. The one-dimensional model was originally solved in Ising's thesis[71]. In Ceder's 1993 paper[72], they demonstrate that the ferromagnetic Ising model, where neighboring spins interact, works well for modeling phase diagrams. In Ceder's study, they assume the lattice is fixed with a spin variable of σ_p on each lattice site p. The spin can only have one vector (+1 or -1), and these indicate the occupation of the site by either an A or B atom; therefore, the traditional Ising model can only be used to describe a binary system. The Ising Hamiltonian (Eqn. 2.8) in this case assumes that only nearest neighbor spins interact

with each other, where α is a collection of lattice sites (cluster), σ_α is a product of all spins in the cluster, and J_α is the effective cluster interaction (ECI) for the cluster.

$$E = \sum_{\alpha} J_\alpha \sigma_\alpha \qquad (2.8)$$

The product of spins (Eqn. 2.9) is made up of the occupation variable σ on each lattice site (in a binary system, this will represent either atom A or B). *i, j,…l* are all elements of cluster α. In simpler terms, the identity of each atom in the cluster (A or B) will be considered by this variable.

$$\sigma_\alpha = \sigma_i \sigma_j \ldots \sigma_l \qquad (2.9)$$

For multinary systems, Sanchez *et. al.*[73] describes an alternative occupation variable that can take values of ±*m*, ±*(m-1), … ±1 for M=2m* for an even number of element types, or a value of 0 and a relationship of *M=2m-1* for an odd number of element types. As an example, if we want to explore a system with four element types, the possible occupation variables are ±*1* and ±*2.* This has been used to describe ternary and quaternary systems.

Eqn. 2.8 indicates that each possible cluster of atoms within a superstructure will have a different ECI value based on its arrangement of atoms. Ideally, the ECI value for every cluster would be calculated; however, in practice, this must be condensed because there are too many possible clusters. Determining the ideal (number of) clusters has been studied in great depth, and genetic algorithms have been the most robust selectors[74-78]. Typically, the ECI values can be determined by fitting the values to the energy of a small number of configurations, which is known as the structure inversion method[79]. One important consideration for building the cluster expansion model is determining which ECI values and energies are used to fit. Here, I provide an explanation based on van de Walle and Ceder's work[80].

There are many interactions between atoms in a cluster that must be modeled by the ECI value to accurately predict the energy of a superstructure. The simplest interaction is in a two-body cluster, in which the energy is determined by bond vibrations and bond rotations. For a three-body cluster, the interactions between all constituent atoms, in addition to bond angle, must be considered to accurately predict its energy. As the number of atoms in a cluster increases linearly, the number of parameters that must be modeled to accurately predict the energy increases exponentially. Therefore, the true system (with a large

number of atoms) can't be described exactly with a finite number of ECI. Thus, we must find a good approximation with as few ECIs as possible; the predicted energies may be incorrect if insufficient ECIs are used, and overfitting can occur if too many ECIs are used. Given this, we must evaluate the predictive power using a cross-validation (CV) score (Eqn. 2.10)[81], where the calculated energy for each structure *i* is compared to the predicted energy of structure *i* obtained from the least squares fit.

$$CV = n^{-1}\sum_{i=1}^{n}\left(E_i - \hat{E}_{(i)}\right)^2 \qquad (2.10)$$

The CV score differs from the mean squared error because it does not monotonically decrease. The CV scoring method allows us to avoid partitioning data arbitrarily; instead, it is adequate to remove one point at a time, typically called the leave-one-out (LOO) scheme. While this method involves removing one point from the fit, the CV score does give a measure of the fit's predictive power for all structures[81,82].

Once the ECI values have been determined, numerous statistical mechanics methods, including Monte Carlo simulations[83], can be used to obtain phase diagrams[84-86]. With only a few ECIs in the expansion, one can obtain a phase diagram giving stable superstructures at 0K. Above 0K, several types of excitations are possible: vibrations, interatomic excitations, and substitutional excitations. Only substitutional excitations change the spin configuration, so all other excitations do not affect the Ising lattice. Therefore, higher temperatures can still be modeled well with a small number of ECIs.

Cluster expansion must predict ground state energies as accurately as possible. Accurate ground state energies are more important than accurate metastable structures' energies because the ground state energies create the phase diagram. Because CV measures all energy values equally, the lowest CV won't necessarily make the best possible prediction of ground states[87]. Therefore, a candidate cluster expansion with a higher CV score but correct ground state prediction will be chosen over a cluster expansion that has a lower CV score but incorrect ground state prediction.

Structure selection is another important consideration when building a cluster expansion model. Ideally, one would choose to add a structure that reduces the prediction error of the CV. However, this would require knowledge of the structure's energy, which is impractical because we have not yet calculated this value. The CV can be separated into 2 components: systematic bias and variance (fluctuations around

the mean ECI). Systematic bias cannot be reduced without knowledge of the structure, but the variance can be estimated. To see, the derivation for variance estimation, refer to van de Walle and Ceder's publication[80]. Estimating the variance allows us to predict the change in the fit by adding a new structure, but even still, minimizing the variance will not necessarily predict ground states correctly.

To tackle this, when constructing the cluster expansion model, a large number of structures generated are left out of the fit and these are checked to determine whether they are ground-state structures. If multiple new ground-state structures are predicted, we only use for the most variance-reducing structure amongst the newly predicted ground states. Additionally, CV works better on a smaller input dataset because as the number of cluster selections rises, the probability rises of one suboptimal selection giving a smaller CV score than the correct choice. Thus, we typically limit our search only to "physically meaningful" candidates.

2.2.3.1 CLEASE

Using the methodology described in section 2.2.3, Chang *et. al.* developed the cluster expansion in atomic simulation environment (CLEASE) package[88], combining cluster expansion with the already-built atomic simulation environment (ASE). Building off of ASE has two advantages: features implemented in ASE can also be used in CLEASE, and the language between the two is the same so users do not need to learn a new package. Below, I will discuss a few techniques within CLEASE that I have used when building/using my cluster expansion model. For a more in-depth discussion of the possible implementations within CLEASE, refer to the publication[88].

In CLEASE, the selection of relevant clusters is done using compressive sensing[89], which can select clusters using a small amount of data. It also is advantageous as it can tolerate noise in the input data. l_1 describes the Manhattan distance, which is calculated as the sum of absolute vector values and is mathematically described by Eqn. 2.11.

$$l_1(v) = |v_1| + |v_2| + \cdots |v_n| \qquad (2.11)$$

In the vector norm equations, v is a vector value, and n is the number of vectors. l_2 describes the Euclidean distance, which calculates the distance between two real vectors and is mathematically described by Eqn. 2.12.

$$l_2(v) = \sqrt{{v_1}^2 + {v_2}^2 + \cdots {v_n}^2} \tag{2.12}$$

CLEASE uses these regularization terms (Eqn. 2.11 or Eqn. 2.12) in conjunction with the ordinary least squares method to select the clusters that minimize the residual sum of squares. l_1 is advantageous as it promotes using the least number of clusters possible to find a reasonable solution, which helps to avoid overfitting; however, it must be solved iteratively, so l_2 can be used to more easily find a solution. For my work, I have used l_1 as it tends to give me the best fit, but one can fit with both schemes to decide which works best for any system.

In addition to selecting clusters, a CV must be used to assess the predictive power of the cluster expansion model. The most common CV technique used in the cluster expansion community is the LOO scheme (Eqn. 2.13), which I used when running CLEASE.

$$LOOCV = \left(\frac{1}{N_{config}} \sum_{i=1}^{N_{config}} (\hat{q}_i - q_i)^2 \right)^{1/2} \tag{2.13}$$

N_{config} is the number of configurations in the training set, $\hat{q}_i$ is the physical quantity of structure i predicted by cluster expansion using $N_{config} - 1$ structures without a structure i, and q_i is the calculated quantity of structure i. We use the CV score to ensure that our cluster expansion model accurately predicts structural energies, so in general, we want to minimize our LOOCV score. CLEASE also supports the use of *k-fold* CV, where the pool of configurations is randomly partitioned into k equal-sized portions. Structures in all but one portion are used to train the data while the last portion is used as validation, and this is done until each portion has been used as the validation set. This CV technique is popular among the machine learning community because they tend to have large amounts of training data; however, because we tend to have a small amount of input data, I used the LOOCV scoring scheme.

In addition to training a model with DFT data, which I have calculated using VASP, the finished model can be used to run Monte Carlo simulations, which can calculate energies at finite temperatures by

predicting the free energy G with Eqn. 2.14, where Z is the partition function, $\beta=1/k_BT$, k_B is the Boltzmann constant and T is the temperature in Kelvin.

$$G = -\frac{lnZ}{\beta} \tag{2.14}$$

DFT energies are found for fully relaxed structures with no external forces, so the thermodynamic quantities have a fixed number of particles, fixed pressure, and fixed temperature, and volume fluctuations must be neglected. The free energy can then be obtained by a thermodynamic integration at a reference temperature β_{ref} where free energy is known. This is written as Eqn. 2.15, where U is internal energy.

$$\beta G = (\beta G)_{ref} + \int_{\beta_{ref}}^{\beta} d\beta' U(\beta') \tag{2.15}$$

Using canonical Monte Carlo simulations – fixed composition – over several different compositions, a phase diagram can be obtained. CLEASE will output the lowest energy for each composition, which can be used to build a phase diagram. Semi-grand canonical Monte Carlo simulations – fixed number of atoms with varying composition – can be used to calculate a voltage profile when run over many potentials. CLEASE will output the lowest energy composition at each potential, which can be used to generate the voltage profile. Because the program will calculate this, I did not have to perform the thermodynamic integration myself.

2.2.3.2 CLEASE with Simmate

Using a framework that I helped develop, Simmate[90], we have integrated CLEASE into an automated workflow that can run cluster expansion model calculations with minimal manual inputs. This workflow requires the user to input a structure file that can be read by Simmate (cif or POSCAR), the formula for each atom (for $Y_2CF_xX_{x-1}$ where X is a vacancy site, Y=2, C=1, F=x, X=x-1), the variable range (0<x<1), the cluster diameter, the maximum number of atoms in a supercell, the number of structures per generation, and the convergence limit. Given this input, Simmate will create structures in an initial generation using CLEASE, set-up and run a low-quality geometry optimization followed by a high-quality optimization and a high-quality single-point energy calculation on each structure using VASP and previously developed Simmate workflows, followed by the analysis of data using CLEASE. Simmate will use the analysis to

determine whether another generation should be run according to the convergence criteria, and rerun the workflow if the criteria was not met.

While this workflow is still in the development stage, we have run successful tests with small structures (<50 atoms) using single-point energy calculations locally. I have not yet integrated the ability to run subsequent Monte Carlo simulations, but that will be included in a future version of this workflow.

2.3 Synthesis methods

Informed by my calculations, I developed two synthetic methods during my Ph.D. to create novel materials. In this section, I will describe these methods, which were based on the syntheses of similar materials that had been made previously (Y_2C[62], Y_2CH_2[91]) but adapted to fit the new systems. All steps were performed under inert atmosphere (Ar).

2.3.1 Sc_2C

Before use, scandium (Alfa Aesar, distilled dendritic, 99.9%) was arc-melted to form one large piece of scandium, which facilitates subsequent arc-melting. The scandium was combined with graphite (Sigma-Aldrich, ~100 mesh flakes, 99.9%) in a typical ratio of 67.3 at. % and 32.7 at. % for scandium and graphite, respectively. This includes a slight excess of scandium (<1 at. %) to account for scandium ablation in the melting process. The pellet after melting was loosely wrapped in Ta foil (Sigma-Aldrich, 0.025 mm thick, ≥99.9%) and sealed in a fused quartz ampule under 1 mBar Ar. The ampule was then heated to 1373 K at a ramp rate of ~3.5 K/min. The temperature was held for 7 days and then cooled back to room temperature at the same rate. The pellet was then ground into a powder in a mortar and pestle for further analysis. Longer annealing times (10 days) did not improve the layered content in the product.

We attempted to increase sample purity using a titanium sponge (Alfa Aesar, 3-19mm, 99.95%) to leach oxygen from the reaction containers. The sponge was present in both the arc-melting and the annealing steps. This inclusion showed no significant improvement in the layered content of the product. Given this information, we concluded that the impurities favoring the cubic phase must be present in the reactants.

2.3.2 Hydrogenation of Sc_2C

Hydrogenation has been performed previously with solvents[92-94], under pressure[92,95], and under a hydrogen plasma[96]. It's also been demonstrated that temperature can be tweaked to induce hydrogenation[97]. Given my previous experience running high-temperature syntheses, I sought to perform a synthesis using elevated temperature and atmospheric pressure. Therefore, I ran DFT calculations to get the enthalpy for the reaction of $Sc_2C(s) + H_2(s) \rightarrow Sc_2CH_2(s)$ and I estimated the entropy of $H_2(g) \rightarrow H_2(s)$ from the NIST thermochemical tables[98]. This information determined that we could run this reaction up to 973 K.

With this, I used our in-lab chemical vapor deposition (CVD) setup to attempt this reaction. I used a large half tube of quartz to run the reaction and cleaned it by washing with isopropyl alcohol and heating the tube to 773 K under vacuum (~0.09 torr) for 5 hours, with an additional 3 hours to ramp up and cool down. I then ground my powder finely to create a high surface area for the reaction to occur and transferred my sample directly into the half tube after grinding. I have tried the reaction with a Ta boat made of foil (Sigma-Aldrich, 0.025 mm thick, ≥99.9%), but the boat would become brittle during the reaction and disintegrate, mixing into the sample and making it harder to analyze. I have found that the sample doesn't react sitting directly in the quartz tube. With that, I attached the sample tube to the CVD and open it to argon gas at 760 torr. I ramped it up in the furnace to 973 K over 3 hours, then open it to a 5% H_2, 95% Ar mixture of gases. This was kept at 973 K, 760 torr for 7 days, then brought back under argon to ramp down over 3 hours.

2.4 Characterization methods

All analyses were performed under inert atmosphere (Ar) except for studies of sample oxidation.

2.4.1 Powder x-ray diffraction with Rietveld refinement

Powder x-ray diffraction (PXRD) is a non-destructive analytical technique used to identify phases and provide quantitative structural information in a powdered, multi-crystalline sample. I used a Bragg-Brentano geometry for all samples described. For a more in-depth discussion of the theory of diffraction, see the dissertation of my colleague, Dr. Dan Druffel from the Scott Warren lab, section 2.3.1. Instead, this dissertation will provide an in-depth discussion of phase identification and quantification using PXRD.

An ideal powder contains many single crystals in every possible orientation according to a perfect statistical distribution. A single PXRD diffraction pattern can give considerable information about the crystal structure contained in the analyzed sample. There are five fitting parameters necessary for fitting the diffraction pattern: peak position, width, intensity, shape, and asymmetry[99].

The peak position is typically defined as the position of maximum intensity. In practice, the position can be calculated either by taking the position of maximum intensity or the center of gravity; for my refinements, I used the former. The position of diffraction peaks is related to the crystal structure by Bragg's Law (Eqn. 2.16), which defines the angles at which constructive interference will occur. In the UNC Rigaku diffractometer, the x-ray wavelength λ is fixed; therefore, specific diffraction peaks will be produced by families of planes. d_{hkl} is a vector drawn from the origin to a plane, intersecting it orthogonally.

$$n\lambda = 2d_{hkl}\sin\theta \qquad (2.16)$$

Peak width occurs because, in real crystals, there is diffraction intensity from angles that differ slightly from the ideal Bragg angle. Therefore, the physical reason for peak width is defects and deviation from the ideal in crystals. This phenomenon is described by Scherrer's equation (Eqn. 2.17), which purports that for an infinitely thick crystal, one can always find a lattice plane with totally destructive interference for an angle that slightly deviates from the ideal Bragg angle. In Eqn. 2.17, τ is the mean domain size, K is a shape factor, λ is the x-ray wavelength, β is the line broadening at full width at half maximum (FWHM), and θ is the Bragg angle.

$$\tau = \frac{K\lambda}{\beta\cos\theta} \qquad (2.17)$$

The FWHM, which is the distance between points on a function where the function reaches half its maximum value, is typically used to describe the peak width. As an example, for a simple Gaussian function, the FWHM function is given by Eqn. 2.18, where σ is the standard deviation. Peak broadening can be indicative of small crystallite sizes, defects, an inhomogeneous composition, or apparative broadening. Apparative broadening could be caused by numerous effects, including equatorial effects (caused by everything parallel to the diffraction plane), axial effects (caused by everything perpendicular to the diffraction plane), effects of the sample and sample preparation, microstructure, and microstrain.

$$FWHM = 2\sqrt{2ln2}\sigma \quad (2.18)$$

Peak intensity gives information about both the diffractometer and the sample, but because we keep conditions in the diffractometer constant, we focus on sample effects. At the most basic level, intensity records the number of peaks hitting the detector, and can either be calculated by taking the integral intensity or maximum intensity (we use this one). Intensity can be described by Eqn. 2.19, where J_k is intensity, s is a scaling factor, F_k is the structure factor, LP_k is the Lorentzian factor & polarization, A_k is the absorption correction, E_k is the extinction correction, H_k is the multiplicity of reflection, and O_k is the factor for preferred orientation.

$$J_k = s \cdot F_k^2 \cdot LP_k \cdot A_k \cdot E_k \cdot H_k \cdot O_k \quad (2.19)$$

The scaling factor takes measurement time and phase fraction into account. The structure factor depends on the crystal structure and is defined by Eqn. 2.20, where N_j is the occupation factor, f_j is the atomic form factor, j is the atoms, and B_j is the thermal motion of nuclei, which smears the electron shell. The atomic form factor drives the decrease in the intensity of high-angle reflections.

$$F_k = \sum_j N_j \cdot f_j \cdot e^{-B_j \frac{\sin^2\theta_k}{\lambda^2}} \cdot e^{i\cdot\phi_k} \quad (2.20)$$

The Lorentzian factor results from the dispersion of wavelength and the geometry of the instrument, while the polarization is a result of partial polarization of the scattered beam. Without a monochromator, this will not need refinement. The absorption correction causes a loss of intensity described by the Lambert-Beer law (Eqn. 2.21), where A is the absorption, ε is the molar absorptivity, b is the path length, and C is the concentration. This is highly important for textured surfaces, where rough surfaces will cause low diffraction angles to be more highly weakened than high angles. In this case, an angular-dependent intensity correction should be adopted.

$$A = \varepsilon bC \quad (2.21)$$

The extinction correction is typically due to backscattering and can normally be ignored. The multiplicity of reflection is the number of symmetry-equivalent reflections that contribute to a single peak, and will typically not require refinement. Finally, the preferred orientation factor will account for some powder morphologies

which deviate from the ideal random particle distribution. This factor will be affected by the texture of the sample and will cause some reflections to be higher intensity than others, typically within a family of planes. We use the March-Dollase equation[100,101] (Eqn. 2.22) to get an angle of preferred orientation (O_k), where α is the angle between the scattering vector and preferred orientation, and G_1 is the only refineable parameter in the model of particles.

$$O_k = \left(G_1^2 \cdot \cos^2 \alpha + \left(\frac{1}{G_1} \cdot \sin^2 \alpha \right) \right)^{-1.5} \quad (2.22)$$

Intensity misfits can be refined by changing atomic charges, stoichiometry, doping, positional parameters, and the space group subgroup. It is important, however, to avoid overparameterization; in summary, one should avoid refining a parameter unless there is an indication within the physical model that it is necessary.

Peak shape can give information about crystallite size/strain and defects. Ideally, the peaks should be sharp, but any tails present characterize the extremities as they approach zero intensity; these tails provide a test of how well a peak fits any function. Peaks can be fit by a Lorentzian function (larger tails), Gaussian function (smaller tails), or something in between. Commonly used convolutions of Gaussian and Lorentzian functions include a Voigt, Pseudo-Voigt, and Pearson VII. I used a Pseudo-Voigt function, or a linear combination of Gaussian and Lorentzian, for my fittings. These functions will describe all of the above parameters except asymmetry. There has been some experimental and theoretical evidence purporting that the Gauss contribution arises from strain while the Lorentzian contribution arises from crystalline domain size[102-109].

Lastly, the most common effects on peak asymmetry are instrumental set-up[110], sample absorption[111], or sample geometry[112]. One example of instrumental set-up causing peak asymmetry occurs when the slits are fixed; when one keeps slits fixed over the entire scan, a larger irradiation area on the lower angle side of peaks causes a higher intensity on the low-angle side compared to the high-angle side[99].

Many of the physical phenomena driving these parameters have an angular dependence, so the diffraction pattern will need to be fit differently at low vs. high angles. Microstructure and microstrain both have an angular dependence, so typically, it is important to measure a standard material with negligible

broadening due to crystallite size or strain to get an idea of the instrument function before measuring an unknown sample[113].

After the parameters have been fit well to the observed diffraction pattern for phase identification, the Rietveld method can be used for quantification[114]. The most important considerations one should make when measuring a sample for quantitative refinement are sample preparation and scan time. The sample must have extremely small crystallite sizes (between 1-5μm is sufficient) to avoid microabsorption and the sample should be as smooth as possible on the XRD slide to reduce texture effects. The scan time needs to be long enough to get a sufficiently high intensity:noise ratio and one should scan a large enough angle range to fit as many peaks as possible.

2.4.1.1 Sc_2C and Sc_2CH_2

Powdered samples of Sc_2C and Sc_2CH_2 were characterized by PXRD at room temperature in a Bragg-Brentano geometry across a range of 30−130° (Sc_2C) and 30-90° (Sc_2CH_2) using Cu Kα (λ= 1.54056 Å) in a Rigaku Smartlab diffractometer. The samples were covered with Kapton tape to keep them air-free. The pattern was indexed and refined using the PDXL software from Rigaku.

2.4.2 X-ray photoelectron spectroscopy

X-ray photoelectron spectroscopy (XPS) is an analytical technique for analyzing a material's surface composition quantitatively. In this technique, x-rays with a known wavelength (E_{photon}) are directed at the sample and the kinetic energies of the emitted electrons ($E_{kinetic}$) are measured. The binding energy of each electron ($E_{binding}$) can be calculated using the photoelectric effect (Eqn. 2.23), where ϕ is an instrumental correction to account for the kinetic energy lost by the electron emission from bulk to the detector.

$$E_{binding} = E_{photon} - (E_{kinetic} + \phi) \qquad (2.23)$$

The XPS detection limit is dependent on the material[115,116], and the binding energy gives information about the electronic states of any atoms present on the surface. By comparing the binding energy found in the sample to those published in the literature, one can determine the oxidation state of any given atom.

2.4.2.1 Sc_2C

Thin films were characterized by XPS using a Kratos Axis Ultra Delay-Line Detector spectrometer with a monochromatic Al Kα source. For these measurements, the powder was pressed into indium substrates. High-resolution XPS data were collected at a pass energy of 20 eV, and a charge neutralizer was used for charge compensation. All data were corrected to the C 1s peak at 284.6 eV. All XPS lines except those from the s orbitals occur as doublets due to spin-orbit coupling. Doublets originating from 2p orbitals will consist of the $2p^{3/2}$ and the $2p^{1/2}$ peaks, and typically, the intensity ratios will be 2:1, and the FWHM of both peaks in the doublet will be the same. This results in a 2:1 area ratio of the $2p^{3/2}$ and the $2p^{1/2}$ peaks. In the case of the Sc 2p peaks, however, it has been reported that the Sc 2p peaks do not follow these rules. The Sc $2p^{1/2}$ peak is typically wider than the Sc $2p^{3/2}$ peak, and the peak splitting varies somewhat depending on the Sc species[117]. This data informed our peak fitting process.

After 11 days of oxidation, the Sc sample showed one doublet which we assume is from the fully oxidized species. This data was fit with two peaks (GL(30) function in Vision Processing software) that were not constrained in any way. Once the peak positions, widths, and heights were optimized, the relative peak positions, relative FWHM, and peak heights were fixed with respect to each other (Component A).

This constrained doublet was then applied to the data obtained at the initial time point. The data required an additional component, which we assume to be a carbide component, given the prominent carbide peak present in the C 1s spectra. An asymmetric doublet (AS(80,0.4) function in the Vision Processing software) was added, but the two peaks in the doublet were not constrained in any way. The asymmetry function was varied, and the AS(80,0.4) function provided the best fit, especially when considering the peak at ~398 eV which is better resolved. These peaks were then constrained so that their relative peak positions, FWHM, and heights were fixed to each other (Component B). With these two doublets (fully formed oxide and carbide), there was still unfit intensity in the data. A third doublet was added, which we assume is an intermediate species as the carbide transitions to the fully formed oxide. Again, peaks were added without constraint, allowed to vary, and once the best fit was obtained, they were fixed with respect to each other (Component C). Finally, there was a small peak at low binding energy (395 eV). It is unclear if this is Sc or possibly N since the binding energy of this peak is low for either element.

We fit this as a fourth doublet (Component D), although its low intensity did not significantly alter the quality of the peak fit. The relative peak positions and relative FWHM values for the Sc $2p^{3/2}$ and Sc $2p^{1/2}$ peaks were compared to literature data[117], and found to match reasonably well (Table 2-2, 2-3, 2-4). We observed that the carbide component had an asymmetric peak shape, and therefore we fit this component with an asymmetric function.

Table 2-2. Scandium XPS peak positions

	11 days (eV)	1 day (eV)	0 days (eV)	Literature (eV)
$2p^{1/2}$ A	406.1	406.0	405.9	406.2[(3)]
$2p^{3/2}$ A	401.6	401.5	401.4	401.7[(3)]
$2p^{1/2}$ B		402.5	402.4	401.8[(4)]
$2p^{3/2}$ B		397.8	398.0	398.5[(4)]
$2p^{1/2}$ C		403.6	403.9	
$2p^{3/2}$ C		399.5	399.4	
$2p^{1/2}$ D		400.5	400.1	
$2p^{3/2}$ D		396.0	395.6	

Table 2-3. Scandium XPS peak splitting

	11 days	1 day	0 days	Literature
A	4.48	4.48	4.48	4.45[(3)]
B		4.66	4.66	
C		4.03	4.48	
D		4.48	4.48	

Table 2-4. Scandium XPS FWHM $2p^{3/2}$:$2p^{1/2}$

	11 days	1 day	0 days	Literature
A	0.79	0.79	0.79	0.75[(3)]
B		0.94	0.94	
C		0.85	0.79	
D		0.79	0.79	

The four sets of doublets used to fit the as-made data were applied to the 1-day data. They did not fit perfectly by just allowing the constrained doublet heights, widths, and positions to vary, so one by one, the components in each doublet were allowed to vary, optimized, and then fixed with respect to each other. The resulting relative peak positions and relative FWHM values for the Sc $2p^{3/2}$ and Sc $2p^{1/2}$ peaks were compared to literature data[117], and found to match reasonably well, except for the intermediate phase (Component C). In this case, the peak separation for the Sc $2p^{3/2}$ and Sc $2p^{1/2}$ peak was 4.0 eV, when it is more commonly reported as 4.5 eV for scandium oxides. In addition, the relative peak areas, which should

be 2:1 were closer to 1.2:1. Attempts were made to constrain the peaks in this doublet to more reasonable values, but the peak fit was noticeably worse. The cause is unclear, but perhaps another intermediate species was also present. However, it was unclear from the data where this would be, or how this would improve the fit. Chi-squared values for the resulting fits were 3.5 (as-made), 3.7 (1 day), and 4.8 (11 day).

REFERENCES

(1) Kresse, G.; Furthmuller, J. Efficient Iterative Schemes for Ab Initio Total-Energy Calculations Using a Plane-Wave Basis Set. *Phys Rev B* **1996**, *54* (16), 11169–11186.

(2) Blöchl, P. E. Projector Augmented-Wave Method. *Phys Rev B* **1994**, *50* (24), 17953–17979.

(3) Perdew, J. P.; Burke, K.; Ernzerhof, M. Generalized Gradient Approximation Made Simple. *Phys Rev Lett* **1996**, *77* (18), 3865–3868.

(4) Perdew, J. P.; Ruzsinszky, A.; Csonka, G. I.; Vydrov, O. A.; Scuseria, G. E.; Constantin, L. A.; Zhou, X.; Burke, K. Restoring the Density-Gradient Expansion for Exchange in Solids and Surfaces. *Phys Rev Lett* **2008**, *100* (13), 1–4.

(5) Krukau, A. v.; Vydrov, O. A.; Izmaylov, A. F.; Scuseria, G. E. Influence of the Exchange Screening Parameter on the Performance of Screened Hybrid Functionals. *J Chem Phys* **2006**, *125* (22).

(6) Ong, S. P.; Richards, W. D.; Jain, A.; Hautier, G.; Kocher, M.; Cholia, S.; Gunter, D.; Chevrier, V. L.; Persson, K. A.; Ceder, G. Python Materials Genomics (Pymatgen): A Robust, Open-Source Python Library for Materials Analysis. *Comput Mater Sci* **2013**, *68*, 314–319.

(7) Moellmann, J.; Grimme, S. DFT-D3 Study of Some Molecular Crystals. *J Phys Chem C* **2014**, *118* (14), 7615–7621.

(8) Hirayama, M.; Matsuishi, S.; Hosono, H.; Murakami, S. Electrides as a New Platform of Topological Materials. *Phys Rev X* **2018**, *8* (3), 31067.

(9) Perdew, J. P.; Zunger, A. Self-Interaction Correction to Density-Functional Approximations for Many-Electron Systems. *Phys Rev B* **1981**, *23* (10), 5048.

(10) Zhou, L.; Körmann, F.; Holec, D.; Bartosik, M.; Grabowski, B.; Neugebauer, J.; Mayrhofer, P. H. Structural Stability and Thermodynamics of CrN Magnetic Phases from *ab initio* Calculations and Experiment. *Phys Rev B Condens Matter Mater Phys* 2014, *90* (18), 184102.

(11) Wang, L.; Maxisch, T.; Ceder, G. Oxidation Energies of Transition Metal Oxides within the GGA+U Framework. *Phys Rev B Condens Matter Mater Phys* **2006**, *73* (19), 195107.

(12) Mosey, N. J.; Carter, E. A. Ab Initio Evaluation of Coulomb and Exchange Parameters for DFT+U Calculations. *Phys Rev B Condens Matter Mater Phys* **2007**, *76* (15), 155123.

(13) Mosey, N. J.; Liao, P.; Carter, E. A. Rotationally Invariant Ab Initio Evaluation of Coulomb and Exchange Parameters for DFT+U Calculations. *J Chem Phys* **2008**, *129* (1), 014103.

(14) Sai Gautam, G.; Carter, E. A. Evaluating Transition Metal Oxides within DFT-SCAN and SCAN+U Frameworks for Solar Thermochemical Applications. *Phys Rev Mater* **2018**, *2* (9), 095401.

(15) Long, O. Y.; Sai Gautam, G.; Carter, E. A. Evaluating Optimal U for 3d Transition-Metal Oxides within the SCAN+ U Framework. *Phys Rev Mater* **2020**, *4* (4), 045401.

(16) Perdew, J. P.; Levy, M. Physical Content of the Exact Kohn-Sham Orbital Energies: Band Gaps and Derivative Discontinuities. *Phys Rev Lett* **1983**, *51* (20), 1884.

(17) Kohn, W.; Sham, L. J. Self-Consistent Equations Including Exchange and Correlation Effects. *Phys Rev* **1965**, *140* (4A), A1133.

(18) Lucero, M. J.; Henderson, T. M.; Scuseria, G. E. Improved Semiconductor Lattice Parameters and Band Gaps from a Middle-Range Screened Hybrid Exchange Functional. *J Phys Condens Matter* **2012**, *24* (14), 145504.

(19) Borlido, P.; Schmidt, J.; Huran, A. W.; Tran, F.; Marques, M. A. L.; Botti, S. Exchange-Correlation Functionals for Band Gaps of Solids: Benchmark, Reparametrization and Machine Learning. *npj Comput Mater* **2020**, *6* (1), 1–17.

(20) Jain, A.; Ong, S. P.; Hautier, G.; Chen, W.; Richards, W. D.; Dacek, S.; Cholia, S.; Gunter, D.; Skinner, D.; Ceder, G.; Persson, K. A. Commentary: The Materials Project: A Materials Genome Approach to Accelerating Materials Innovation. *APL Mater* **2013**, *1* (1), 011002.

(21) Wang, V.; Xu, N.; Liu, J. C.; Tang, G.; Geng, W.-T. VASPKIT: A User-Friendly Interface Facilitating High-Throughput Computing and Analysis Using VASP Code. *Comput Phys Commun* **2021**, *267*, 108033.

(22) Becke, A. D.; Edgecombe, K. E. A Simple Measure of Electron Localization in Atomic and Molecular Systems. *J Chem Phys* **1998**, *92* (9), 5397.

(23) Savin, A.; Jepsen, O.; Flad, J.; Andersen, O. K.; Preuss, H.; von Schnering, H. G. Electron Localization in Solid-State Structures of the Elements: The Diamond Structure. *Angew Chem Int Ed* **1992**, *31* (2), 187.

(24) Savin, A.; Nesper, R.; Wengert, S.; Fassler, T. E. ELF: The Electron Localization Function. *Angew Chem Int Ed* **1997**, *36*, 1808–1832.

(25) Silvi, B.; Savin, A. Classification of Chemical Bonds Based on Topological Analysis of Electron Localization Functions. *Nature* **1994**, *371* (6499), 683–686.

(26) Momma, K.; Izumi, F. VESTA: A Three-Dimensional Visualization System for Electronic and Structural Analysis. *J Appl Crystallogr* **2008**, *41* (3), 653–658.

(27) Togo, A.; Tanaka, I. First Principles Phonon Calculations in Materials Science. *Scr Mater* **2015**, *108*, 1–5.

(28) Skelton, J. M.; Burton, L. A.; Jackson, A. J.; Oba, F.; Parker, S. C.; Walsh, A. Lattice Dynamics of the Tin Sulphides SnS2, SnS and Sn2S3: Vibrational Spectra and Thermal Transport. *Phys Chem Chem Phys* **2017**, *19* (19), 12452–12465.

(29) Pallikara, I.; Kayastha, P.; Skelton, J. M.; Whalley, L. D. The Physical Significance of Imaginary Phonon Modes in Crystals. *Electron Struc* **2022**, *4*, 033002.

(30) Malyi, O. I.; Sopiha, K. v.; Persson, C. Energy, Phonon, and Dynamic Stability Criteria of Two-Dimensional Materials. *ACS Appl Mater Interfaces* **2019**, *11* (28), 24876–24884.

(31) Kresse, G.; Furthmuller, J.; Hafner, J. Ab Intitio Force Constant Approach to Phonon Dispersion Relations of Diamond and Graphite. *Europhys Lett* **1995**, *32* (9), 729–734.

(32) Parlinski, K.; Li, Z. Q.; Kawazoe, Y. First-Principles Determination of the Soft Mode in Cubic ZrO_2. *Phys Rev Lett* **1997**, *78* (21), 4063.

(33) Giannozzi, P.; de Gironcoli, S.; Pavone, P.; Baroni, S. Ab Initio Calculation of Phonon Dispersions in Semiconductors. *Phys Rev B* **1991**, *43* (9), 7231–7242.

(34) Gonze, X.; Lee, C. Dynamical Matrices, Born Effective Charges, Dielectric Permittivity Tensors, and Interatomic Force Constants from Density-Functional Perturbation Theory. *Phys Rev B Condens Matter Mater Phys* **1997**, *55* (16), 10355–10368.

(35) Choudhary, K.; Garrity, K. F.; Sharma, V.; Biacchi, A. J.; Hight Walker, A. R.; Tavazza, F. High-Throughput Density Functional Perturbation Theory and Machine Learning Predictions of Infrared, Piezoelectric, and Dielectric Responses. *npj Comput Mater* **2020**, *6* (1), 1–13.

(36) Iftimie, R.; Minary, P.; Tuckerman, M. E. Ab Initio Molecular Dynamics: Concepts, Recent Developments, and Future Trends. *Proc Natl Acad Sci U S A* **2005**, *102* (19), 6654–6659.

(37) Ganose, A. M.; Park, J.; Faghaninia, A.; Woods-Robinson, R.; Persson, K. A.; Jain, A. Efficient Calculation of Carrier Scattering Rates from First Principles. *Nat Commun* **2021**, *12* (1), 1-9.

(38) Roh Lich, H. F. Theory of Electrical Breakdown in Ionic Crystals. *Proc R Soc Lond A Math Phys Sci* **1937**, *160* (901), 230–241.

(39) Hartig, M.; Haacke, S.; Deveaud, B.; Rota, L. Femtosecond Luminescence Measurements of the Intersubband Scattering Rate in $Al_xGa_{1-x}As$/GaAs Quantum Wells under Selective Excitation. *Phys Rev B* **1996**, *54* (20), R14269.

(40) Lang, N. D.; Kohn, W. Theory of Metal Surfaces: Work Function. *Phys Rev B* **1971**, *3* (4), 1215.

(41) Fall, C. J.; Binggeli, N.; Baldereschi, A. Deriving Accurate Work Functions from Thin-Slab Calculations. *J Phys Condens Matter* **1999**, *11* (13), 2689–2696.

(42) Lavakumar, A. Mechanical Properties of Materials. *Concepts in Physical Metallurgy Concise lecture notes*, **2017**.

(43) Hill, R. Elastic Properties of Reinforced Solids: Some Theoretical Principles. *J Mech Phys Solids* **1963**, *11* (5), 357–372.

(44) Hill, R. The Elastic Behaviour of a Crystalline Aggregate. *Proc Phys Soc* **1952**, *65* (5), 349.

(45) Voigt, W. Lehrbuch Der Kristallphysik; BG Teubner Verlag, **1928**.

(46) Reuss, A. Berechnung Der Fließgrenze von Mischkristallen Auf Grund Der Plastizitätsbedingung Für Einkristalle. *ZAMM* **1929**, *9* (1), 49–58.

(47) Jonsson, H.; Mills, G.; Jacobsen, K. W. Nudged Elastic Band Method for Finding Minimum Energy Paths of Transitions. *In Classical and Quantum Dynamics in Condensed Phase Simulations,* **1998**, 385–404.

(48) Wigner, E. The Transition State Method. *Transactions of the Faraday Society* **1938**, *34* (0), 29–41.

(49) Eyring, H. The Activated Complex in Chemical Reactions. *J Chem Phys* **1935**, *3* (2), 63–71.

(50) Keck, J. C. Variational Theory of Reaction Rates. In Advances in Chemical Physics; Prigogine, I., Ed.; *John Wiley & Sons, Ltd,* **1967**, *13*, 85–121.

(51) Voter, A. F.; Doll, J. D. Dynamical Corrections to Transition State Theory for Multistate Systems: Surface Self-diffusion in the Rare-event Regime. *J Chem Phys* **1998**, *82* (1), 80.

(52) Smidstrup, S.; Pedersen, A.; Stokbro, K.; Jónsson, H. Improved Initial Guess for Minimum Energy Path Calculations. *J Chem Phys* **2014**, *140* (21), 214106.

(53) Henkelman, G.; Uberuaga, B. P.; Jónsson, H. A Climbing Image Nudged Elastic Band Method for Finding Saddle Points and Minimum Energy Paths. *J Chem Phys* **2000**, *113* (22), 9901.

(54) Clark, S. J.; Segall, M. D.; Pickard, C. J.; Hasnip, P. J.; Probert, M. I. J.; Refson, K.; Payne, M. C. First Principles Methods Using CASTEP. *Z Krist* **2005**, *220* (5–6), 567–570.

(55) Vanderbilt, D. Soft Self-Consistent Pseudopotentials in a Generalized Eigenvalue Formalism. *Phys Rev B* **1990**, *41* (11), 7892.

(56) Tkatchenko, A.; Scheffler, M. Accurate Molecular van Der Waals Interactions from Ground-State Electron Density and Free-Atom Reference Data. *Phys Rev Lett* **2009**, *102* (7), 073005.

(57) Monkhorst, H. J.; Pack, J. D. Special Points for Brillouin-Zone Integrations. *Phys Rev B* **1976**, *13* (12), 5188.

(58) Govind, N.; Petersen, M.; Fitzgerald, G.; King-Smith, D.; Andzelm, J. A Generalized Synchronous Transit Method for Transition State Location. *Comput Mater Sci* **2003**, *28* (2), 250–258.

(59) Ciccotti, G.; Berne, B.; Coker, D. Classical and Quantum Dynamics in Condensed Phase Simulations; **1998**.

(60) Kresse, G.; Hafner, J. Ab Initio Molecular Dynamics for Liquid Metals. *Phys Rev B* **1993**, *47* (1), 558.

(61) Kresse, G.; Joubert, D. From Ultrasoft Pseudopotentials to the Projector Augmented-Wave Method. *Phys Rev B* **1999**, *59* (3), 1758.

(62) Zhang, X.; Xiao, Z.; Lei, H.; Toda, Y.; Matsuishi, S.; Kamiya, T.; Ueda, S.; Hosono, H. Two-Dimensional Transition-Metal Electride Y_2C. *Chem Mater* **2014**, *26* (22), 6638–6643.

(63) Druffel, D. L.; Lanetti, M. G.; Sundberg, J. D.; Pawlik, J. T.; Stark, M. S.; Donley, C. L.; McRae, L. M.; Scott, K. M.; Warren, S. C. Synthesis and Electronic Structure of a Crystalline Stack of MXene Sheets. *Chem Mater* **2019**, *31* (23), 9788–9796.

(64) Glass, C. W.; Oganov, A. R.; Hansen, N. USPEX-Evolutionary Crystal Structure Prediction. *Comput Phys Commun* **2006**, *175* (11–12), 713–720.

(65) van de Walle, A. A Complete Representation of Structure-Property Relationships in Crystals. *Nat Mater* **2008**, *7* (6), 455–458.

(66) Asta, M.; Ozolins, V.; Woodward, C. A First-Principles Approach to Modeling Alloy Phase Equilibria. *JOM* **2001**, *53* (9), 16–19.

(67) Zunger, A. First-Principles Statistical Mechanics of Semiconductor Alloys and Intermetallic Compounds. **1994**, 361–419.

(68) Sanchez, J. M.; Ducastelle, F.; Gratias, D. Generalized Cluster Description of Multicomponent Systems. *Phys A: Stat Mech App* **1984**, *128* (1–2), 334–350.

(69) Zhang, X.; Sluiter, M. H. F. Cluster Expansions for Thermodynamics and Kinetics of Multicomponent Alloys. *J Phase Equilibria Diffus* **2016**, *37* (1), 44–52.

(70) Fontaine, D. de. Cluster Approach to Order-Disorder Transformations in Alloys. *Solid State Phys* **1994**, *47* (C), 33–176.

(71) Ising, E. Beitrag Zur Theorie Des Ferromagnetismus. *Zeitschrift für Physik* **1925**, *31* (1), 253–258.

(72) Ceder, G. A Derivation of the Ising Model for the Computation of Phase Diagrams. *Comput Mater Sci* **1993**, *1* (2), 144–150.

(73) Zarkevich, N. A.; Johnson, D. D. Reliable First-Principles Alloy Thermodynamics via Truncated Cluster Expansions. *Phys Rev Lett* **2004**, *92* (25), 255702.

(74) Blum, V.; Zunger, A. Prediction of Ordered Structures in the Bcc Binary Systems of Mo, Nb, Ta, and W from First-Principles Search of Approximately 3,000,000 Possible Configurations. *Phys Rev B Condens Matter Mater Phys* **2005**, *72* (2), 020104.

(75) Hart, G. L. W.; Blum, V.; Walorski, M. J.; Zunger, A. Evolutionary Approach for Determining First-Principles Hamiltonians. *Nat Mater* **2005**, *4* (5), 391–394.

(76) Díaz-Ortiz, A.; Dosch, H.; Drautz, R. Cluster Expansions in Multicomponent Systems: Precise Expansions from Noisy. *J Physics Condens Matter* **2007**, *19* (40), 406206.

(77) Hyun Chang, J.; Kleiven, D.; Melander, M.; -, al; Barton, J.; Cocco -, S.; Lerch, D.; Wieckhorst, O.; W Hart, G. L.; Forcade, R. W.; Müller, S. UNCLE: A Code for Constructing Cluster Expansions for Arbitrary Lattices with Minimal User-Input. *Model Simul Mat Sci Eng* **2009**, *17* (5), 055003.

(78) Connolly, J. W. D.; Williams, A. R. Density-Functional Theory Applied to Phase Transformations in Transition-Metal Alloys. *Phys Rev B* **1983**, *27* (8), 5169.

(79) van de Walle, A.; Ceder, G. Automating First-Principles Phase Diagram Calculations. *J Phase Equilibria* **2002**, *23*, 348–359.

(80) Stone, M. Cross-Validatory Choice and Assessment of Statistical Predictions. *J R Stat Soc Series B Stat Methodol* **1974**, *36* (2), 111–147.

(81) Li, K.-C. Asymptotic Optimality for Cp, CL, Cross-Validation and Generalized Cross-Validation: Discrete Index Set. **1987**, *15* (3), 958–975.

(82) Stauffer, D. Monte Carlo Simulations in Statistical Physics. *Computer Simulation and Computer Algebra* **1988**, 55–81.

(83) Kikuchi, R. A Theory of Cooperative Phenomena. *Phys Rev* **1951**, *81* (6), 988.

(84) Ducastelle, F. Order and Phase Stability in Alloys. **1993**, 133–142.

(85) Kohan, A. F.; Tepesch, P. D.; Ceder, G.; Wolverton, C. Computation of Alloy Phase Diagrams at Low Temperatures. *Comput Mater Sci* **1998**, *9* (3–4), 389–396.

(86) Garbulsky, G. D.; Ceder, G. Linear-Programming Method for Obtaining Effective Cluster Interactions in Alloys from Total-Energy Calculations: Application to the Fcc Pd-V System. *Phys Rev B* **1995**, *51* (1), 67–72.

(87) Sanchez, J. M.; Ducastelle, F.; Gratias, D. Generalized Cluster Description of Multicomponent Systems. *Physica* **1984**, 334–350.

(88) Chang, J. H.; Kleiven, D.; Melander, M.; Akola, J.; Garcia-Lastra, J. M.; Vegge, T. CLEASE: A Versatile and User-Friendly Implementation of Cluster Expansion Method. *J Phys Condens Matter* **2019**, *31* (32), 325901.

(89) Nelson, L. J.; Hart, G. L. W.; Zhou, F.; Ozoliņš, V. Compressive Sensing as a Paradigm for Building Physics Models. *Phys Rev B Condens Matter Mater Phys* **2013**, *87* (3), 035125.

(90) Sundberg, J. D.; Benjamin, S. S.; McRae, L. M.; Warren, S. C. Simmate: A Framework for Materials Science. *J Open Source Softw* **2022**, *7* (75), 4364.

(91) C Ashby, B. E.; Brendel, O. J.; Redman, E. Direct Synthesis of Complex Metal Hydrides. *Inorg Chem* **1963**, *2* (3), 499–504.

(92) Kochaev, A.; Maslov, M.; Katin, K.; Efimov, V.; Efimova, I. Stabilization of Porous Borophene-Graphene Vertical Heterostructure Using Unilateral Hydrogenation. *Mater Today Nano* **2022**, 20.

(93) Liu, G.; Zhou, W.; Ji, Y.; Chen, B.; Fu, G.; Yun, Q.; Chen, S.; Lin, Y.; Yin, P. F.; Cui, X.; Liu, J.; Meng, F.; Zhang, Q.; Song, L.; Gu, L.; Zhang, H. Hydrogen-Intercalation-Induced Lattice Expansion of Pd@Pt Core-Shell Nanoparticles for Highly Efficient Electrocatalytic Alcohol Oxidation. *J Am Chem Soc* **2021**, *143* (29), 11262–11270.

(94) Ismail, N.; El-Meligi, A. A.; Temerk, Y. M.; Madian, M. Synthesis and Characterization of Layered $FePS_3$ for Hydrogen Uptake. *Int J Hydrogen Energy* **2010**, *35* (15), 7827–7834.

(95) Su, W.; Zhao, F.; Ma, L.; Tang, R.; Dong, Y.; Kong, G.; Zhang, Y.; Niu, S.; Tang, G.; Wang, Y.; Pang, A.; Li, W.; Wei, L. Synthesis and Stability of Hydrogen Storage Material Aluminum Hydride. *Materials*, **2021**, *14* (11), 2898.

(96) Aoki, K.; Masumoto, T. Solid State Amorphization of Intermetallic Compounds by Hydrogenation. *J Alloys Compd* **1993**, *194*, 251–261.

(97) Chase, M. W. NIST-JANAF Thermochemical Tables; **1998**; Vol. 4.

(98) Zhou, J.; Wang, H. The Physical Meanings of 5 Basic Parameters for an X-Ray Diffraction Peak and Their Application. *Chin J Geochem* **2003**, *22* (1), 38–44.

(99) March, A. Z. Mathematische Theorie Der Regelung Nach Der Korngestah Bei Affiner Deformation. *Kristallographie* **1932**, *81*, 285–297.

(100) Dollase, W. A. Correction of Intensities for Preferred Orientation in Powder Diffractometry: Application of the March Model. *J Appl Crystallogr* **1986**, *19* (4), 267–272.

(101) Schoening, F. R. L. Strain and Particle Size Values from X-Ray Line Breadths. *Acta Crystallogr* **1965**, *18* (5), 975–976.

(102) Nandi, R. K.; sen Gupta, S. P. The Analysis of X-Ray Diffraction Profiles from Imperfect Solids by an Application of Convolution Relations. *J Appl Crystallogr* **1978**, *11* (1), 6–9.

(103) Hindeleh, A. M.; Johnson, D. J. Crystallinity and Crystallite Size Measurement in Polyamide and Polyester Fibres. *Polymer* **1978**, *19* (1), 27–32.

(104) Jones, R. C. X-Ray Diffraction Line Profile Analysis Vs. Phosphorus Sorption by 11 Puerto Rican Soils. *Soil Sci Soc Am J* **1981**, *45* (4), 818–825.

(105) de Keijser, T. H.; Langford, J. I.; Mittemeijer, E. J.; Vogels, A. B. P. Use of the Voigt Function in a Single-Line Method for the Analysis of X-Ray Diffraction Line Broadening. *J Appl Crystallogr* **1982**, *15* (3), 308–314.

(106) Balzar, D.; Ledbetter, H. Voigt-Function Modeling in Fourier Analysis of Size- and Strain-Broadened X-Ray Diffraction Peaks. *J Appl Crystallogr* **1993**, *26* (1), 97–103.

(107) Wang, H.; Frey, M.; Stern, W. B. Diagenesis and Metamorphism of Clay Minerals in the Helvetic Alps of Eastern Switzerland. *Clay Clay Miner* **1996**, *44* (1), 96–112.

(108) Ida, T.; Ando, M.; Toraya, H. Extended Pseudo-Voigt Function for Approximating the Voigt Profile. *J Appl Crystallogr* **2000**, *33* (6), 1311–1316.

(109) Masson, O.; Guinebretiere, R.; Dauger, A. Modelling of Line Profile Asymmetry Caused by Axial Divergence in Powder Diffraction. *J Appl Crystallogr* **2001**, *34* (4), 436–441.

(110) Bragg, R. H.; Aladekomo, J. B. Diffraction by Diffusely Scattering Materials of High Transparency. *J Appl Crystallogr* **1995**, *28* (1), 14–19.

(111) Klug, H. P.; Alexander, L. E. X-Ray Diffraction Procedures: For Polycrystalline and Amorphous Materials, 2nd Edition, 2nd ed.; *John Wiley & Sons*, **1974**.

(112) Balzar, D.; Audebrand, N.; Daymond, M. R.; Fitch, A.; Hewat, A.; Langford, J. I.; le Bail, A.; Louër, D.; Masson, O.; McCowan, C. N.; Popa, N. C.; Stephens, P. W.; Toby, B. H. Size-Strain Line-Broadening Analysis of the Ceria Round-Robin Sample. *J Appl Crystallogr* **2004**, *37* (6), 911–924.

(113) Rietveld, H. M. The Rietveld Method. *Phys Scr* **2014**, *89* (9).

(114) Shard, A. G. Detection Limits in XPS for More than 6000 Binary Systems Using Al and Mg Kα X-Rays. *Surf Interface Anal* **2014**, *46* (3), 175–185.

(115) Faradzhev, N. S.; Hill, S. B.; Powell, C. J. Quantitative Analysis of Trace Levels of Surface Contamination by X-Ray Photoelectron Spectroscopy. Part II: Systematic Uncertainties and Absolute Quantification. Surface and Interface Analysis **2017**, *49* (12), 1214–1224.

(116) Biesinger, M. C.; Lau, L. W. M.; Gerson, A. R.; Smart, R. S. C. Resolving Surface Chemical States in XPS Analysis of First Row Transition Metals, Oxides and Hydroxides: Sc, Ti, V, Cu and Zn. *Appl Surf Sci* **2010**, *257* (3), 887–898.

(117) Merrick, J. Bonding in Scandium Monosulfide a NaCl Crystal Type, *Iowa State University*, **1980**.

CHAPTER 3: 2D ELECTRIDES AS FLUORIDE INTERCALATION ELECTRODES[a]

3.1 Introduction

Rechargeable batteries are necessary for diverse applications from microscopic devices to grid-scale energy storage. Myriad rechargeable battery technologies such as lead-acid, Ni-Cd, Ni-MH, and LIBs have been commercialized[1,2]. For the last two decades, intercalation-type LIBs have dominated the market because these LIBs offer high volumetric and gravimetric capacities and function reliably over hundreds or thousands of cycles. Now, a scarcity of lithium as well as plateauing improvements in the performance metrics of intercalation-type LIBs motivate the search for alternative technologies[3]. One promising alternative is intercalation-type anion batteries, particularly fluoride-ion batteries (FIBs).

Anions like fluoride (F^-) and chloride (Cl^-) are earth-abundant monovalent anions with lightweight, high charge density, and a large electrochemical stability window. These properties make these anions attractive as charge-transporting ions in a battery. Anion batteries have received little attention, however, due to a lack of suitable electrodes, particularly anodes.

While conversion-based anodes have been studied, the large volume changes that occur upon phase transformations require large overpotentials and dramatically limit the cycling stability[4]. Intercalation-type anodes are known to offer far superior cyclability, however, to date, studies on intercalation-type anode materials are very limited[5]. Only two materials have been investigated as intercalation-type anodes, $SrTiO_3F_2$[(6)] and $Sr_3Ti_2O_5F_4$[(7)] and unfortunately, we acknowledge that attempts to electrochemically drive fluorination and defluorination in these compounds were unsuccessful[5]. These materials failed because they did not have the key materials properties necessary for a feasible intercalation electrode.

[a] Portions of this chapter reproduced with permission from Druffel, D. L.; Pawlik, J. T.; Sundberg, J. D.; McRae, L. M.; Lanetti, M. G.; Warren, S. C. First-Principles Prediction of Electrochemical Electron-Anion Exchange: Ion Insertion without Redox. *The Journal of Physical Chemistry Letters* **2020**, 11 (21), 9210-9214. Copyright 2020 American Chemical Society.

Intercalation involves the charge-transporting ion inserting/deinserting into a host material. In a well-performing electrode, intercalation/deintercalation results in a <10% expansion in the host's volume with minimal disruption of the bonding in the host structure. The lack of structural change limits mechanical degradation, which is one of the primary reasons that intercalation-type batteries offer superior cyclability. In addition, low activation energy for the charge-carrying ion to hop between sites in the electrode (ideally <500 meV) directly correlates to faster ion diffusion, which facilitates the fast charge and discharge rates typical for intercalation-type batteries. Thirdly, intercalation often employs an efficient atom economy (for example, in $LiCoO_2$, a ratio of 1:3 charge-carrying atoms:host atoms), which provides high maximum volumetric and gravimetric capacities.

An elementary concept of chemistry is that the gain or loss of electrons in a material must be accompanied by the reduction or oxidation of its atoms. Here, we describe an exception to this concept. Some crystalline solids, called electrides, contain lattice sites occupied by a bare electron[8,9]. These electrons are called "anionic electrons" because they have a charge and size similar to those of simple anions. The striking parallel between anionic electrons and anions was demonstrated when electrides were reacted with metal halides, producing crystals in which the halide replaced the electride electron with minimal change to the crystal lattice[10]. Despite these findings, the reversible insertion or removal of anions is little explored, perhaps because anion movement typically involves high activation energies. In this section, however, we demonstrate using first-principles methods that anions and electrons can be exchanged at room temperature reversibly under electrochemical control (Figure 3-1a,b), where the electrode material gains and loses electrons without oxidation or reduction of its atoms. In addition, the 2D electron gas (2DEG) formed by the partially delocalized electrons facilitates the diffusion of ions because the ions hardly experience deflection in 2DEG. We suggest that this chemistry could enable a class of anode materials for intercalation-type batteries. Lastly, we identify the Y_2CF_2 as a potential anode material that offers superior properties over existing anodes for FIBs (Figure 3-1c). We show that Y_2CF_2 offers low migration barriers, high capacity, and a low reduction potential capable of achieving large cell voltages when paired with known F-intercalation cathodes. We believe these findings should motivate experimental studies of the electrochemical intercalation of Y_2CF_2.

In a general sense, exchanging an anion, such as fluoride, for an electride electron stabilizes the material system because the energetic electride electron shifts onto a lower-lying band comprised of fluorine p orbitals (Figure 3-1d). This provides a favorable driving force for a reaction with fluoride of a less electropositive metal (e.g., Cu) that could act as a cathode in a FIB. For example, the large free energy of the reaction $[Y_2C]^{2+}(e^-)_2 + CuF_2 \rightarrow Y_2CF_2 + Cu$ suggests a possible cell voltage of 2.8 V (see supporting information for chapter 3). To provide a fundamental grounding for EAX, we present computational results that address the oxidation states of the atoms, the mechanism of anion diffusion, and the structural changes that result.

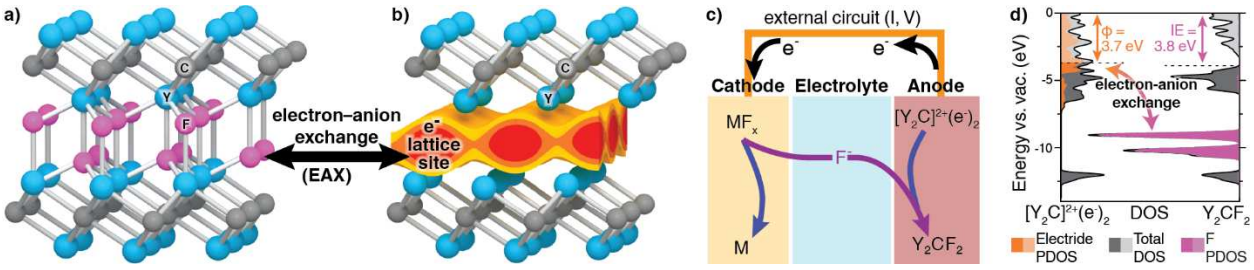


Figure 3-1. Concept of electron−anion exchange. The reversible conversion of (a) Y_2CF_2 to (b) $[Y_2C]^{2+}(e^-)_2$ under an applied bias where yellow, orange, and red show isosurfaces of the anionic electrons at the Fermi level. (c) Battery configuration incorporating $[Y_2C]^{2+}(e^-)_2$ as an anode, a F^- electrolyte, and a cathode (e.g., a metal fluoride). (d) Effect of electron−anion exchange on the partial density of states in the Y_2C system, where IE is the ionization energy and Φ is the work function.

3.2 Results and Discussion

We began by examining the electrides $[Ca_2N]^+e^-$ and $[Sr_2N]^+e^-$, which have positively charged layers of atoms that alternate with negatively charged layers of electrons. We found that fluoride intercalation and chloride intercalation were not reversible at room temperature because the corresponding halides are wide-band gap insulators with poor ionic mobility. We sought out an isostructural electride, $[Y_2C]^{2+}(e^-)_2$, because our calculations and experiments indicated that the corresponding fluoride, Y_2CF_2, has a small band gap and high electronic mobility[11]. We expected F^- to intercalate reversibly into the $[Y_2C]^{2+}(e^-)_2$ lattice as the e^- moves into an external circuit according to the half-reaction in Eqn. 3.1.

$$Y_2C^{2+}(e^-)_2 + 2F^-_{(electrolyte)} \leftrightarrow Y_2C^{2+}(F^-)_2 + 2e^-_{(circuit)} \quad (3.1)$$

For EAX to occur at room temperature, the anionic electron and F^- need to diffuse rapidly through the crystal. To assess F^- movement in the Y_2C system, we modeled a supercell of Y_2CF_2 and removed a fluorine atom, naturally introducing an anionic electron in its place (Figure 2b). Using DFT and NEB, we calculated a remarkably low activation barrier for electron−fluoride exchange (and thus F^- diffusion) in Y_2CF_2 of only 196 meV (Figure 3-2a), which is even lower than the barrier for Li^+ diffusion in both $LiCoO_2$ (~300 meV[12]) and graphite (~260 meV[13]). Our calculations reveal that the lowest-energy pathway for F^- diffusion in Y_2CF_2 is hopping of F^- directly between tetrahedral sites (Figure 3-2b−d), a distance of only 2.44 Å. Because the entire two-dimensional (2D) network of sites can be accessed by hopping exclusively through tetrahedral sites, we expect that this is the dominant mechanism of F^- diffusion in the layered Y_2C system and that F^- diffusion is rapid at room temperature.

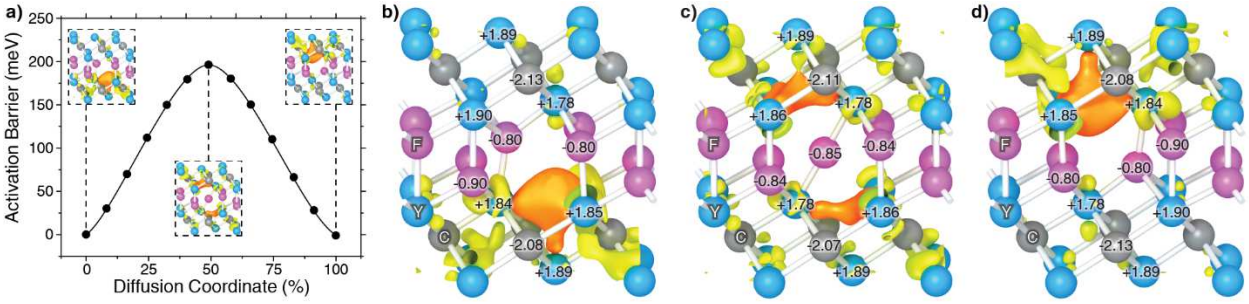


Figure 3-2. Mechanism of electron−anion exchange. (a) Activation barrier for the diffusion of F^- in Y_2CF_2 calculated using the NEB method. (b) Electron density isosurfaces near the Fermi level. The ground state of Y_2CF_2 with one F vacancy showing a F^- (purple) and an anionic electron (orange) at tetrahedral sites prior to exchange. The oxidation states are overlaid on the individual atoms, including Y (blue) and carbon (gray). (c) Transition state during electron−anion exchange. (d) Ground state after the exchange. All e^- densities are plotted at a value of 0.0036 $e^-/Å^3$.

To understand the extent of redox chemistry in electrochemical electron-anion exchange, we calculated the oxidation states of the atoms in the host lattice (see supporting information for chapter 3). We find that the oxidation states of Y (+1.91) and C (-2.06) in Y_2CF_2 are nearly identical to those in $[Y_2C]^{2+}(e^-)_2$ (+1.95 and -2.10, respectively)[14] and also agree with our experimental XPS measurements on Y_2CF_2 that identify a 2+ oxidation stat for Y[11]. Thus, in contrast to traditional ion insertion chemistry, in which

the oxidation state of a transition metal changes, the net result of EAX is that the atoms in the host lattice are neither reduced nor oxidized.

Though we determined that EAX results in no reduction or oxidation overall, the fundamental question of whether the elemental step of anion hopping involves transient redox processes in the host lattice remains. To answer this question, we calculated the electron density as the F^- hops along the NEB path, exchanging sites with an anionic electron (Figure 3-2b−d). We find that the position of the anionic electron differs subtly from the position of the F^- site (Figure 3-2b,d), but the electron density in that site still integrates to 0.8e− (Table 2-1). At the transition state, with F^- halfway between sites, the anionic electron simultaneously occupies both its initial site and its final site (Figure 3-2c). This behavior demonstrates an exciting result: while the anionic electron behaves in many ways like a traditional anion, it can still tunnel in a way common to electrons. We also note that even as the oxidation states remain unchanged (see Table 2-1), the valence electrons of nearby atoms polarize slightly (Figure 3-3). These plots show the change in electron density between the ground state and transition state with red (blue) showing areas that gain (lose) electron density. Individual atoms that surround the moving fluoride gain electron density on one side of the atom but lose electron density on the other, thus leading to a small polarization of the surrounding environment with negligible changes in oxidation state. In addition, bond lengths near the fluoride change by <0.03 Å, which further highlights how the electron transfer process that occurs in EAX is fundamentally different from ordinary redox processes, which can induce large changes in bond length.

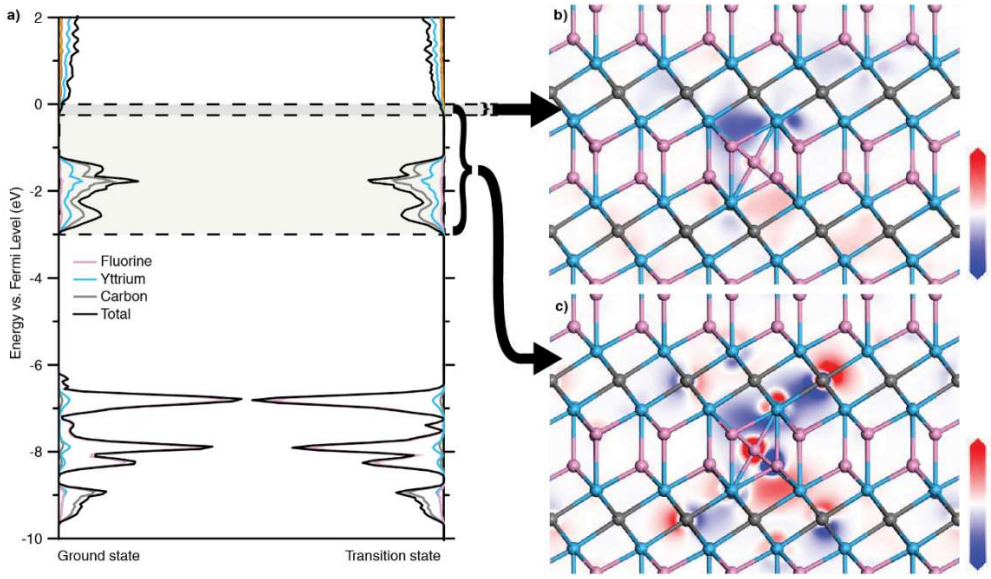


Figure 3-3. Polarization of valence electrons at and near the Fermi level. (a) Partial density of states for the ground and transition states during electron−anion exchange in Y_2CF_2. (b) Electron density deformation plots projected onto a 2D slice along the (110) direction cutting through the anionic electron and hopping F^-. These show the difference in electron density between the transition state and ground state for (b) the highest filled bands that comprise the anionic electron and (c) the valence bands comprised of the anionic electron, Y, C, and F orbitals, within 2.5 eV of the Fermi level. The scale bars for panels b and c are, from blue to red, 0.01 to 0.01 and −0.035 to 0.035 $e^-/Å^3$, respectively.

More broadly, the observations about EAX highlight similarities to the concept of proton-coupled electron transfer (PCET)[15] in which the movement of a proton is coupled to the movement of an electron. Here, our calculations show that anion movement occurs simultaneously with electron movement. We, therefore, introduce the term anion-coupled electron transfer (ACET) to describe the fundamental step of EAX. In the ACET observed in Figure 3-2, the transfer of an electron without reduction or oxidation of atoms indicates that the reorganization energy may be small or negligible.

Typically, intercalation is accompanied by significant volume expansion of the host lattice. For example, the insertion of lithium into graphite increases the number of atoms by 17% and leads to an expansion in the c lattice constant of 10%[(16)]. However, recently, we synthesized Y_2CF_2 and determined its crystal structure[11], which we find to be remarkably similar to that of $[Y_2C]^{2+}(e^-)_2$[(14,17)]. Complete fluorination (Y_2CF_2) increases the number of atoms in $[Y_2C]^{2+}(e^-)_2$ by 66% yet results in an expansion in the c lattice

constant by only 5.2% (Table 3-1). Moreover, in the Y_2C system, the a and b lattice constants and intralayer atomic distances all change by <1.1% (Table 3-1). We anticipate that the crystal structure may change its stacking sequence upon EAX, just as the stacking sequence changes in $LiCoO_2$ and graphite upon Li^+ intercalation (see Figure A3-1), but without disrupting local bonding. Importantly, EAX and a lack of redox chemistry facilitate the minimal changes in both volume and the local bonding of the host lattice.

Table 3-1. Atomic Distances in $[Y_2C]^{2+}(e^-)_2$[18] and Y_2CF_2[11] with Distances in Angstroms and Volumes (V) in Cubic Angstroms as Determined Experimentally.

	$Y_2C^{2+}(e^-)_2$	Y_2CF_2	Difference (%)
a	3.62483	3.6651	1.1
c	17.964	18.8907	5.2
Y-Y	2.493	2.510	0.7
Y-C	3.423	3.431	0.2
V	204.413	219.761	7.5

Finally, we discuss a natural application of this new mechanism, electrochemical energy storage. We calculated the potential at which electrons insert into Y_2CF_2 to be +0.97 V versus Li/Li^+ (Figure 3-4a), which suggests that $[Y_2C]^{2+}(e^-)_2/Y_2CF_2$ could serve as an anode in a F^- battery. The maximum gravimetric capacity of Y_2CF_2 is a remarkable 282 mAh/g (Figure 3-4b), comparable to that of $LiCoO_2$ (274 mAh/g)[19]. The high capacity is achieved despite using the heavy Y atoms because two F^- ions insert into each unit cell of $[Y_2C]^{2+}(e^-)_2$. Therefore, the gravimetric capacity can be improved by using lighter elements, for example, by alloying Y with Sc[20]. Upon replacement of Y with Sc entirely as in Sc_2CF_2, the density can reach 526 mAh/g, >70% more than that of $LiCoO_2$. Sc_2CF_2 also offers a high maximum volumetric capacity reaching 1634 mAh/cm^3 (Figure 3-4b). Calculations on the Sc_2CF_2 system reveal a small F^- diffusion barrier (~500 meV) and useful electron insertion potential (+1.1 V vs Li/Li^+), suggesting that electrochemical electron-anion exchange can enable champion anodes for F^- batteries.

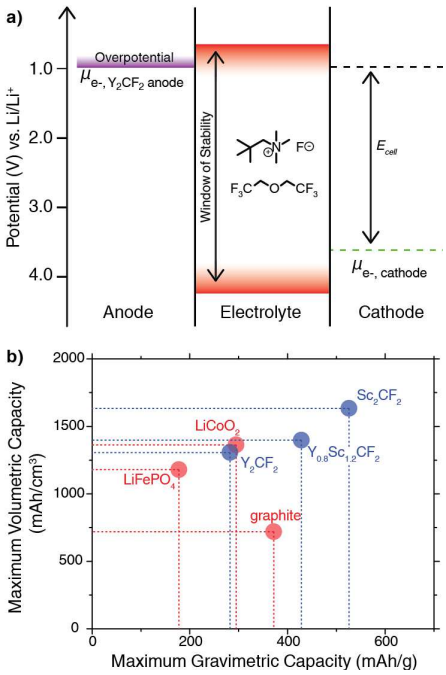


Figure 3-4. Application of electron−anion exchange. (a) Potential diagram of a F− battery utilizing a Y_2CF_2 anode, a NpF1/BTFE liquid electrolyte, and a cathode (e.g., CuF_2). (b) Comparison of capacities for common Li-ion intercalation electrodes to those of electrodes that use electron−anion exchange.

To understand the phase evolution in Y_2C/Y_2CF_2 and to calculate the voltage profile for intercalation, we performed cluster expansion and Monte Carlo simulations. Cluster expansion rigorously extracts the effective F-F and F-vacancy interactions from hundreds of DFT calculations. Subsequently, we employed those effective cluster interactions (ECI) in Monte Carlo simulations that result in our reported hull diagram and voltage profile. To use the cluster expansion method, we first identified a set of host phases that are likely to be stable. We considered three host phases, O3, T1, and H1-3, illustrated in Figure A3-2. We introduced the O3 as the Y_2C and the T1 as the Y_2CF_2 structures previously. The third, the H1-3 structure, is a hybrid of both O3 and T1. In the H1-3 structure, the unit cell consists of six layers of Y_2C in the R-3m space group alternating between O3 and T1 stacking sequences. The unit cell of H1-3 shares the same *a* lattice vector as O3, but the *c* lattice vector is double that of the O3 phase to account for the six layers. In all of the hosts, we assumed that the Y and C ions do not migrate. This is supported by DFT calculations suggesting that the activation barrier for C migration is more than 2 eV. Considering these three phases, we ran DFT calculations to calculate the ECIs and used the ECIs in Monte Carlo simulations

to construct the convex hull diagram shown in Figure 3-5a. The cluster expansion fit accurately reproduces the DFT calculation energies and convex hull (see supporting information for chapter 3).

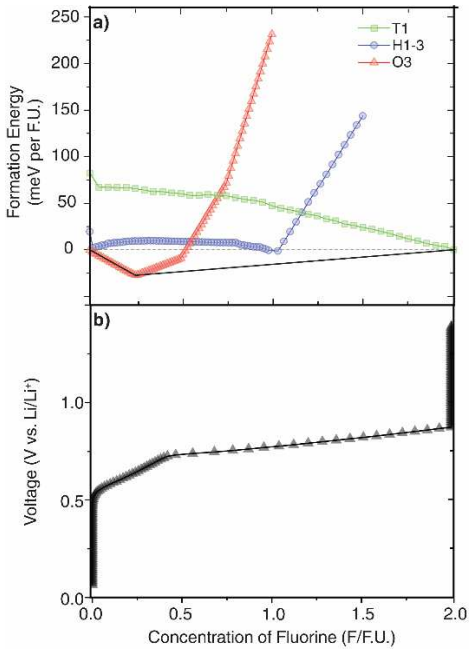


Figure 3-5. Convex hull and voltage profile from cluster expansion. a) The convex hull for fluorine intercalation in Y_2C considering the O3, T1, and H1-3 phases with the formation energies given in meV/formula unit. The energies are calculated by canonical Monte Carlo simulations at 0K using ECIs from cluster expansion fitting. b) The predicted voltage profile for fluorine intercalation in Y_2C. The voltage is derived from chemical potential calculated with semi-grand canonical Monte Carlo simulations at 298K.

Several important features about the phase stability are implied by the convex hull (solid black line in Figure 3-5a). First, in agreement with our earlier calculations, at a concentration of zero F, the O3 host is more stable than the T1 host; Y_2C adopts the O3 phase. Second, at complete fluorination, the T1 host is more stable than the O3 host; Y_2CF_2 adopts the T1 phase. These findings match the experimental observation that at high temperatures the syntheses of Y_2C and Y_2CF_2 yield the O3 and T1 phases respectively[11,14]. In addition, the convex hull reveals several stable ground states at low F concentrations. The convex hull is mainly shaped by the ground state at 0.25 F/F.U. with this O3 configuration exhibiting a formation energy of −25 meV/F.U. There are also ground states, all with the O3-stacking sequence, that lie below the linear interpolation between 0-0.25 F/F.U. (0-12.5%), affording a smoothly varying hull diagram

in this region. This suggests that in the low F regime, the ordered configurations of fluorine within the O3-stacking sequence of the Y_2C lattice effectively evolve continuously with intercalation of fluorine up to 0.25 F/F.U. With intercalation of fluorine beyond 0.25 F/F.U. ($12.5\% < x < 100\%$), we find a single two-phase region of coexisting O3-$Y_2CF_{0.25}$ and T1-Y_2CF_2. Interestingly, the H1-3 host lies above the convex hull at all concentrations of fluorine, meaning that it is less stable than the two-phase mixture.

We can also examine the metastable intermediates in addition to the ground state structures. Metastable intermediates are known to contribute to the kinetics of charge and discharge in experimental studies[21]. At all compositions from zero fluorination to complete fluorination, the formation energies for some metastable intermediates are low, even near kT at room temperature (Figure 3-5a). As an example, at 1 F/F.U. an H1-3 intermediate is only 22 meV/F.U. above the hull. This single-phase non-equilibrium path of fluorine intercalation through metastable intermediates involves topotactically related phases with minimal difference in lattice constants (value) and is kinetically accessible. This suggests that fluorine insertion through intermediate Y_2CF_x structures is possible with minimal input of energy or overpotential. Importantly, a single-phase transformation bypasses the extra kinetic barriers of nucleation and growth that are required for a two-phase transformation. This feature has important ramifications for battery performance and has been used to explain why $LiFePO_4$ functions as an electrode with high rate-capability[22].

Our discovery that fluorine intercalation in Y_2C has a kinetically accessible solid-solution path should facilitate the optimization of battery performance and experimentation. First, it suggests that particle size will play an important role in the charge/discharge process of Y_2C. Nanosizing particles tends to increase the solubility limits of the two phases whereas larger particles tend to facilitate phase separation[23]. Like nanosized $LiFePO_4$ or other two-phase ground-state intercalation systems, we expect smaller particles of Y_2C to exhibit faster kinetics and achieve better rate capabilities than large particles. Secondly, while fluorine intercalation may proceed through a single-phase transformation, the ground state consists of two phases. A partially charged electrode at rest will relax to the ground state and under ex-situ observation, the particles will appear only as ground-state structures. This has been observed in similarly behaving Li-ion electrodes[24]. Therefore, ex-situ TEM and XRD will reveal a mixture of O3-Y_2CF_x($0<x<0.25$) or fully

fluorinated T1-Y_2CF_2, but this should not be taken as evidence that the (de)intercalation involves a two-phase transformation.

With the convex hull, we obtain a piecewise voltage profile by evaluating the equilibrium voltage between the adjacent phases that make up the hull. The voltage profile shows a multitude of voltage steps, with the small steps (<0.05 V) originating from the numerous shallow ground states at low F concentrations. Voltage steps are associated with single-phase, ordered regions; however, we observe continuous ground-state orderings within the solution of our Monte Carlo simulations. Therefore, given the small size of the voltage steps and differences in an experimental setting to the considerations of our calculations like temperature and kinetic effects, we expect that in experiment the voltage profile will vary smoothly between 0 and 0.4 F/F.U. The dominant feature of the voltage curve, however, is the flat voltage plateau with fluorine intercalation beyond 0.4 F/F.U. accounting for 80% of the fluorination. This plateau owes to the two-phase mixture of O3-$Y_2CF_{0.25}$ and T1-Y_2CF_2. A similarly large voltage plateau is well known for the lithium electrode material $LiFePO_4$[25]. The second important feature of the voltage profile is the voltage itself. To yield a large cell voltage when paired with a cathode, ideally, an anode material has a low reduction potential similar to that of lithium. In Y_2C, fluorination begins at 0.54 V vs. Li/Li^+ and plateaus at 0.73V vs. Li/Li^+ resulting in an average voltage of 0.74 V vs. Li/Li^+. While not as extreme as that of Li or LiC_6, the reduction potential of Y_2C is still very low, making it an excellent candidate as an anode in a FIB.

We are exploring this electrochemistry experimentally in a half-cell configuration with electrodes made of Y2CF2 using N,N,N-trimethyl-N-neopentylammonium fluoride (NpF1) dissolved in blends of bis(2,2,2-trifluoroethyl)ether and tetraethylene glycol dimethyl ether[26]. Our experiments will be reported in a separate publication.

3.3 Conclusions

We have demonstrated a fundamentally distinct mechanism of electrochemically controlled ion insertion in which an electron reversibly inserts into a lattice without redox chemistry. Our calculations show that this occurs with minimal changes to the structure or oxidation states of the atoms. We suggest that electrochemical electron-anion exchange can address a deficiency in the science and technology of intercalation, the absence of high-capacity electrodes that reversibly intercalate anions at room

temperature. We expect that this mechanism will find use in other applications, as well, for example, in information processing, catalysis, and energy conversion.

Additionally, in the field of fluoride ion batteries, introducing Y_2C as a champion anode is a major step forward. Y_2C is promising by every metric. Its maximum capacity is the highest reported for any intercalation-type FIB electrode. Its reduction potential is low, just outside the electrochemical stability window of F-ion liquid electrolytes. Y_2C has a small activation barrier for F^- diffusion affording fast kinetics. Its combination of a very small change in volume upon intercalation coupled with its kinetically accessible solid-solution intercalation path may suggest that it will offer good cyclability. Together, this suggests that just as graphite is the champion anode for LIBs that Y_2C will be the champion anode for FIBs.

REFERENCES

(1) Fichtner, M.; Edström, K.; Ayerbe, E.; Berecibar, M.; Bhowmik, A.; Castelli, I. E.; Clark, S.; Dominko, R.; Erakca, M.; Franco, A. A.; Grimaud, A.; Horstmann, B.; Latz, A.; Lorrmann, H.; Meeus, M.; Narayan, R.; Pammer, F.; Ruhland, J.; Stein, H.; Vegge, T.; Weil, M. Rechargeable Batteries of the Future—The State of the Art from a Battery 2030+ Perspective. *Adv Energy Mater* **2022**, *12* (17), 2102904.

(2) Mizushima, K.; Jones, P. C.; Wiseman, P. J.; Goodenough, J. B. Li_xCoO_2 ($0<x\leq1$): A New Cathode Material for Batteries of High Energy Density. *Solid State Ion* **1981**, *3–4* (C), 171–174.

(3) Greim, P.; Solomon, A. A.; Breyer, C. Assessment of Lithium Criticality in the Global Energy Transition and Addressing Policy Gaps in Transportation. *Nature Comm* **2020**, *11* (1), 1–11.

(4) Nowroozi, M. A.; Clemens, O. Insights on the Behavior of Conversion-Based Anode Materials for Fluoride Ion Batteries by Testing against an Intercalation-Based Reference Cathode. *ACS Appl Energy Mater* **2018**, *1* (11), 6626–6637.

(5) Nowroozi, M. A.; Mohammad, I.; Molaiyan, P.; Wissel, K.; Munnangi, A. R.; Clemens, O. Fluoride Ion Batteries - Past, Present, and Future. *J Mater Chem A* **2021**, *9* (10), 5980–6012.

(6) Wissel, K.; Dasgupta, S.; Benes, A.; Schoch, R.; Bauer, M.; Witte, R.; Fortes, A. D.; Erdem, E.; Rohrer, J.; Clemens, O. Developing Intercalation Based Anode Materials for Fluoride-Ion Batteries: Topochemical Reduction of $Sr_2TiO_3F_2$ via a Hydride Based Defluorination Process. *J Mater Chem A* **2018**, *6* (44), 22013–22026.

(7) Wissel, K.; Vogel, T.; Dasgupta, S.; Fortes, A. D.; Slater, P. R.; Clemens, O. Topochemical Fluorination of n = 2 Ruddlesden-Popper Type $Sr_3Ti_2O_7$ to $Sr_3Ti_2O_5F_4$ and Its Reductive Defluorination. *Inorg Chem* **2020**, *59* (2), 1153–1163.

(8) Keve, E. T.; Skapski, A. C. Ca_2N: A Nitride with a Layer Structure. *Chem Commun* **1966**, *22* (22), 829–830.

(9) Matsuishi, S., Toda, Y., Miyakawa, M., Hayashi, K., Kamiya, T., Hirano, M., Tanaka, I., Hosono, H. High-Density Electron Anions in a Nanoporous Single Crystal:$[Ca_{24}Al_{28}O_{64}]^{4+}(4e^-)$. *Science* **2003**, *301*, 626–630.

(10) Bowman, A.; Mason, P. v.; Gregory, D. H. Heteroanionic Intercalation into Positively Charged Inorganic Hosts: The First Nitride Mixed Halides. *Chem Commun* **2001**, *1* (17), 1650–1651.

(11) Druffel, D. L.; Lanetti, M. G.; Sundberg, J. D.; Pawlik, J. T.; Stark, M. S.; Donley, C. L.; McRae, L. M.; Scott, K. M.; Warren, S. C. Synthesis and Electronic Structure of a Crystalline Stack of MXene Sheets. *Chem Mater* **2019**, *31* (23), 9788–9796.

(12) Okubo, M.; Tanaka, Y.; Zhou, H.; Kudo, T.; Honma, I. Determination of Activation Energy for Li Ion Diffusion in Electrodes. *J Phys Chem B* **2009**, *113* (9), 2840–2847.

(13) Toyoura, K.; Koyama, Y.; Kuwabara, A.; Oba, F.; Tanaka, I. First-Principles Approach to Chemical Diffusion of Lithium Atoms in a Graphite Intercalation Compound. *Phys Rev B Condens Matter Mater Phys* **2008**, *78* (21), 214303.

(14) Zhang, X.; Xiao, Z.; Lei, H.; Toda, Y.; Matsuishi, S.; Kamiya, T.; Ueda, S.; Hosono, H. Two-Dimensional Transition-Metal Electride Y_2C. *Chem Mater* **2014**, 26 (22), 6638–6643.

(15) Huynh, M. H. v.; Meyer, T. J. Proton-Coupled Electron Transfer. *Chem Rev* **2007**, *107* (11), 5004–5064.

(16) Schweidler, S.; de Biasi, L.; Schiele, A.; Hartmann, P.; Brezesinski, T.; Janek, J. Volume Changes of Graphite Anodes Revisited: A Combined Operando X-Ray Diffraction and in Situ Pressure Analysis Study. *J Phys Chem C* **2018**, *122* (16), 8829–8835.

(17) Atoji, M.; Kikuchi, M. Crystal Structures of Cubic and Trigonal Yttrium Hypocarbides; A Dimorphically Interphased Single-Crystal Study. *J Chem Phys* **1969**, *51* (9), 3863–3872.

(18) Maehlen, J. P.; Yartys, V. A.; Hauback, B. C. Structural Studies of Deuterides of Yttrium Carbide. *J Alloys Compd* **2003**, *351* (1–2), 151–157.

(19) Orman, H. J.; Wiseman, P. J. Cobalt(III) Lithium Oxide, $CoLiO_2$: Structure Refinement by Powder Neutron Diffraction. *Acta Crystallogr C* **1984**, *40* (1), 12–14.

(20) Park, J.; Hwang, J. Y.; Lee, K. H.; Kim, S. G.; Lee, K.; Kim, S. W. Tuning the Spin-Alignment of Interstitial Electrons in Two-Dimensional Y_2C Electride via Chemical Pressure. *J Am Chem Soc* **2017**, *139* (48), 17277–17280.

(21) Yoshinari, T.; Yamamoto, K.; Nishijima, M.; Fukuda, K.; Kuwabara, A.; Tanaka, I.; Maeda, K.; Kageyama, H.; Orikasa, Y.; Uchimoto, Y. High Rate Performance of Dual-Substituted $LiFePO_4$ Based on Controlling Metastable Intermediate Phase. *ACS Appl Energy Mater* **2018**, *1* (12), 6736–6740.

(22) Malik, R.; Zhou, F.; Ceder, G. Kinetics of Non-Equilibrium Lithium Incorporation in $LiFePO_4$. *Nat Mater* **2011**, *10* (8), 587–590.

(23) Wagemaker, M.; Mulder, F. M. Properties and Promises of Nanosized Insertion Materials for Li-Ion Batteries. *Acc Chem Res* **2013**, *46* (5), 1206–1215.

(24) Delmas, C.; Maccario, M.; Croguennec, L.; le Cras, F.; Weill, F. Lithium Deintercalation in LiFePO4 Nanoparticles via a Domino-Cascade Model. *Nat Mater* **2008**, *7* (8), 665–671.

(25) Rowden, B.; Garcia-Araez, N. Estimating Lithium-Ion Battery Behavior from Half-Cell Data. *Energy Rep* **2021**, *7*, 97–103.

(26) Davis, V. K.; Bates, C. M.; Omichi, K.; Savoie, B. M.; Momčilović, N.; Xu, Q.; Wolf, W. J.; Webb, M. A.; Billings, K. J.; Hawn Chou, N.; Alayoglu, S.; McKenney, R. K.; Darolles, I. M.; Nair, N. G.; Hightower, A.; Rosenberg, D.; Ahmed, M.; Brooks, C. J.; Miller III, T. F.; Grubbs, R. H.; Jones, S. C. Room-Temperature Cycling of Metal Fluoride Electrodes: Liquid Electrolytes for High-Energy Fluoride Ion Cells. *Science* **2018**, *362* (6419), 1144–1148.

CHAPTER 4: Sc_2C – A 2D SEMICONDUCTING ELECTRIDE[b]

Lauren M. McRae†, *Rebecca C. Radomsky*†, *Jacob T. Pawlik*†, *Daniel L. Druffel*†, *Jack D. Sundberg*†, *Matthew G. Lanetti*†, *Carrie L. Donley*‡, *Kelly L. White*†, and *Scott C. Warren**,†

†Department of Chemistry, University of North Carolina at Chapel Hill, Chapel Hill, North Carolina 27599, United States

‡Chapel Hill Analytical and Nanofabrication Laboratory (CHANL), University of North Carolina at Chapel Hill, Chapel Hill, North Carolina 27599, United States

4.1 Introduction

Challenges in energy storage, electronics, and catalysis motivate the search for exotic materials with extreme properties, and electrides—crystals with bare electrons trapped at stoichiometric concentrations[1-3]—offer some of the most exceptional. These electrons have been ejected from atomic orbitals to reside in vacant lattice sites and, because they are so weakly bound, are better electron donors than alkali metals[4-6], can offer electrical conductivity that rivals silver[6], and can catalyze challenging reactions[6]. These properties have led to the exploration of electrides in applications where electron-rich materials are needed: N_2 and CO_2 reduction[7,8], battery electrodes[9,10], and electron emitters[11-13]. Despite this progress, rules that might predict an electride's properties based on its structure or composition are underdeveloped. For example, unlike in conventional materials, it is not known how to tune the band gap of electrides. And, even more critically, simple rules that could predict whether a material is an electride remain imprecise[3,14].

Presently, just two rules for predicting electrides are widely accepted: (1) the metal atoms that form the coordination sphere around the electride electron must be electropositive[15], and (2) the compound must

[b] Portions of this chapter reproduced with permission from McRae, L. M.; Radomsky, R. C.; Pawlik, J. T.; Druffel, D. L.; Sundberg, J. D.; Lanetti, M. G.; Donley C. L.; White, K. L.; Warren, S. C. Sc_2C: a 2D Semiconducting Electride. *Journal of the American Chemical Society* **2022**, 144 (24), 10862-10869. Copyright 2022 American Chemical Society.

be electron rich[16]. For example, in $[Ca_2N]^+(e^-)$[(17)], calcium is electropositive, and the compound is electron rich because the preferred oxidation states (Ca^{2+}, N^{3-}) and stoichiometry provide an extra electron, forming an electride. These rules are far too broad, however, because many compounds fulfill these rules but are not electrides.

To improve these rules, experiments have begun to identify the metals that can be adjacent to an electride electron. So far, only Ca[(5)], Sr[(18,19)], Ba[(20)], Y[(21,22)], Hf[(23)], and Gd[(24,25)] have been incorporated next to the electride site (Figure 4-1), while Sc and several of the lanthanide series have been identified as candidates computationally[26-28]. This delicate balance between electron counting and electronegativity was recently explored in the case of Ca_5Pb_3 (not an electride) and $Ca_3Hf_2Pb_3$ (an electride), as replacing calcium for hafnium makes the compound electron rich[16]. Despite these findings, the limit of cation electronegativity in the formation of electrides is not yet known. Therefore, to develop improved design rules for electrides and for their structure-property relationships, we explore the trivalent metal carbides with a layered structure. This family is informative because Y_2C is a known electride[22], Sc_2C has been predicted[26], and Al_2C is unknown, and further, these metals vary systematically in electronegativity (Figure 4-1).

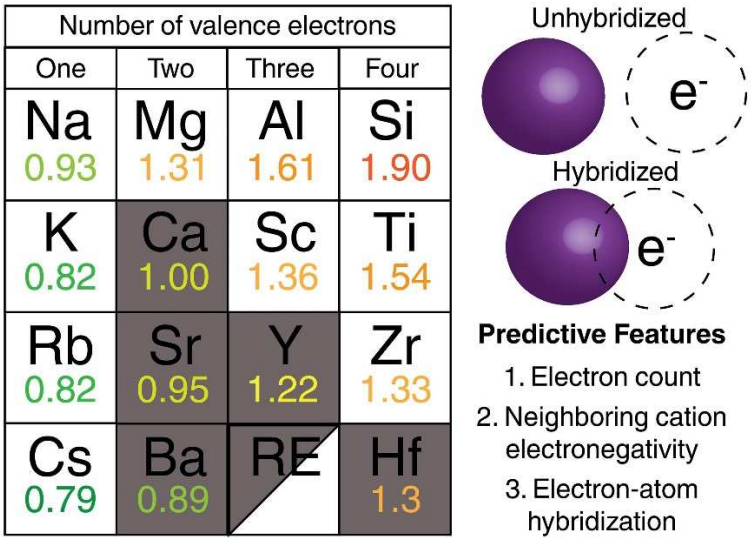


Figure 4-1. An adapted periodic table highlighting the valency of various cations. The Pauling electronegativity values are shown beneath each element symbol, and the gray blocks indicate which cations have been experimentally incorporated next to an electride site. The predictive features for potential electrides are listed and electride electron-atom hybridization is illustrated.

The question of electronegativity is essential because two experimentally observed electrides—Y_2C and Hf_2S—are "hybrid" electrides[3], where the electride electron has some overlap with the adjacent metal orbitals, and electronegativity of the metal may be correlated with the degree of hybridization. This covalency plays an important role in defining the electronic structure of the electride because the electride electron is normally found around the Fermi level. Thus, as hybridization occurs, tunable band structures become possible, and indeed, Y_2C is a semi-metal. While there are examples of 0D electrides[28-31] and electride-like structures[32] with semiconducting character, this is unique among the 2D electrides[3,33]. This peculiarity raises the question of whether greater degrees of hybridization between metal and electride electron could lead to new categories of electride materials[34]. These questions motivate our exploration of the M_2C system, especially of layered Sc_2C.

To highlight uncertainties within the Sc_2C system, we briefly outline previous findings and predictions. Sc_2C was originally synthesized in 1967 and assigned to the NaCl structure type, which we refer to below as the cubic phase[35]. In 1969, different authors reassigned the structure as layered (R-3m) on the basis of its powder x-ray diffraction (PXRD) pattern[21,36], even though the pattern was missing several important reflections (Table A4-1).

In 1989, the structure was again reassigned as the cubic phase[37] (Figure 4-2a, updated with our findings). This assignment appears to be correct and it is not known whether a layered Sc_2C electride exists. Currently, a 2D Sc_2C MXene structure has been explored computationally[38,39] and calculations predict that layered Sc_2C would be an electride[26]. In addition, 2D Sc_2C has been predicted to store an impressive 8% hydrogen by weight[40,41] and reversibly store fluoride as a battery anode at capacities that exceed state-of-the-art lithium-ion batteries[10]. Thus, if a layered Sc_2C electride does exist, it could allow these exciting predictions to be realized.

In this study, we predict that layered Sc_2C is stable using an evolutionary algorithm and experimentally explore the phase diagram around the desired composition. We then calculate the electronic structure of the synthesized material and compare it to Y_2C and Al_2C to understand periodic trends. We find that as the cation becomes more electronegative, the band gap opens with Y_2C as a semimetal, Sc_2C as a small band gap semiconductor, and Al_2C as a larger gap semiconductor. The synthesized layered

Sc_2C is the first 2D electride with semiconducting properties, opening up a fascinating new class of electride materials with several possible applications in energy storage or optoelectronics.

4.2 Results and Discussion

4.2.1 Phase diagram exploration

Although layered Sc_2C is unknown, we and Hirayama *et. al.*[26] have hypothesized that it exists because Sc is chemically similar to Y and layered Y_2C is a stable phase. To investigate whether layered Sc_2C is thermodynamically stable, we used USPEX to explore the scandium-carbon phase space. The phase diagram we obtained indicates that the Sc_2C composition is on the hull and that the layered R-3m structure is stable by 28 meV/atom (Figure 4-2b). This modest relative stability could suggest why the layered phase had not previously been synthesized.

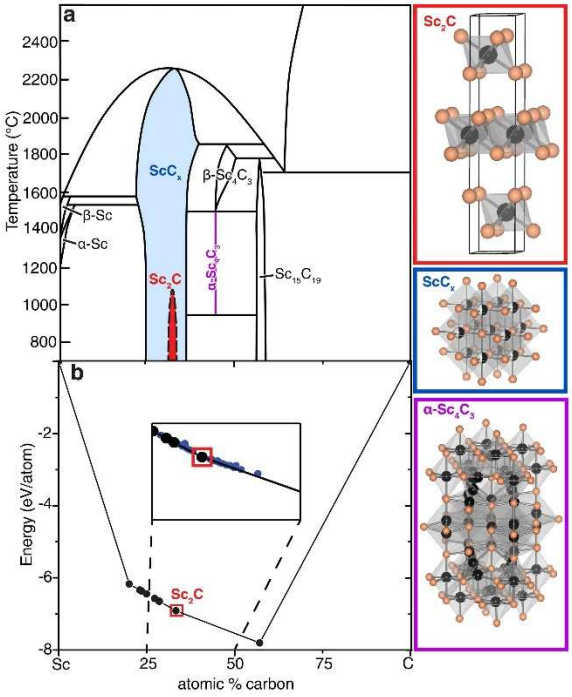


Figure 4-2. Phase diagram of the Sc-C system. (a) The binary phase diagram of the Sc-C system. The layered Sc_2C is shown in red. (b) The hull diagram for the Sc-C phase, as calculated with USPEX. The conventional unit cell for layered Sc_2C (red), cubic ScC_x (green), and α-Sc_4C_3 (purple) are shown.

The possibility that layered Sc_2C is thermodynamically stable motivated us to make this compound via high-temperature solid-state synthesis. In the Y_2C synthesis, we observed that high oxygen content in

the yttrium led to the formation of the cubic phase (YC_x). With this in mind, compared to the synthesis performed in Rassaerts *et. al.*'s 1967 study, we suspected that our use of high-purity scandium with a lower oxygen content would allow us to experimentally realize our computational prediction. We arc-melted scandium and carbon in ratios from 2:0.9 to 2:1.15, respectively. These arc-melted samples had a high content of the cubic structure (ScC_x) (Figure A4-2), but arc-melting has a rapid cool-down, so the structure may not be at equilibrium. Therefore, we followed arc-melting with annealing for 7 days at 1100°C to increase the likelihood of observing the thermodynamically favored layered phase. We found that the cubic structure is stable both at compositions with deficient carbon (Figure A4-3) and excess carbon (Figure A4-4). However, at a composition of 2:0.99, the layered structure was observed, and this is reflected in the new binary phase diagram we propose for the Sc-C system (Figure 4-2a)[37]. There is uncertainty in the assignment of the temperature at which the congruent layered-to-cubic phase change occurs, but our experiments indicate that the layered phase is stable to at least 1100°C.

To fully understand the structure of the layered phase, we first performed PXRD experiments of the product at room temperature and refined the pattern using the Rietveld method[42] (Figure 4-3). The pattern indexed as the R-3m structure with lattice parameters of $a = b = 3.337$ Å and $c = 16.346$ Å. This refinement includes the incorporation of preferred orientation at {104} with a March coefficient of 0.754. The sample contained up to 15% of the cubic ScC_x, which we attribute to the relatively low stability of the layered phase as well as possible oxygen contamination in the Sc reactant. To quantitatively compare the predicted and experimental structures, we further optimized the structure from USPEX using the PBEsol functional. The calculated lattice parameters were 0.68% smaller in a and 0.09% smaller in c, which is within the typical error between PBEsol and experiment. This further confirms that the synthesized material is layered Sc_2C.

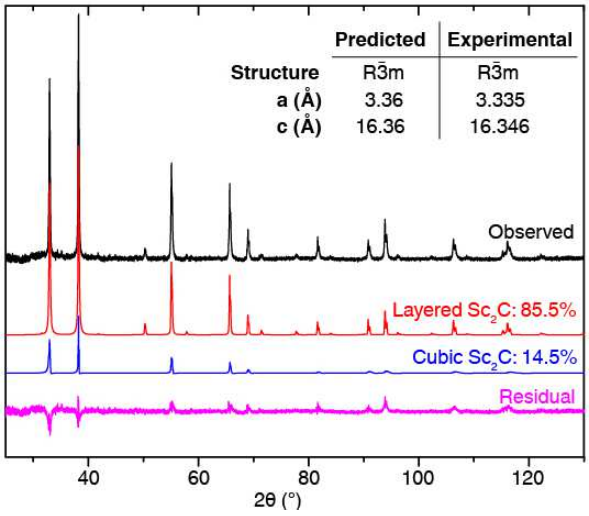
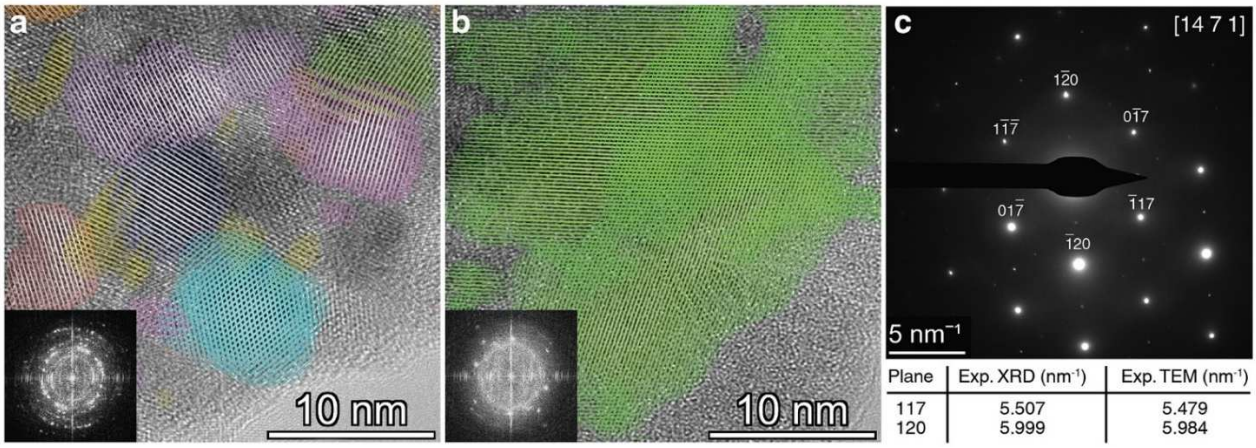


Figure 4-3. X-ray diffraction patterns of the experimental structure compared to the calculated layered and cubic Sc_2C phases. The calculated amounts of the layered and cubic are shown as determined by the Rietveld method. The predicted and experimental lattice parameters are compared.

To better understand the effect of annealing in these samples, we obtained high-resolution transmission electron microscopy (HRTEM) of the product at room temperature under high vacuum. In Figure 4-4, we compare the Fast Fourier Transform (FFT) of these samples, where the non-annealed sample shows a ring pattern while the annealed sample shows well-defined spots. From the FFT images, we constructed filtered HRTEM images to create a color-coded map of crystalline domains where we compare the crystallinity of Sc_2C before and after annealing. The filtered HRTEM images and FFTs confirm that the domain size is small before annealing, likely due to kinetic trapping from rapid cooling after arc-melting. Even with annealing, there was still about 15% of the cubic phase present, which we attribute to a small amount of oxygen in the sample. In an attempt to leach any oxygen present in the reaction container, we tried the synthesis in the presence of a titanium sponge. This did not improve the layered content of the sample. We, therefore, suspect that impurities in the product must come from impurities present in the Sc reactant. Specifically, Sc that is nominally 99.999% pure typically contains 0.1-0.5 at.% oxygen[43], thus favoring a small amount of the cubic phase.

In addition, we used TEM to confirm that the layered Sc_2C phase is dominant. While from XRD there is a small amount of cubic Sc_2C (14.5%) compared to layered Sc_2C (85.5%), the refinement has some

uncertainty because the layered and cubic patterns are similar. In electron diffraction, the most common spatial frequency corresponds to a d-spacing of 2.3 Å, which we assign to either {104} in the layered structure or {101} in the cubic structure. This ambiguity motivated us to find distinct peaks for the layered phase. To identify the phase of these domains, we sought to acquire diffraction patterns containing the {117} reflection of the layered phase, which is expected at 5.501 nm^{-1}, for which there are no reflections in the cubic phase. In Figure 4-4c, we observe diffraction spots at 5.479 nm^{-1}, which can only be assigned to the layered phase. Simulations of the cubic structure with varied arrangements of carbon and carbon vacancies also failed to show a diffraction peak at 5.501 nm^{-1}. Importantly, the prevalence of {117} in diffraction patterns increases upon annealing, in agreement with XRD. In addition, XRD and TEM lattice spacings agree within 0.6%. This data confirms the experimental structure from XRD and corroborates the Rietveld refinement result.



Plane	Exp. XRD (nm^{-1})	Exp. TEM (nm^{-1})
117	5.507	5.479
120	5.999	5.984

Figure 4-4. TEM images of Sc_2C. (a) A high-resolution TEM image of Sc_2C before annealing, with colored lattice planes corresponding to different crystallite regions determined through FFTs. (b) A high-resolution TEM image of Sc_2C after annealing for 7 days, with the lattice planes of the single crystallite region in green. (c) A selected area electron diffraction (SAED) pattern of the [14 7 1] zone axis. The corresponding experimental d-spacings are compared.

4.2.2 Assessment of electride character and electronic structure

Having confirmed the existence of layered Sc_2C as a thermodynamically stable material, we examined the material's electride character. In the experimental structure determined from our Rietveld refinement, there was a longer scandium-scandium distance (3.53 Å) than in scandium metal (3.22 Å) and

Sc_2O_3 (3.27 Å). This increased distance could indicate that electride electrons are present, so we sought evidence by calculating the electron localization function (ELF) using the hybrid DFT functional HSE-06. The ELF measures the degree of electron spatial localization compared to a reference electron with the same spin and provides a map of electron probability across a system. The ELF of Sc_2C shows localization of electrons that are not associated with either the scandium or carbon atoms and indicates that there is electride character in the layered structure (Figure 4-5a).

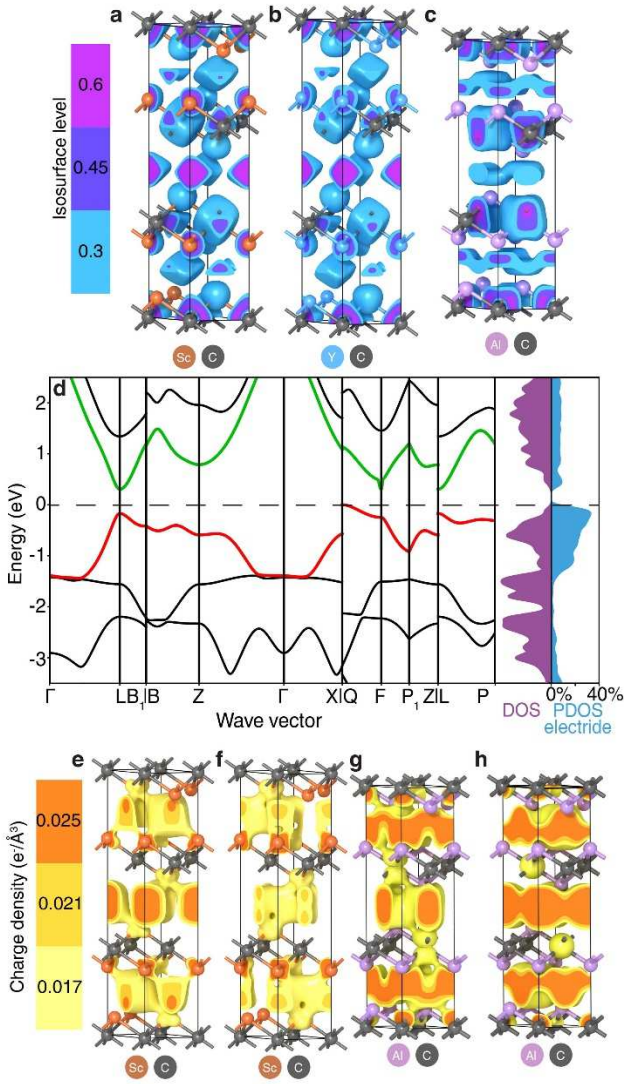


Figure 4-5. Electronic structure of Sc_2C compared to Al_2C and Y_2C. (a) The 3D ELF of Sc_2C, where the gradient of isosurface level spans from 0.3-0.6. This scale is the same for each ELF. (b) The 3D ELF of Y_2C. (c) The 3D ELF of Al_2C. (d) The Sc_2C band structure, total density of states (purple), and partial density

of the electride states as a percentage of the total (blue). The valence and conduction bands are highlighted in red and green, respectively. (e) The charge density of the Sc_2C valence band at the L point. The gradient of charge density spans from 0.017 $e^-/Å^3$ - 0.025 $e^-/Å^3$. This scale is the same for each charge density. (f) The charge density of the Sc_2C conduction band at the L point. (g) The charge density of the Al_2C valence band at the L point. (h) The charge density of the Al_2C conduction band at the L point.

We calculated the band structure and density of states (DOS) with HSE-06 and found that Sc_2C is a semi-conductor with a 0.305 eV indirect band gap and a 0.476 eV direct band gap (Figure 4-5d). We attempted to further purify Sc_2C, but the cubic phase remained in all experiments. This prevented us from making electrical and optical band gap measurements on pure layered Sc_2C.

4.2.3 Emergence of semiconducting behavior in electrides

To understand how cation electronegativity plays a role in band structure, we compare these results to the electronic structure of Y_2C and Al_2C. The known hybrid electride Y_2C has a similar ELF to Sc_2C, where there is electron character that is not associated with either the yttrium or carbon atoms (Figure 4-5b). Yttrium has an electronegativity value of 1.22, whereas scandium has a value of 1.36[44]. Therefore, Sc_2C has the most electronegative metal adjacent to the electride site yet synthesized in a 2D electride. We wanted to further explore a possible electride structure with a similar, yet more electronegative metal, aluminum (1.61). The theoretical layered Al_2C has the same structure type as Y_2C and Sc_2C, but there is less observed electron localization in this structure between the layers of Al_2C (Figure 4-5c). We calculated band structures and band gaps of Y_2C (Figure A4-5), Sc_2C (Figure 4-5d), and Al_2C (Figure A4-6) using the same calculation parameters. Although Y_2C is a semimetal, we find that Sc_2C and Al_2C are indirect band gap semiconductors. In these systems, increasing cation electronegativity (Y to Sc to Al) correlates with an increasing band gap (0 to 0.31 to 0.50 eV, respectively).

From these observations, we propose a model in which increasing electronegativity of metal leads to increased hybridization. As electronegativity of the metal increases, unoccupied states lower in energy and become closer in energy to the occupied electride states. Because the metal and electride states are close in energy and can physically overlap, the states hybridize. The consequence of this hybridization is that the bonding states are stabilized and adopt some character of the metal orbitals while the anti-bonding

states are destabilized and adopt some character of the electride orbitals (Figure A4-1). Thus, increasing metal electronegativity leads to increasing hybridization and a larger splitting between occupied and unoccupied states—i.e., the band gap increases.

If this model is correct, we should observe electride character in both the valence and conduction bands. Thus, we examined a partial density of the electride states (Figure 4-5d). We identified a sphere with a radius 1.2 Å centered at the electride lattice site, and integrating the charge density within this radius produces the partial density of states. This indicates that virtually all electride states are present around the Fermi level, with most in the valence band and a number in the conduction band. Additionally, we examined charge density at the top of the valence band and bottom of the conduction band in Sc_2C and Al_2C (Figure 4-5e-h). This indeed revealed electride character in both states, which could only result from hybridization of the electride electron and empty metal orbitals. This hybridization is analogous to donor-acceptor interactions[45], such as BH_3-NH_3, but with the 2D electron layer playing the role of the donor and the 2D M_2C atoms playing the role of acceptor. Therefore, as overlap increases between donor (electride electrons) and acceptor (empty metal-carbide orbitals), the valence and conduction bands split more, and the band gap increases. Presumably, the greatest hybridization seen in the Al_2C system is facilitated by aluminum being most electronegative, since the empty Al orbitals are closer in energy to the electride electrons. Additionally, this model is supported by the observation that Al_2C's electride shows lower localization than Sc_2C (Figure 4-5a,c), which would be a consequence of this hybridization. These observations and model directly lead us to a powerful design rule for layered semiconducting electrides: increasing metal electronegativity leads to increased electron-metal hybridization, yielding an increased band gap.

4.2.4 Exfoliation potential

To explore the possibility of exfoliating layered Sc_2C to make the Sc_2C electrene, we calculated the energy to separate two monolayers of Sc_2C. We obtained a value of 2.76 J/m^2, which is larger than that of Y_2C[46]. Compared to other known layered electrides with similar structures (Ca_2N and Sr_2N), Sc_2C and Y_2C exhibit a similar trend wherein the electride with the smaller cation has a larger binding energy. This is likely due to the smaller cation naturally having a greater electrostatic attraction due to the smaller distance between opposite charges.

We also examined the mechanical properties of Sc_2C and Y_2C, since these properties are known to predict the exfoliation potential of a material[47]. We found that Sc_2C has a higher bulk modulus than Y_2C, while its shear modulus and Young's modulus are both lower (Table A4-3). The higher bulk modulus and lower shear modulus indicate that the material has a higher exfoliation potential than Y_2C. We explored this experimentally but found that the material wouldn't exfoliate after sonicating in 1,3-dioxolane for 800 minutes[48]. SAED patterns and TEM images show that the particles that were produced were thick and irregularly shaped (Figure A4-8). Nevertheless, experimental exfoliation could lead to the realization of many exciting applications proposed for 2D Sc_2C[40,41] and could facilitate its study as an MXene-like derivative.

4.2.5 Stability in air

We tested the stability of this novel material in air because electrides are good reducing agents. Indeed, our calculations[49] of Sc_2C's work function—3.78 eV on the (0001) plane (Figure A4-6)—suggested that it could be a good electron donor, although less so than Y_2C[22], which has a slightly smaller work function and is more electropositive.

To explore the material's reactivity, we performed PXRD experiments after letting micron-sized particles (Figure A4-8) sit in air for varying intervals of time (Figure 4-6). The data shows that the material oxidizes slowly, with almost no change after sitting in air for one day. However, after four days, we observe that diffraction peaks shift to higher angles with decreased intensity and increased width. These attributes indicate a decrease in crystallinity and the formation of an amorphous material, which is the dominant phase by the final timepoint. Thus, unlike Hf_2S, Sc_2C is not naturally self-passivating.

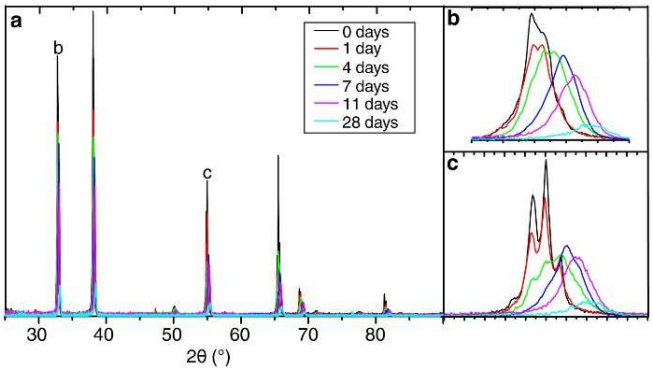


Figure 4-6. PXRD of Sc_2C oxidation. (a) X-ray diffraction patterns after various amounts of oxidation. (b) The diffraction pattern zoomed in between 54-56° two-theta. (c) The diffraction pattern zoomed in between 32.4-33.4° two-theta.

To better understand the mechanism of oxidation, we performed XPS. High-resolution scans of scandium and carbon were taken after 0, 1, and 11 days of sitting in air (Figure 4-7). Scandium shows four distinct doublets at the initial timepoint, indicating that several scandium species were initially present on the material's surface. Component A, Sc^{3+} [50], is likely due to surface oxidation during transfer into the XPS. Component B matches the value previously reported for Sc^{2+} [51]. Component C has peaks that lie between components A and B, suggesting that this Sc is in an environment that is between that of these two components. Component D has a small peak with a low binding energy, which may be attributed to either scandium or nitrogen. The carbon XPS spectra also reveals four species at the initial timepoint Components E and G are adventitious carbon and its oxidized counterpart, respectively[52]. Component F is likely the carbide of Sc_2C. This component has an extremely small binding energy compared to other known transition metal carbide species, which is not surprising from an electride[53]. Component H is likely an intermediate species as the carbide oxidizes.

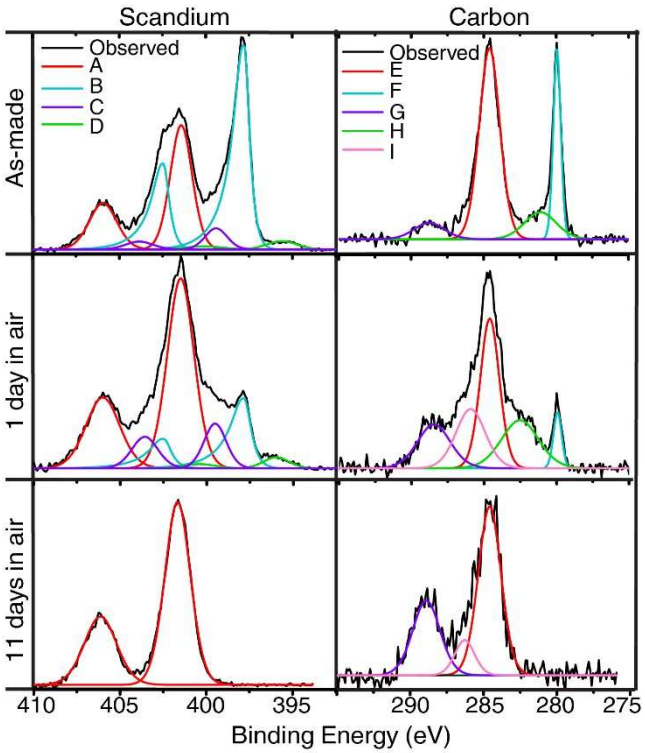


Figure 4-7. X-ray photoelectron spectroscopy spectra of scandium and carbon as-made, after 1 day in air, and after 11 days in air.

After one day of exposure to air, the Sc^{2+} peak decreases, the Sc^{3+} peak increases, and the carbide carbon peak decreases in intensity, indicating the sample is oxidizing. In the carbon spectra, a new species, component I, becomes apparent, and likely results from the adventitious carbon oxidizing. At the 11-day timepoint, the peaks associated with Sc_2C in both the scandium and carbon spectra have disappeared, indicating the surface was completely oxidized. The XRD data shows that there are still crystalline peaks present at the 11-day timepoint. From XRD and XPS, we conclude that an amorphous oxide forms on the surface of crystals first, and as the material continues to be exposed to air, oxygen diffuses further into the crystals until the bulk material becomes an amorphous oxide after 28 days. These results suggest that handling this material in air will require passivating coatings.

4.3 Conclusions

We have synthesized a new 2D inorganic electride, Sc_2C, which is the first semiconducting 2D electride. The discovery of this phase within the disordered rocksalt region of the Sc-C phase diagram suggests, in general, that other new electrides might be found within the rocksalt regions of many binary

phase diagrams. Along with our exploration of Al_2C, the trivalent metal carbides lead to a new design rule for semiconducting 2D electrides: that more electronegative cations in 2D electrides lead to higher degrees of hybridization, resulting in greater splitting of valence and conduction bands. Therefore, based on the electronegativity of the cation, we predict that the band gap in these electride materials may be controllably tuned. This first example of a semiconducting 2D electride suggests possible applications as a catalyst or photocatalyst, where the already-excellent electron-donating properties of the electride could be further enhanced by photoexcitation. In the case of Sc_2C, its small band gap specifically allows applications as an IR photodetector. These and other applications—e.g., in hydrogen storage[40,41] or as a fluoride ion battery electrode[10]—can now be experimentally explored.

REFERENCES

(1) Matsuishi, S., Toda, Y., Miyakawa, M., Hayashi, K., Kamiya, T., Hirano, M., Tanaka, I., Hosono, H. High-Density Electron Anions in a Nanoporous Single Crystal: $[Ca_{24}Al_{28}O_{64}]^{4+}(4e^-)$ *Science* **2003**, *301*, 626–630.

(2) Dye, J. L. Electrides: Early Examples of Quantum Confinement. *Acc Chem Res* **2009**, *42* (10), 1564–1572.

(3) Hosono, H.; Kitano, M. Advances in Materials and Applications of Inorganic Electrides. *Chem Rev* **2021**, *121*, 3121–3185.

(4) Toda, Y.; Yanagi, H.; Ikenaga, E.; Kim, J. J.; Kobata, M.; Ueda, S.; Kamiya, T.; Hirano, M.; Kobayashi, K.; Hosono, H. Work Function of a Room-Temperature, Stable Electride $[Ca_{24}Al_{28}O_{64}]^{4+}(4e^-)$. *Adv Mater* **2007**, *19* (21), 3564–3569.

(5) Gregory, D. H.; Bowman, A.; Baker, C. F.; Weston, D. P. Dicalcium Nitride, Ca_2N - A 2D "excess Electron" Compound; Synthetic Rotates and Crystal Chemistry. *J Mater Chem* **2000**, *10* (7), 1635–1641.

(6) Zhang, X.; Yang, G. Recent Advances and Applications of Inorganic Electrides. *J Phys Chem Lett* **2020**, *11* (10), 3841–3852.

(7) Kuganathan, N.; Hosono, H.; Shluger, A. L.; Sushko, P. v. Enhanced N_2 Dissociation on Ru-Loaded Inorganic Electride. *J Am Chem Soc* **2014**, *136* (6), 2216–2219.

(8) Qi, M.; Tang, C.; Zhou, Z.; Ma, F.; Mo, Y. Electride-Sponsored Radical-Controlled CO_2 Reduction to Organic Acids: A Computational Design. *Chem Eur J* **2020**, *26* (28), 6234–6239.

(9) Hu, J.; Xu, B.; Yang, S. A.; Guan, S.; Ouyang, C.; Yao, Y. 2D Electrides as Promising Anode Materials for Na-Ion Batteries from First-Principles Study. *ACS Appl Mater Interfaces* **2015**, *7* (43), 24016–24022.

(10) Druffel, D. L.; Pawlik, J. T.; Sundberg, J. D.; McRae, L. M.; Lanetti, M. G.; Warren, S. C. First-Principles Prediction of Electrochemical Electron–Anion Exchange: Ion Insertion without Redox. *J Phys Chem Lett* **2020**, *11* (21), 9210–9214.

(11) Toda, Y.; Matsuishi, S.; Hayashi, K.; Ueda, K.; Kamiya, T.; Hirano, M.; Hosono, H. Field Emission of Electron Anions Clathrated in Subnanometer-Sized Cages in $[Ca_{24}Al_{28}O_{64}]^{4+}(4e^-)$. *Adv Mater* **2004**, *16* (8), 685–689.

(12) Hosono, H.; Hayashi, K.; Kamiya, T.; Atou, T.; Susaki, T. New Functionalities in Abundant Element Oxides: Ubiquitous Element Strategy. *Sci Technol Adv Mater* **2011**, *12* (3), 034303.

(13) Menamparambath, M. M.; Park, J. H.; Yoo, H. S.; Patole, S. P.; Yoo, J. B.; Kim, S. W.; Baik, S. Large Work Function Difference Driven Electron Transfer from Electrides to Single-Walled Carbon Nanotubes. *Nanoscale* **2014**, *6* (15), 8844–8851.

(14) Dale, S. G.; Johnson, E. R. Theoretical Descriptors of Electrides. *J Phys Chem A* **2018**, *122* (49), 9371–9391.

(15) Redko, M. Y.; Jackson, J. E.; Huang, R. H.; Dye, J. L. Design and Synthesis of a Thermally Stable Organic Electride. *J Am Chem Soc* **2005**, *127* (35), 12416–12422.

(16) Li, K.; Gong, Y.; Wang, J.; Hosono, H. Electron-Deficient-Type Electride Ca_5Pb_3: Extension of Electride Chemical Space. *J Am Chem Soc* **2021**, *143* (23), 8821–8828.

(17) Walsh, A.; Scanlon, D. O. Electron Excess in Alkaline Earth Sub-Nitrides: 2D Electron Gas or 3D Electride? *J Mater Chem C* **2013**, *1* (22), 3525–3528.

(18) Brese, N. E.; O'Keeffe, M. Synthesis, Crystal and Physical Properties of Sr_2N. *J Solid State Chem* **1990**, *87*, 134–140.

(19) Chanhom, P.; Fritz, K. E.; Burton, L. A.; Kloppenburg, J.; Filinchuk, Y.; Senyshyn, A.; Wang, M.; Feng, Z.; Insin, N.; Suntivich, J.; Hautier, G. Sr_3CrN_3: A New Electride with a Partially Filled d-Shell Transition Metal. *J Am Chem Soc* **2019**, *141* (27), 10595–10598.

(20) Reckeweg, O.; DiSalvo, F. J. Crystal Structure of Dibarium Mononitride, Ba_2N, an Alkaline Earth Metal Subnitride. *Z Krist - New Cryst Struct* **2005**, *220* (1–4), 549–550.

(21) Atoji, M.; Kikuchi, M. Crystal Structures of Cubic and Trigonal Yttrium Hypocarbides; A Dimorphically Interphased Single-Crystal Study. *J Chem Phys* **1969**, *51* (9), 3863–3872.

(22) Zhang, X.; Xiao, Z.; Lei, H.; Toda, Y.; Matsuishi, S.; Kamiya, T.; Ueda, S.; Hosono, H. Two-Dimensional Transition-Metal Electride Y_2C. *Chem Mater* **2014**, *26* (22), 6638–6643.

(23) Kang, S. H.; Kang, S. H.; Bang, J.; Chung, K.; Nandadasa, C. N.; Han, G.; Lee, S.; Lee, K. H.; Lee, K.; Ma, Y.; Ma, Y.; Oh, S. H.; Kim, S. G.; Kim, Y. M.; Kim, Y. M.; Kim, S. W.; Kim, S. W. Water- And Acid-Stable Self-Passivated Dihafnium Sulfide Electride and Its Persistent Electrocatalytic Reaction. *Sci Adv* **2020**, *6* (23), 1-8.

(24) Mudryk, Y.; Paudyal, D.; Pecharsky, V. K.; Gschneidner, K. A. Magnetic Properties of Gd_2C: Experiment and First Principles Calculations. *J Appl Phys* **2011**, *109* (7), 2–5.

(25) Lee, S. Y.; Hwang, J. Y.; Park, J.; Nandadasa, C. N.; Kim, Y.; Bang, J.; Lee, K.; Lee, K. H.; Zhang, Y.; Ma, Y.; Hosono, H.; Lee, Y. H.; Kim, S. G.; Kim, S. W. Ferromagnetic Quasi-Atomic Electrons in Two-Dimensional Electride. *Nat Commun* **2020**, *11* (1), 1–8.

(26) Hirayama, M.; Matsuishi, S.; Hosono, H.; Murakami, S. Electrides as a New Platform of Topological Materials. *Phys Rev X* **2018**, *8* (3), 31067.

(27) Inoshita, T.; Jeong, S.; Hamada, N.; Hosono, H. Exploration for Two-Dimensional Electrides via Database Screening and Ab Initio Alculation. *Phys Rev X* **2014**, *4* (3), 1–8.

(28) Zhou, J.; Shen, L.; Yang, M.; Cheng, H.; Kong, W.; Feng, Y. P. Discovery of Hidden Classes of Layered Electrides by Extensive High-Throughput Material Screening. *Chem Mater* **2019**, *31* (6), 1860–1868.

(29) Ma, Y.; Eremets, M.; Oganov, A. R.; Xie, Y.; Trojan, I.; Medvedev, S.; Lyakhov, A. O.; Valle, M.; Prakapenka, V. Transparent Dense Sodium. *Nature* **2009**, *458* (7235), 182–186.

(30) Dong, X.; Oganov, A. R.; Goncharov, A. F.; Stavrou, E.; Lobanov, S.; Saleh, G.; Qian, G. R.; Zhu, Q.; Gatti, C.; Deringer, V. L.; Dronskowski, R.; Zhou, X. F.; Prakapenka, V. B.; Konôpková, Z.; Popov, I. A.; Boldyrev, A. I.; Wang, H. T. A Stable Compound of Helium and Sodium at High Pressure. *Nat Chem* **2017**, *9* (5), 440–445.

(31) Tang, H.; Wan, B.; Gao, B.; Muraba, Y.; Qin, Q.; Yan, B.; Chen, P.; Hu, Q.; Zhang, D.; Wu, L.; Wang, M.; Xiao, H.; Gou, H.; Gao, F.; Mao, H. kwang; Hosono, H. Metal-to-Semiconductor Transition and Electronic Dimensionality Reduction of Ca_2N Electride under Pressure. *Adv Sci* **2018**, *5* (11), 1800666 (1-6).

(32) Mizoguchi, H.; Okunaka, M.; Kitano, M.; Matsuishi, S.; Yokoyama, T.; Hosono, H. Hydride-Based Electride Material, LnH_2 (Ln = La, Ce, or Y). *Inorg Chem* **2016**, *55* (17), 8833–8838.

(33) Liu, C.; Nikolaev, S. A.; Ren, W.; Burton, L. A. Electrides: A Review. *J Mater Chem C* **2020**, *8* (31), 10551–10567.

(34) Park, J.; Hwang, J. Y.; Lee, K. H.; Kim, S. G.; Lee, K.; Kim, S. W. Tuning the Spin-Alignment of Interstitial Electrons in Two-Dimensional Y_2C Electride via Chemical Pressure. *J Am Chem Soc* **2017**, *139* (48), 17277–17280.

(35) Rassaerts, H.; Nowotny, H.; Vinek, G.; Benesovsky, F. Zum System Scandium. *Inorg, Struct and Phys Chem* **1967**, *61*, 460–468.

(36) Krikorian, N. H.; Bowman, A. L.; Krupka, M. C.; Arnold, G. P. The Preparation and Crystal Structure of Sc_4C_3. *High Temp Science* **1969**, *1*, 360–366.

(37) Velikanova, T. Ya.; Eremenko, V. N.; Artyukh, L. v.; Bondar, A. A.; Gordiichuk, O. v. Methods of Investigation and Properties of Powder Metallurgy Materials: Phase Diagrams of Sc-M(IV-VII)-C Systems. *Soviet Powder Metallurgy and Metal Ceramics* **1989**, *28*, 711–718.

(38) Khazaei, M.; Arai, M.; Sasaki, T.; Chung, C. Y.; Venkataramanan, N. S.; Estili, M.; Sakka, Y.; Kawazoe, Y. Novel Electronic and Magnetic Properties of Two-Dimensional Transition Metal Carbides and Nitrides. *Adv Funct Mater* **2013**, *23* (17), 2185–2192.

(39) Bae, S.; Espinosa-García, W.; Kang, Y. G.; Egawa, N.; Lee, J.; Kuwahata, K.; Khazaei, M.; Ohno, K.; Kim, Y. H.; Han, M. J.; Hosono, H.; Dalpian, G. M.; Raebiger, H. MXene Phase with C3 Structure Unit: A Family of 2D Electrides. *Adv Funct Mater* **2021**, *31*, 2100009 (1–8).

(40) Hu, Q.; Sun, D.; Wu, Q.; Wang, H.; Wang, L.; Liu, B.; Zhou, A.; He, J. MXene: A New Family of Promising Hydrogen Storage Medium. *J Phys Chem A* **2013**, *117* (51), 14253–

(41) Hu, Q.; Wang, H.; Wu, Q.; Ye, X.; Zhou, A.; Sun, D.; Wang, L.; Liu, B.; He, J. Two-Dimensional Sc_2C: A Reversible and High-Capacity Hydrogen Storage Material Predicted by First-Principles Calculations. *Int J Hydrogen Energy* **2014**, *39* (20), 10606–10612.

(42) Rietveld, H. M. The Rietveld Method. *Phys Scr* **2014**, *89* (9).

(43) Kononov, A.; Kuznetsov, S.; Polyakov, E. Electrorefining in Molten Salts-an Effective Method of High Purity Tantalum, *Hafnium and Scandium Metal Production*; **1995**, *218*, 173-176.

(44) A. Louis Allred. Electronegativity Values from Thermochemical Data. *J Inorg Nucl Chem* **1961**, *17*, 215–221.

(45) Woomer, A. H.; Druffel, D. L.; Sundberg, J. D.; Pawlik, J. T.; Warren, S. C. Bonding in 2D Donor-Acceptor Heterostructures. *J Am Chem Soc* **2019**, *141* (26), 10300–10308.

(46) Druffel, D. L.; Woomer, A. H.; Kuntz, K. L.; Pawlik, J. T.; Warren, S. C. Electrons on the Surface of 2D Materials: From Layered Electrides to 2D Electrenes. *J Mater Chem C* **2017**, *5*, 11196–11213.

(47) Jia, X.; Shao, Q.; Xu, Y.; Li, R.; Huang, K.; Guo, Y.; Qu, C.; Gao, E. Elasticity-Based-Exfoliability Measure for High-Throughput Computational Exfoliation of Two-Dimensional Materials. *NPJ Comput Mater* **2021**, *7* (1), 1–8.

(48) Druffel, D. L.; Kuntz, K. L.; Woomer, A. H.; Alcorn, F. M.; Hu, J.; Donley, C. L.; Warren, S. C. Experimental Demonstration of an Electride as a 2D Material. *J Am Chem Soc* **2016**, *138* (49), 16089–16094.

(49) Fall, C. J.; Binggeli, N.; Baldereschi, A. Deriving Accurate Work Functions from Thin-Slab Calculations. *J Phys Condens Matter* **1999**, *11* (13), 2689–2696.

(50) Biesinger, M. C.; Lau, L. W. M.; Gerson, A. R.; Smart, R. S. C. Resolving Surface Chemical States in XPS Analysis of First Row Transition Metals, Oxides and Hydroxides: Sc, Ti, V, Cu and Zn. *Appl Surf Sci* **2010**, *257* (3), 887–898.

(51) Merrick, J. Bonding in Scandium Monosulfide a NaCl Crystal Type, *Iowa State University*, **1980**.

(52) Barr, T. L.; Seal, S. Nature of the Use of Adventitious Carbon as a Binding Energy Standard. *J Vac Sci Technol* **1995**, *13* (3), 1239–1246.

(53) Ramqvist, L.; Hamrin, K.; Johansson, G.; Fahlman, A.; Nordling, C. Charge Transfer in Transition Metal Carbides and Related Compounds Studied by ESCA. *J Phys Chem Solids* **1969**, *30*, 1835–1847.

CHAPTER 5: HYDROGENATION OF Sc_2C

5.1 Introduction

Hydrogen is plentiful, lightweight, and produces water vapor when burned, suggesting its use as a fuel for airplanes. Despite this promise, its low density makes its storage a challenge, especially for applications that are volume-limited[1,2]. High-pressure gas storage and low-temperature liquid storage are possible storage mechanisms, but both come with challenges when incorporating them into a mobile system[3–7].

Solid hydrogen storage uses solid materials to store hydrogen under ambient temperature and pressure, so is a promising method compared to current state-of-the-art technologies. The DOE standards for hydrogen storage capacity are 6.5 wt % operating between -40 to 60 °C but, currently, no hydrogen storage materials meet these standards[8]. 2D Sc_2C is predicted to be an excellent hydrogen storage material with 8 wt. % capacity[9,10], so we sought to explore a possible hydrogenated structure of Sc_2C. While 0D[11] and 1D[12] electrides have been studied for hydrogen storage, 2D electrides have yet to be rigorously explored as hydrogen storage materials. Studying Sc_2C as a hydrogen storage material could lead to a better understanding of 2D electrides' ability to store hydride. However, there is no known Sc_2C hydrogenated structure, so I sought to investigate possible Sc-C-H structures.

In chapter 4, I demonstrated the advantage of using evolutionary algorithms to find novel structure types within a phase diagram because of random structure generation. Still, because they create such a large amount of unreasonable structures, they take significant computational power and time to search phase diagrams. Especially in ternary phase diagrams, they struggle to find the ground states in a reasonable amount of time[13]. Given this challenge, I used ionic substitution to predict a structure in the Sc-C-H system. Structure prediction using chemical substitution rules has long been used to experimentally explore phase diagrams, but Hautier *et. al.* recently developed an algorithm that performs statistically probable substitutions to probe structures in new compositions[14]. This algorithm

finds that yttrium and scandium are similar metals, so we substitute the yttrium in the known Y_2CH_2[15,16] for scandium to predict a Sc_2CH_2 structure.

5.2 Computational properties exploration

Hydride diffusion in hydrogen storage materials is a rate-limiting step for their use in energy devices[17], so fast diffusion kinetics are important. To understand the kinetics of hydride diffusion in Sc_2CH_2, we ran an NEB calculation between two tetrahedral H^- sites and find that the barrier for hydride diffusion is 229 meV (Figure 5-). Because this structure is layered, all sites are accessible by hopping through the tetrahedral sites, so we expect this to be the main mechanism of H^- diffusion in Sc_2CH_2. Additionally, this diffusion barrier is lower than that for Li^+ diffusion in both $LiCoO_2$ (~300 meV[18]) and graphite (~260 meV[19]) in commercial LIBs, suggesting that H^- diffusion in Sc_2CH_2 will be very fast at room temperature.

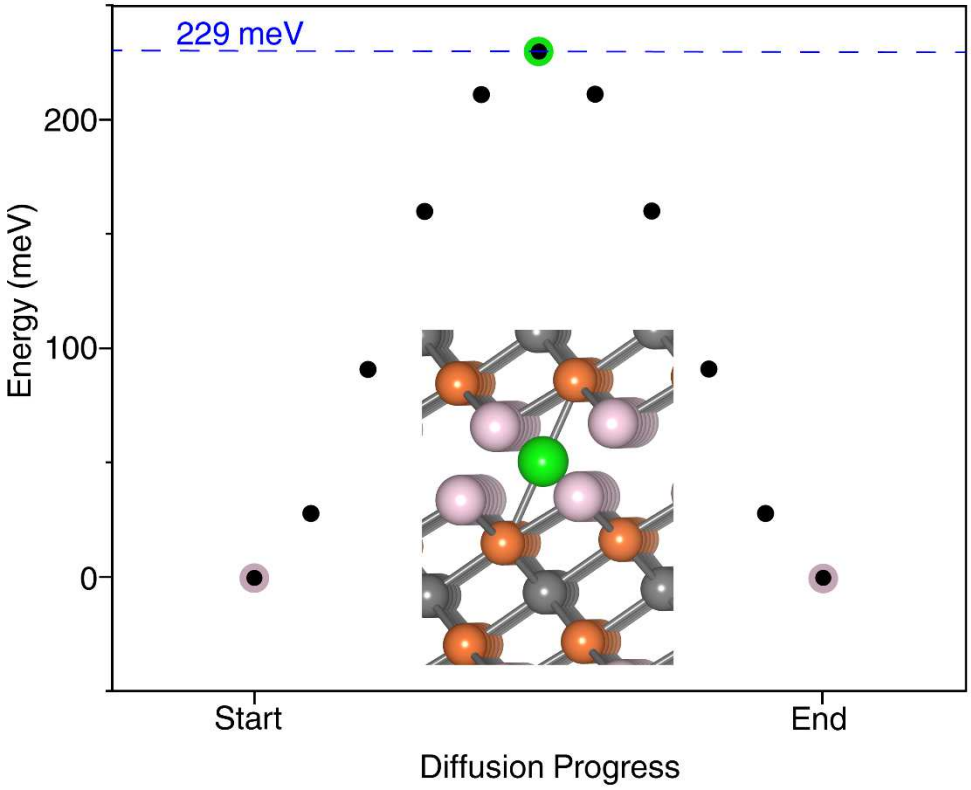


Figure 5-1. NEB calculation of Sc_2CH_x. The blue dashed line shows the activation barrier, and the structure with the diffusing ion is shown in the inset. The green hydride ion is the transition state and the pink hydride ions are the initial states, which are all symmetrically equivalent. The colored points on the graph correspond to the colored positions in the structure.

Currently, the metal hydrides used in hydrogen storage are insulators[20], and based on previous calculations on Sc_2CF_2 (Figure A5-1), I expected Sc_2CH_2 to be a semiconductor. However, we found that Sc_2CH_2 is a semi-metal (Figure 5-2). In both the Sc_2CF_2 and the Sc_2CH_2, the valence band contains scandium and carbon orbitals while the conduction band contains only scandium orbitals. The structure is the same and the oxidation states should be similar, so the change in band structure around the Fermi level must arise from differences in the orbital overlap between the scandium and anion orbitals. Specifically, there should be a greater coulombic interaction between scandium and fluoride than scandium and hydride because of the larger electronegativity of F^-. It's possible that this increased interaction stabilizes the scandium-occupied orbitals and destabilizes the scandium-unoccupied orbitals in the fluoride relative to the hydride, creating a larger band gap. The semi-metallic behavior in Sc_2CH_2 indicates the material could be applied in electrocatalysis in addition to hydrogen storage.

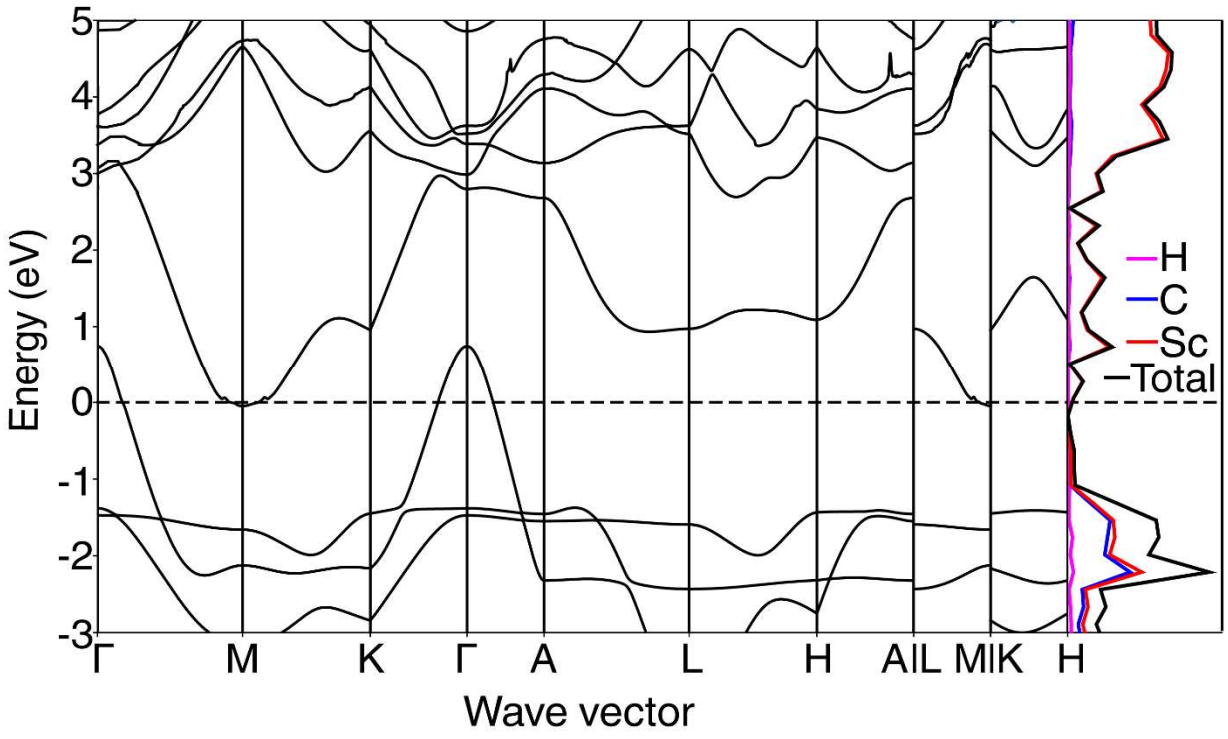


Figure 5-2. Band structure and DOS of Sc_2CH_2. This material is a semi-metal.

5.3 Synthesis

We optimized our predicted Sc_2CH_2 structure using the PBEsol functional[21] to best predict lattice parameters. After optimization, the space group is P-3m1 and lattice parameters are $a = b = 3.38$ Å and c

= *5.50 Å*. We attempted the hydrogenation of Sc_2C using a high-temperature synthesis with hydrogen gas via the procedure described in section 2.3.2. After the reaction, we performed PXRD experiments on the product at room temperature and refined the pattern using the Rietveld method[22] (Figure 5-3). The product contained a mixture of our predicted Sc_2CH_2 and Sc_2C in a mixture of 3:1. After refinement, we find no difference between the predicted and experimental structures in *a* and <1% difference in *c*, indicating that our model fits the refined structure well (Figure 5-3 inset).

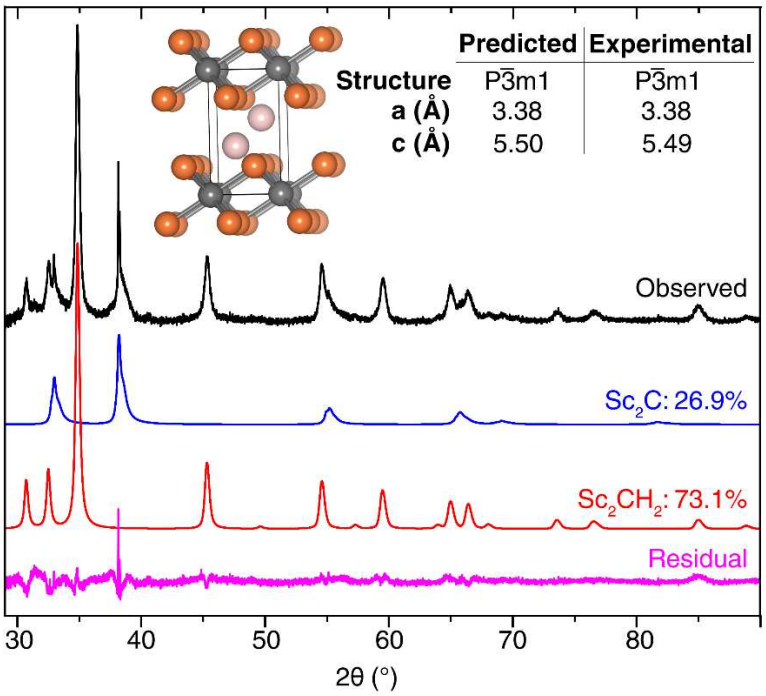


Figure 5-3. PXRD pattern of Sc_2C hydrogenation. The product contains a mixture of Sc_2C and Sc_2CH_x. The structure of Sc_2CH_2 is shown in the inset, and the experimentally refined structure (where x=2) is compared to the structure calculated using the substitution method and optimized using the PBE-sol functional.

Using Scherrer's equation (described in section 2.4.1, Eqn. 2.17) to calculate the domain size from the peak shape, we find that the Sc_2C domains (>100 nm) are almost an order of magnitude larger than the Sc_2CH_2 domains (~20 nm). This might suggest that nucleation of Sc_2CH_2 occurs at multiple locations in a Sc_2C domain, which is indicative of fast insertion kinetics.

With this analysis, it is important to consider the limits of PXRD; hydrogen is so light that we cannot probe it with PXRD. Specifically, although we have high certainty of the Sc and C locations, we lack knowledge of the H locations. We can gain some insight from the Y-C-H system, where it has been found that an increase in hydrogen content (Y_2CH_2 vs. $Y_2CH_{2.55}$) causes the lattice to contract by 0.06 Å[15]. While our experiment suggests that the lattice is slightly contracted compared to our model (0.01 Å), we would expect the lattice to be more highly contracted with a large excess of hydrogen. This suggests that $x<2.55$ in Sc_2CH_x. Additionally, we computationally modeled several possible Sc_2CH_x structures with $x=1$ and found that the lowest energy structure (by 79.3 meV) takes on the R-3m space group (similar to Sc_2C) rather than the P3m1 space group with a lattice contraction (similar to $Y_2CH_{2.55}$). Therefore, we expect that $x>1$ in Sc_2CH_x. Still, we cannot gauge the hydrogen content within that range ($1<x<2.55$) through PXRD alone. Supplementary experiments to explore the interlayer hydride structure are needed and underway.

To confirm excess oxygen is not present in the hydrogenated sample, causing the change in structure, we performed energy dispersive x-ray spectroscopy (EDS) via transmission electron microscopy (TEM) on the samples before and after hydrogenation (Table 5-). The amount of carbon cannot give insight into the sample because the TEM grid contains lacey carbon; depending on sample thickness and placement on the grid, the values of scandium to carbon will vary. Thus, we only consider the oxygen-to-scandium ratio. From EDS, we find that there is a small amount of oxygen (<4%) in each sample, presumably from transfer to the TEM and our synthesis; however, there is not a large difference in the amount of oxygen-to-scandium between samples (3% in Sc_2C and 5% in Sc_2CH_x). This small difference would not cause a change in structure in 75% of the sample and supports our conclusion that the change in structure originates from hydrogen in the sample rather than an excess of oxygen.

Table 5-1. EDS comparing oxygen:scandium of Sc_2C to Sc_2CH_x sample.

Ratio	Sc_2C sample	Sc_2CH_x sample
O:Sc	3.0%	5.0%

5.4 Exfoliation potential

From DFT, I calculated the binding energy of Sc_2CH_2 to be 1.53 J/m^2. Compared to an analogous material we studied, Y_2CF_2 (0.90 J/m^2)[23], and a material previously exfoliated in our lab, Ca_2N (1.11 J/m^2)[24], it has a higher binding energy. Yet, it still has much lower binding energy than the Sc_2C electride (2.76 J/m^2), so we performed exfoliation experiments similar to our previous study on Ca_2N, where we sonicated Sc_2CH_x in 1,3-dioxolane for 1,300 minutes. We took HRTEM images after the exfoliation (Figure 5-4), and found no thin particles that contained scandium and carbon. Given the hydrogenation mechanism proposed in Section 5.3, the small domain size and the particles not fully hydrogenating could cause failed exfoliation. Additionally, the exfoliation conditions need to be tuned. In summary, more experiments are needed to understand whether this material can be experimentally exfoliated.

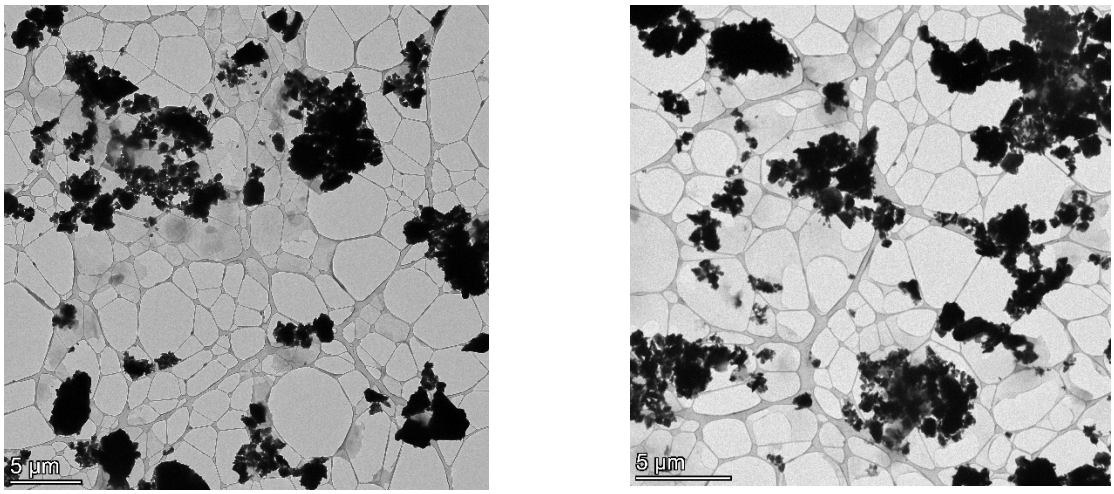


Figure 5-4. Representative HRTEM images of attempted exfoliation of Sc_2CH_2. In these images, there are many thick particles, but we found no evidence of thin particles with the correct composition. Consequently, any thin particles in the images are impurities.

5.5 Outlook

Using chemical substitution rules, we were able to correctly predict the structure of hydrogenated Sc_2C in experiments and calculations on this material indicate several promising applications in hydrogen storage and electrocatalysis. However, characterization of the hydride layer requires additional experiments, which we will do with hydrogen adsorption experiments[25] and neutron diffraction[26]. We've performed initial experiments on the exfoliation of this material, but further experiments are required to

understand whether this can be achieved. Understanding the structure and properties of Sc_2CH_x could lead to a more efficient search in the 2D electrides class for those that make promising hydrogen storage materials.

REFERENCES

(1) Fan, L.; Tu, Z.; Chan, S. H. Recent Development of Hydrogen and Fuel Cell Technologies: A Review. *Energy Rep* **2021**, *7*, 8421–8446.

(2) Dash, S. K.; Chakraborty, S.; Roccotelli, M.; Sahu, U. K. Hydrogen Fuel for Future Mobility: Challenges and Future Aspects. *Sustainability* **2022**, *14* (14), 8285.

(3) Rivard, E.; Trudeau, M.; Zaghib, K. Hydrogen Storage for Mobility: A Review. *Materials* **2019**, *12* (12).

(4) Mori, D.; Hirose, K. Recent Challenges of Hydrogen Storage Technologies for Fuel Cell Vehicles. *Int J Hydrogen Energy* **2009**, *34* (10), 4569–4574.

(5) Crabtree, R. H. Hydrogen Storage in Liquid Organic Heterocycles. *Energy Environ Sci* **2008**, *1* (1), 134–138.

(6) Eberle, U.; Arnold, G.; von Helmolt, R. Hydrogen Storage in Metal–Hydrogen Systems and Their Derivatives. *J Power Sources* **2006**, *154* (2), 456–460.

(7) Zhang, J.; Fisher, T. S.; Ramachandran, P. V.; Gore, J. P.; Mudawar, I. A Review of Heat Transfer Issues in Hydrogen Storage Technologies. *J Heat Transfer* **2005**, *127* (12), 1391–1399.

(8) Huang, Y.; Cheng, Y.; Zhang, J. A Review of High Density Solid Hydrogen Storage Materials by Pyrolysis for Promising Mobile Applications. *Ind Eng Chem Res* **2021**, 2737–2771.

(9) Hu, Q.; Sun, D.; Wu, Q.; Wang, H.; Wang, L.; Liu, B.; Zhou, A.; He, J. MXene: A New Family of Promising Hydrogen Storage Medium. *J Phys Chem A* **2013**, *117* (51), 14253–14260.

(10) Hu, Q.; Wang, H.; Wu, Q.; Ye, X.; Zhou, A.; Sun, D.; Wang, L.; Liu, B.; He, J. Two-Dimensional Sc_2C: A Reversible and High-Capacity Hydrogen Storage Material Predicted by First-Principles Calculations. *Int J Hydrogen Energy* **2014**, *39* (20), 10606–10612.

(11) Kitano, M.; Inoue, Y.; Yamazaki, Y.; Hayashi, F.; Kanbara, S.; Matsuishi, S.; Yokoyama, T.; Kim, S. W.; Hara, M.; Hosono, H. Ammonia Synthesis Using a Stable Electride as an Electron Donor and Reversible Hydrogen Store. *Nat Chem* **2012**, *4* (11), 934–940.

(12) Lu, Y.; Li, J.; Tada, T.; Toda, Y.; Ueda, S.; Yokoyama, T.; Kitano, M.; Hosono, H. Water Durable Electride Y_5Si_3: Electronic Structure and Catalytic Activity for Ammonia Synthesis. *J Am Chem Soc* **2016**, *138* (12), 3970–3973.

(13) Liu, X.; Niu, H.; Oganov, A. R. COPEX: Co-Evolutionary Crystal Structure Prediction Algorithm for Complex Systems. *npj Comput Mater* **2021**, *7* (1), 1–11.

(14) Hautier, G.; Fischer, C.; Ehrlacher, V.; Jain, A.; Ceder, G. Data Mined Ionic Substitutions for the Discovery of New Compounds. *Inorg Chem* **2011**, *50* (2), 656–663.

(15) Maehlen, J. P.; Yartys, V. A.; Hauback, B. C. Structural Studies of Deuterides of Yttrium Carbide. *J Alloys Compd* **2003**, *351*, 151–157.

(16) Lobier, G. Study of Yttrium Carbohydrides and Yttrium Sulfohydrides by X-Ray and Neutron Diffraction. *Les elements des terres rares* **1970**, 405–417.

(17) Novak, E.; Daemen, L.; Ramirez-Cuesta, A. J.; Cheng, Y.; Smith, R.; Egami, T.; Jalarvo, N. Uncovering the Hydride Ion Diffusion Pathway in Barium Hydride via Neutron Spectroscopy. *Sci Rep* **2022**, *12* (1).

(18) Okubo, M.; Tanaka, Y.; Zhou, H.; Kudo, T.; Honma, I. Determination of Activation Energy for Li Ion Diffusion in Electrodes. *J Phys Chem B* **2009**, *113* (9), 2840–2847.

(19) Toyoura, K.; Koyama, Y.; Kuwabara, A.; Oba, F.; Tanaka, I. First-Principles Approach to Chemical Diffusion of Lithium Atoms in a Graphite Intercalation Compound. *Phys Rev B Condens Matter Mater Phys* **2008**, *78* (21), 214303.

(20) Reshak, A. H. MgH2 and LiH Metal Hydrides Crystals as Novel Hydrogen Storage Material: Electronic Structure and Optical Properties. *Int J Hydrogen Energy* **2013**, *38* (27), 11946–11954.

(21) Perdew, J. P.; Ruzsinszky, A.; Csonka, G. I.; Vydrov, O. A.; Scuseria, G. E.; Constantin, L. A.; Zhou, X.; Burke, K. Restoring the Density-Gradient Expansion for Exchange in Solids and Surfaces. *Phys Rev Lett* **2008**, *100* (13), 1–4.

(22) Rietveld, H. M. The Rietveld Method. *Phys Scr* **2014**, *89* (9).

(23) Druffel, D. L.; Lanetti, M. G.; Sundberg, J. D.; Pawlik, J. T.; Stark, M. S.; Donley, C. L.; McRae, L. M.; Scott, K. M.; Warren, S. C. Synthesis and Electronic Structure of a Crystalline Stack of MXene Sheets. *Chem Mater* **2019**, *31* (23), 9788–9796.

(24) Druffel, D. L.; Kuntz, K. L.; Woomer, A. H.; Alcorn, F. M.; Hu, J.; Donley, C. L.; Warren, S. C. Experimental Demonstration of an Electride as a 2D Material. *J Am Chem Soc* **2016**, *138* (49), 16089–16094.

(25) Jordá-Beneyto, M.; Suárez-García, F.; Lozano-Castelló, D.; Cazorla-Amorós, D.; Linares-Solano, A. Hydrogen Storage on Chemically Activated Carbons and Carbon Nanomaterials at High Pressures. *Carbon* **2007**, *45* (2), 293–303.

(26) Ramirez-Cuesta, A. J.; Jones, M. O.; David, W. I. F. Neutron Scattering and Hydrogen Storage. *Mater Today* **2009**, *12* (11), 54–61.

APPENDIX: SUPPORTING INFORMATION FOR CHAPTER 3[c]

A3.1 Phases in the $[Y_2C]^{2+}(e^-)_2$-Y_2CF_2 system

The Y_2C stacking sequence in the experimentally determined crystal structures of $[Y_2C]^{2+}(e^-)_2$ and Y_2CF_2 are shown in Figure A3-1a and b, respectively. Recognizing that a stacking sequence change is possible upon EAX, we calculated hypothetical partially fluorinated phases in the O3 and T1 structures. We found that for insertion up to and including 1 F^-, the enthalpy of the O3 phase is thermodynamically favored in comparison to the T1 structure (Figure A3-1c). This is consistent with our expectation that the O3 structure offers an octahedral site where the F^- has a higher coordination number than it would be in the tetrahedral site of the T1 structure. In contrast, the T1 structure is thermodynamically favored in comparison to the O3 structure with insertion of any additional F^- beyond one equivalent per formula unit. This is also consistent with our expectation that the insertion of additional F^- forces the F^- into a tetrahedral site proximal to the carbon (C^{2-}) anion, which is less favorable because of electrostatic repulsion between anions (Figure A3-1d). In contrast, the T1 phase affords two tetrahedral sites with relatively long F–C distances, thus minimizing electrostatic repulsion. The same trends appear in the Sc_2CF_2 system (Figure A3-1c). However, we note that the hypothetical intermediate ABC-stacked (O3-type) Y_2CF is thermodynamically unstable vs. the convex hull ($[Y_2C]^{2+}(e^-)_2$ + Y_2CF_2) by 38 kJ/mol, which may indicate that the phase change occurs as an intercalation front or islands rather than a staging mechanism.

[c] Portions of this chapter reproduced with permission from Druffel, D. L.; Pawlik, J. T.; Sundberg, J. D.; McRae, L. M.; Lanetti, M. G.; Warren, S. C. First-Principles Prediction of Electrochemical Electron-Anion Exchange: Ion Insertion without Redox. *The Journal of Physical Chemistry Letters* **2020**, 11 (21), 9210-9214. Copyright 2020 American Chemical Society.

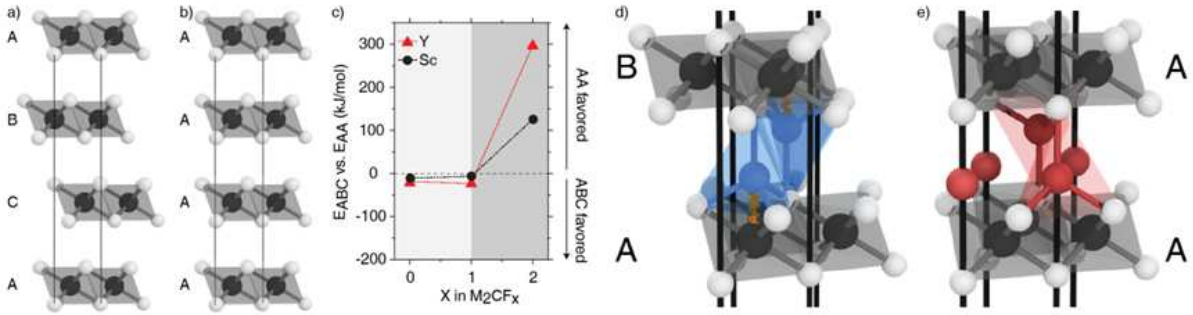


Figure A3-1. The two stacking sequences of Y_2C and Y_2CF_2. a) R-3m $[Y_2C]^{2+}(e^-)_2$ (ABC-stacked) b) P-3m1 Y_2CF_2 (AA-stacked). c) The relative stability of the stacking sequences as a function of x in Y_2CF_x. d) A representation of two layers of the ABC-stacked structure where the two tetrahedral sites are occupied by F^-, represented in blue. The proximity of the F^- to the carbon anions (black) is highlighted by yellow springs. e) A representation of the AA-stacked structure where the two tetrahedral sites are occupied by F^-, represented in red.

We further studied this through our cluster expansion and subsequent Monte Carlo simulations, and added an additional H1-3 phase. All 3 stacking sequences are shown in Figure A3-2. The H1-3 phase is a hypothetical structure of hybridized stacking sequences of the T1 and O3 phases that has an overall stacking sequence of AABBCC. We used an a lattice constant of 3.53 Å and c lattice constant of 17.12 Å, though the parameters and atomic positions of all cells used in the cluster expansion were fully optimized before calculating the energy.

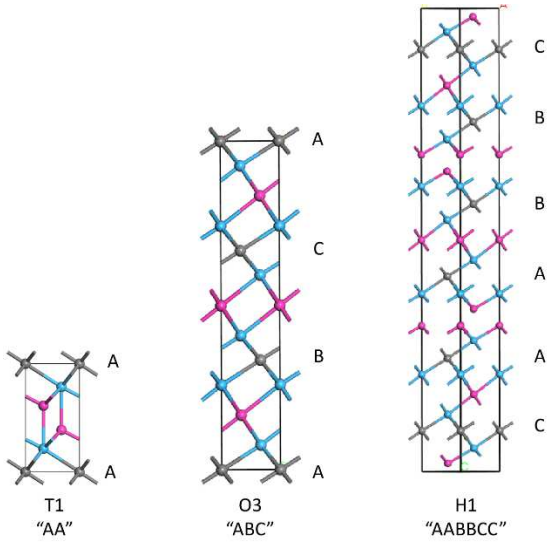


Figure A3-2. Crystal structures of the T1, O3, and H1-3 phases considered in our cluster expansion.

A3.2 Characteristics of the $[Y_2C]^{2+}(e^-)_2$-Y_2CF_2 as an anode in a fluoride-ion battery

In equation A3-1, we write a series of chemical equations that combine to give the potential of electron insertion into Y_2CF_2 versus Li/Li^+.

$$\begin{array}{lll} & Y_2CF_{2(s)} + 2Li_{(s)} \rightarrow [Y_2C]^{2+}(e^-)_{2(s)} + 2LiF_{(s)} & \Delta G_{rxn} \\ & 2LiF_{(s)} \rightarrow 2Li^+_{(solvated)} + 2F^-_{(solvated)} & \Delta G_{solv} \\ + & 2Li^+_{(solvated)} + 2e^- \rightarrow 2Li_{(s)} & E_{red}{}^{Li+} \\ \hline & Y_2CF_{2(s)} + 2e^-_{(s)} \rightarrow [Y_2C]^{2+}(e^-)_{2(s)} + 2F^-_{(solvated)} & E_{e\text{-}int}{}^{Y2CF2} \end{array} \qquad (A3\text{-}1)$$

In a hypothetical cell with lithium, the voltage of the cell, ΔE, is the sum of the potential of electron insertion into Y_2CF_2, $E_{e-int}{}^{Y2CF2}$, and the oxidation potential of lithium metal, $E_{ox}{}^{Li}$ (Eqn. A3-2). We can instead write the equation in terms of the reduction potential of Li^+ (Eqn. A3-4). Through the Nernst equation (Eqn. 3-5), we can relate the Gibbs free energy, ΔG, of the reduction reaction, to the voltage of the cell (Eqn. A3-9). The Gibbs free energy of the reaction is the sum of the Gibbs free energy of a solid-state reaction of Y_2CF_2 and lithium metal, ΔG_{rxn}, and the Gibbs free energy of the solvation of solid LiF, ΔG_{solv}. Substituting terms and rearranging the equation yields an equality (Eqn. A3-10) that allows us to estimate the potential of electron insertion into Y_2CF_2 vs. Li/Li^+ from values of ΔG_{rxn} and ΔG_{solv}.

$$\Delta E = E_{e-int}^{Y2CF2} + E_{ox}^{Li} \qquad (A3\text{-}2)$$

$$E_{ox}^{Li} = -E_{red}^{Li+} \quad \textit{(A3-3)}$$

$$\Delta E = E_{e-int}^{Y2CF2} - E_{red}^{Li+} \quad \textit{(A3-4)}$$

$$\Delta G = -nF(\Delta E) \quad \textit{(A3-5)}$$

$$\Delta G = \Delta G_{rxn} + \Delta G_{solv} \quad \textit{(A3-6)}$$

$$-nF(\Delta E) = \Delta G_{rxn} + \Delta G_{solv} \quad \textit{(A3-7)}$$

$$-nF(E_{e-int}^{Y2CF2} - E_{red}^{Li+}) = \Delta G_{rxn} + \Delta G_{solv} \quad \textit{(A3-8)}$$

$$E_{e-int}^{Y2CF2} = \frac{\Delta G_{rxn}}{-nF} + \frac{\Delta G_{solv}}{-nF} + E_{red}^{Li+} \quad \textit{(A3-9)}$$

$$E_{e-int\ vs.\frac{Li}{Li+}}^{Y2CF2} = \frac{\Delta G_{rxn} + \Delta G_{solv}}{-nF} \quad \textit{(A3-10)}$$

We approximated ΔG_{rxn} by neglecting the change in entropy of the solid reaction and calculating the enthalpy using DFT, affording a value of -209.3 kJ/mol. To estimate ΔG_{solv}, we used an experimental value of the energy of solvation of LiF (21.13 kJ/mol) in the ionic liquid, 1-butyl-3-methylimidazolium trifluoromethanesulfonate ([C_4C_1im][OTf])[(1)]. It is worthwhile to understand the sources of error and relative accuracy of this estimate. We performed four DFT calculations, each of which may contain an error of 1-2 kJ/mol, adding an error of ~4 kJ/mol. We neglected the change in the entropy of the solids. The sum of these terms at 300 K, each with a value of around 10 kJ/mol, likely gives an error of ~2 kJ/mol. Rather than [C_4C_1im][OTf], our experiments employed a different solvent, an ionic liquid consisting of N,N,N-trimethyl-

N-neopentylammonium fluoride and bis(2,2,2-trifluoroethyl) ether, which has a higher free energy of solvation for F^{-}[2]. The error associated with this term could be as large as 20 kJ/mol. Together these errors, ~26 kJ/mol, suggest a liberal estimate of 14% error. Therefore, the potential of electron insertion into Y_2CF_2 is +0.97 ± 0.13 V vs. Li/Li^+.

We calculated the cell voltage for a battery using $[Y_2C]^{2+}(e^-)_2/Y_2CF_2$ as the anode and Cu/CuF_2 as the cathode using the equation:

$$[Y_2C]^{2+}(e^-)_{2(s)} + 2CuF_{2(s)} \rightarrow Y_2CF_{2(s)} + 2Cu_{(s)} \quad \Delta G_{rxn} \qquad (A3\text{-}11)$$

The enthalpy of Cu was calculated using GGA while the enthalpy of CuF_2 was calculated using GGA+U (U =4.0 eV) so the ΔG was corrected according to the procedure developed by Jain *et. al.*[3] Following the procedure described above, we calculated the reduction potential of CuF_2 to be ~3.7 V vs. Li/Li+ consistent with reported results[2].

To calculate the maximum gravimetric capacity and maximum volumetric capacity, we used the following equations respectively, where *n* is the number of electrons, *F* is Faraday's constant, *MW* is the molecular weight of the unintercalated host lattice, *N* is Avogadro's number, and V_{unit} is the volume of the host lattice unit cell.

$$max\ gravimetric\ capacity = \frac{nF}{(3600)MW} \qquad (A3\text{-}12)$$

$$max\ volumetric\ capacity = \frac{nF}{(3600)NV_{unit}} \qquad (A3\text{-}13)$$

A3.3 Cluster expansion models

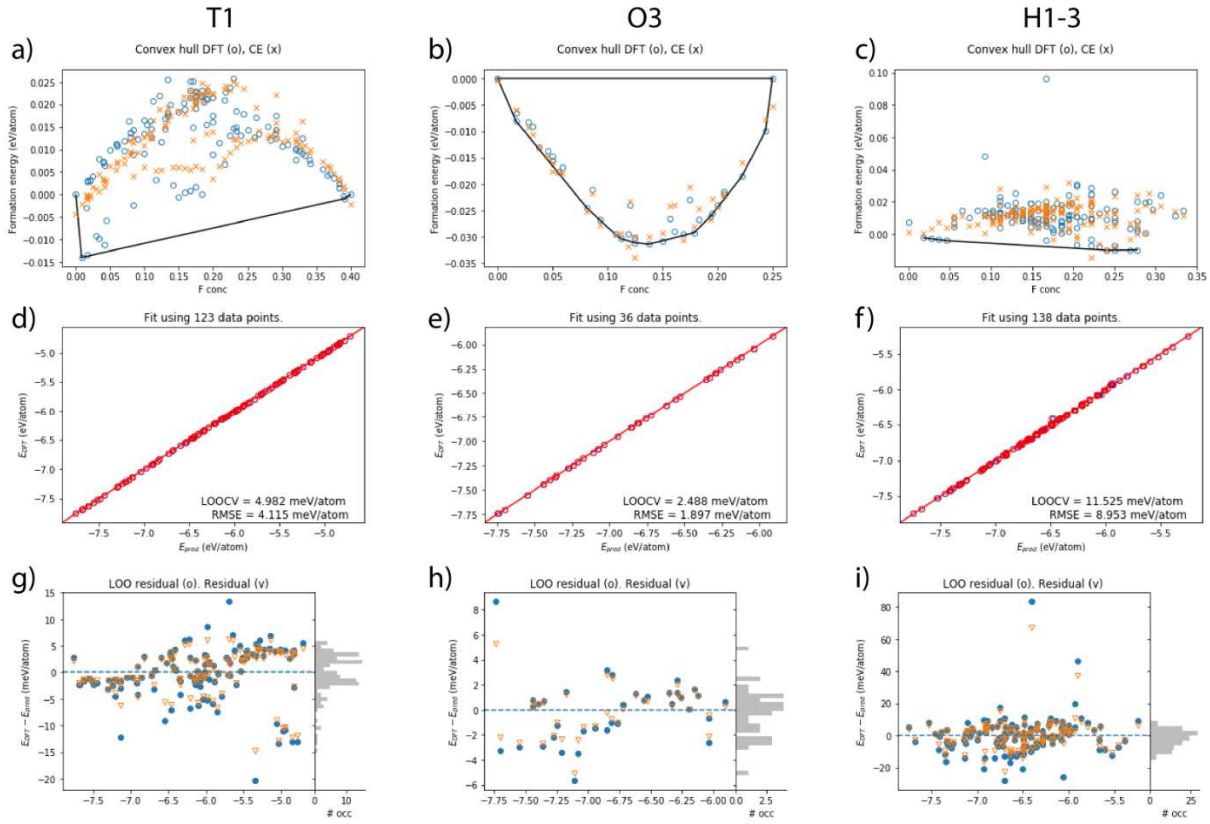


Figure A3-3. The cluster expansion models for the T1, O3, and H1-3 phases. a-c) The convex hull considering only the individual phase as a function of fluorine concentration with the concentration of fluorine reported as the fraction of total atoms in the cell. d-f) The fit of the energies predicted from the CE model to the energies calculated by DFT. g-h) The residual plots show a close match between the predicted values and DFT and show the random distribution of the times.

REFERENCES

(1) Kuzmina, O.; Bordes, E.; Schmauck, J.; Hunt, P. A.; Hallett, J. P.; Welton, T. Solubility of Alkali Metal Halides in the Ionic Liquid [C_4C_1im][OTf]. *Phys Chem Chem Phys* **2016**, *18* (24), 16161–16168.

(2) Davis, V. K.; Bates, C. M.; Omichi, K.; Savoie, B. M.; Momčilović, N.; Xu, Q.; Wolf, W. J.; Webb, M. A.; Billings, K. J.; Hawn Chou, N.; Alayoglu, S.; McKenney, R. K.; Darolles, I. M.; Nair, N. G.; Hightower, A.; Rosenberg, D.; Ahmed, M.; Brooks, C. J.; Miller III, T. F.; Grubbs, R. H.; Jones, S. C. Room-Temperature Cycling of Metal Fluoride Electrodes: Liquid Electrolytes for High-Energy Fluoride Ion Cells. *Science* **2018**, *362* (6419), 1144–1148.

(3) Jain, A.; Hautier, G.; Ong, S. P.; Moore, C. J.; Fischer, C. C.; Persson, K. A.; Ceder, G. Formation Enthalpies by Mixing GGA and GGA + U Calculations. *Phys* Rev *B Condens Matter Mater Phys* **2011**, *84* (4), 045115.

APPENDIX: SUPPORTING INFORMATION FOR CHAPTER 4[d]

A4.1 Historical diffraction data

We compared the predicted x-ray diffraction pattern for layered Sc_2C to the diffraction pattern in Rassaerts *et. al.*[1] found that while many of the predicted peaks do match well with the published data, the 1967 pattern misses several intense peaks. These missing peaks are within 0.2° of other intense peaks which were observed. It is unclear whether the absence of neighboring peaks is due to instrumental broadening. Our inspection of papers from this era indicates that typical instruments had instrumental broadenings below 0.1° two-theta, and a larger width of peaks is indicative of higher structural disorder[2]. We, therefore, expect that the absence of peaks 0.1-0.2° apart suggests the previously synthesized material was not layered Sc_2C.

Table A4-1. Comparison of diffraction patterns for ScC_x.

Index	McRae *et. al.* Sc_2C XRD shifts	Rassaerts *et. al.*[27] Sc_2C XRD shifts	McRae *et. al.* Sc_2C XRD intensities	Rassaerts *et. al.* Sc_2C XRD intensities
(111)	16.2°	16.2°	5,080 – weak	Weak
(0-1-1)	32.7°	missing	20,000 – very strong	Missing
(222)	32.8°	32.9°	7,000 – very strong	Very strong
(211)	38.0°	38.2°	20,000–very strong	Very strong
(3-22)	50.1°	50.3°	1,300 – very weak	Very weak
(10-1)	54.7°	55.0°	6,750 - strong	Strong
(332)	54.9°	missing	5,890 - weak	Missing
(00-2)	65.15°	missing	2,300 - weak	Missing
(321)	65.24°	65.6°	4,290 – weak	Medium strong
(433)	65.4°	missing	1,815 – weak	Missing
(0-2-2)	68.4°	69.0°	2,770 - weak	Medium weak

[d] Portions of this chapter reproduced with permission from McRae, L. M.; Radomsky, R. C.; Pawlik, J. T.; Druffel, D. L.; Sundberg, J. D.; Lanetti, M. G.; Donley C. L.; White, K. L.; Warren, S. C. Sc_2C: a 2D Semiconducting Electride. *Journal of the American Chemical Society* **2022**, 144 (24), 10862-10869. Copyright 2022 American Chemical Society.

(422)	81.1°	81.5°	1,370 - weak	Weak

A4.2 Supplementary results and discussion

We propose that the band gap in Sc_2C arises from increased electron-atom hybridization compared to the previously discovered 2D electrides. An illustration of this idea is provided in Figure A4-1, where the vacancy-centered state is filled with electrons while the atom-centered state (in Sc_2C, Sc d-orbitals) is empty. Because the filled vacancy-centered state and the empty atom-centered state are close in energy, they hybridize to form a filled lower energy state (corresponding to the valence band) and an unfilled higher energy state (corresponding to the conduction band). Therefore, the splitting between the valence and conduction bands is a direct consequence of hybridization. As the atom-centered state (which corresponds to the cation) becomes lower in energy, there will be a greater degree of hybridization and thus, an increased energy split between valence and conduction bands. Koopmans' theorem established the negative direct relationship between electron affinity and energy of the LUMO[3]. From this, we can conclude that as the electronegativity of the cation increases, the atom-centered state will sit at lower energies. Therefore, there is a direct relationship between cation electronegativity and hybridization, and thus, band gap in these electride materials.

It is also important to note that hybridization between electride and atomic states does not guarantee that a material will be a semiconductor. As in any system, the resulting bands must be "fully" occupied and "fully" unoccupied. The occurrence of hybridization simply allows bands that are near the Fermi level to mix and separate in energy—a necessary but not sufficient criterion for a semiconductor.

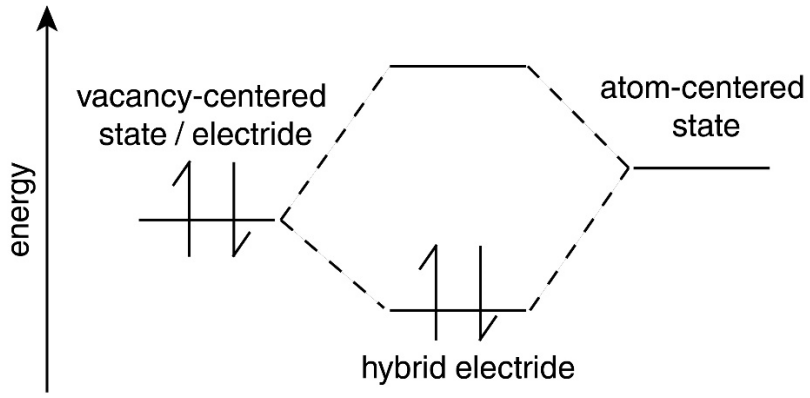
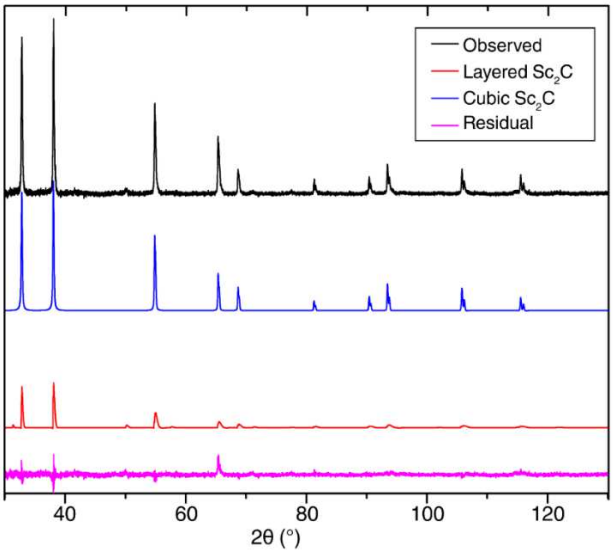


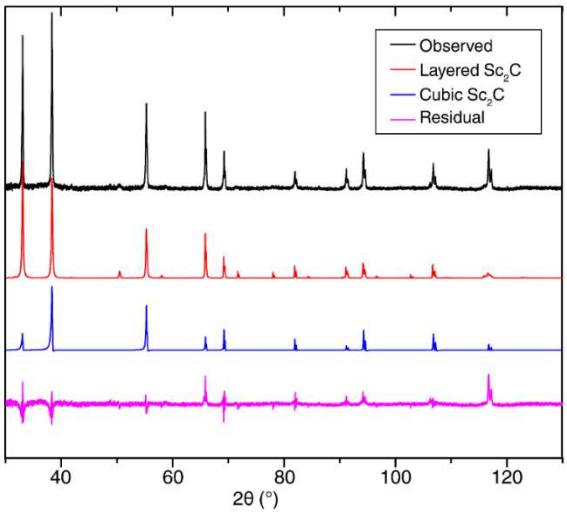
Figure A4-1. An illustration of electride-atom hybridization.

We obtained XRD data for the product after arc-melting (without annealing), and found a high amount of the cubic phase (Figure A4-2). After annealing, as discussed in the main text, we found a much larger amount of the layered phase at a ratio of 2:0.99 of Sc:C. On both the carbon-poor (Figure A4-3) and carbon-rich (Figure A4-4) sides of the 2:1 stoichiometry, we find a high amount of the cubic phase. In the carbon-rich diffraction pattern, we also see evidence of the Sc_4C_3 phase.



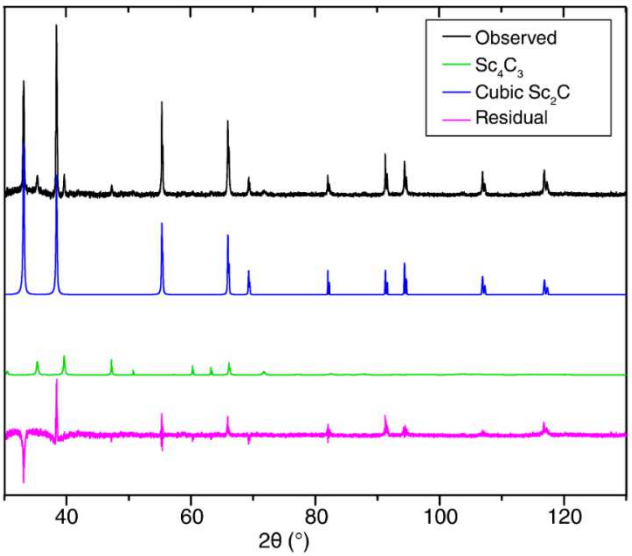
Occupancies	Sc	C	Quant
Cubic ScC_x	1.00	0.5	59%
Layered Sc_2C	1.00	1.00	41%

Figure A4-2. XRD pattern of typical arc-melting synthesis without annealing. The occupancies of Sc and C, and the quantity of both the cubic and layered phases from Rietveld refinement are shown in the corresponding table.



Occupancies	Sc	C	Quant
Cubic ScC_x	1.00	0.5	48.7%
Layered Sc_2C	1.00	1.00	51.3%

Figure A4-3. XRD pattern of $Sc_2C_{0.95}$. The occupancies of Sc and C, and the quantity of both the cubic and layered phases from Rietveld refinement are shown in the corresponding table.



Occupancies	Sc	C	Quant
Cubic ScC_x	1.00	0.5	88.1%
Sc_4C_3	1.00	1.00	11.9%

Figure A4-4. XRD pattern of $Sc_2C_{1.13}$. The occupancies of Sc and C, and the quantity of both the cubic and layered phases from Rietveld refinement are shown in the corresponding table.

We calculated the band structure for both Y_2C (Figure A4-5) and Al_2C (Figure A4-6) using the same calculation parameters as Sc_2C. The band structure of Y_2C as compared to Sc_2C has the same general shape with the difference in spins and electronegativity of the cations as the primary reasons for the different electronic properties. The band structure of Al_2C is nearly identical to that of Sc_2C, except that relative energies of the valence band at the L and B_1 points are reversed.

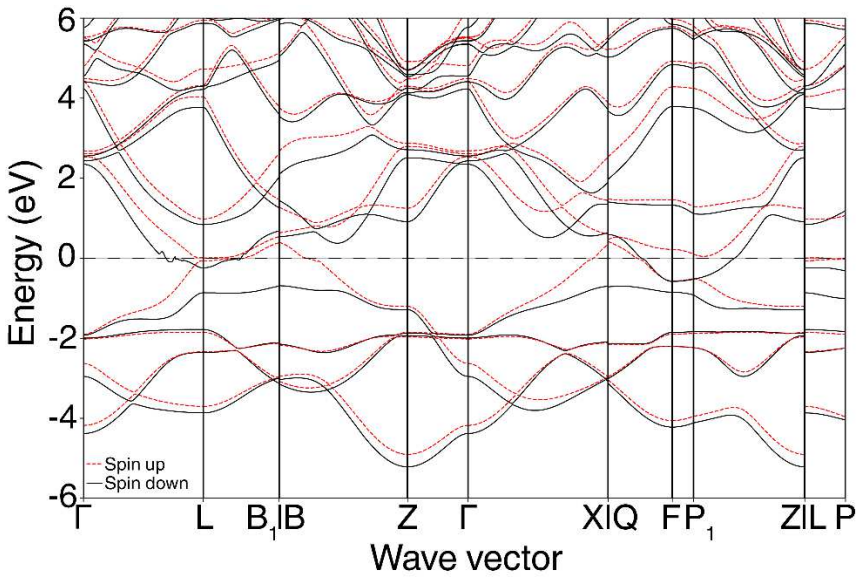


Figure A4-5. The band structure of Y_2C.

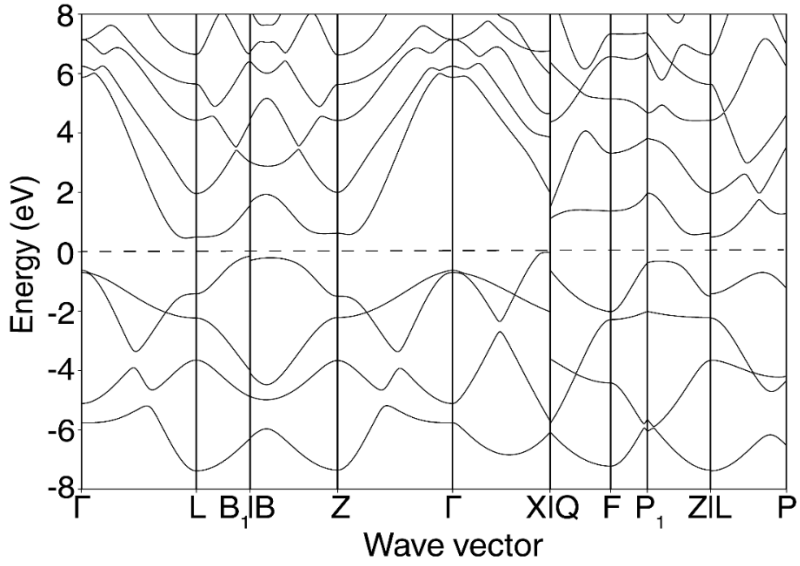


Figure A4-6. The band structure of Al_2C.

To explore how a change in lattice parameters would affect the electronic structure, we ran a band structure calculation on the Al_2C structure, where we substituted Al for Sc (Figure A4-7). While the overall composition was the same as the Sc_2C structure, there was a decrease in lattice parameters. We found that the band gap slightly decreased, from 0.31 eV in the native Sc_2C structure to 0.25 eV in the smaller structure. While many parts of the band diagram changed slightly in the strained structure, we focus on a change in the L-point, where there is a concentration of electride states. Our hypothesis relies on the idea

that in symmetries where the Sc and electride orbitals have the correct orientation to mix, increased mixing will create greater splitting. At the L-point, we have a high degree of mixing, which we demonstrate in the main text Figure 4-5e and f. With smaller lattice parameters, we would expect a greater degree of mixing to occur between the electride and Sc states at the L-point causing a greater split between valence and conduction bands. In the native Sc_2C structure, there is a split of 0.48 eV at the L-point whereas, in the smaller structure, we observe a splitting of 0.84 eV. This greater splitting further supports our hypothesis that when the Sc and electride orbitals have greater overlap, there is an increased split between the occupied and unoccupied orbitals.

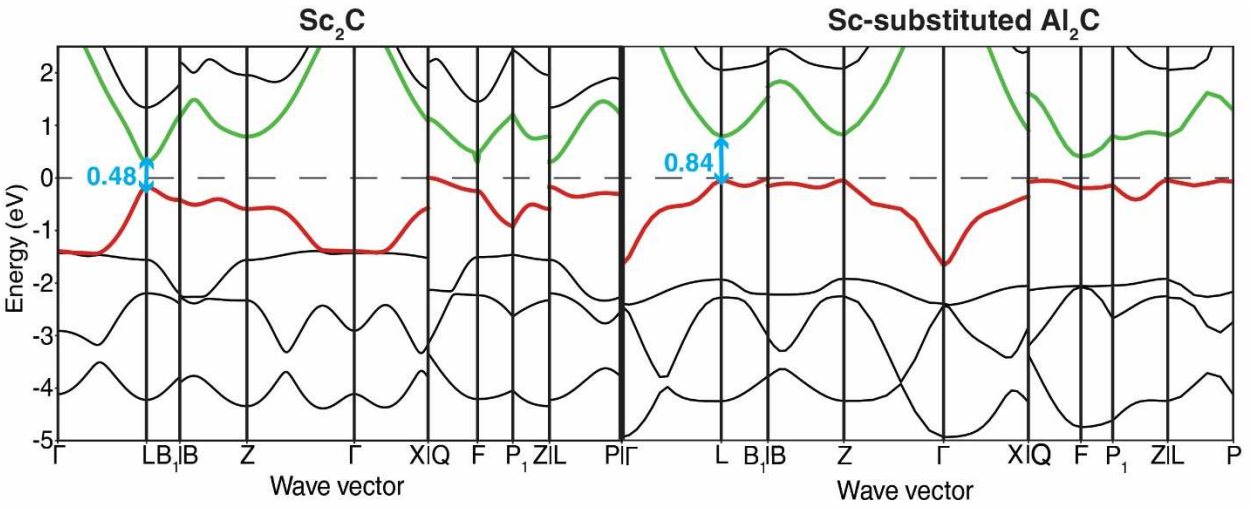


Figure A4-7. The band structure of Sc_2C compared to that of Sc-substituted Al_2C.

We calculated the work function for Sc_2C to understand its electron-donating properties and compare it to Y_2C. The details of the potential change over position are included for (0001) (Figure A4-8) and (11-20) (Figure A4-9), where the difference between the Fermi and vacuum levels gives the calculated work function.

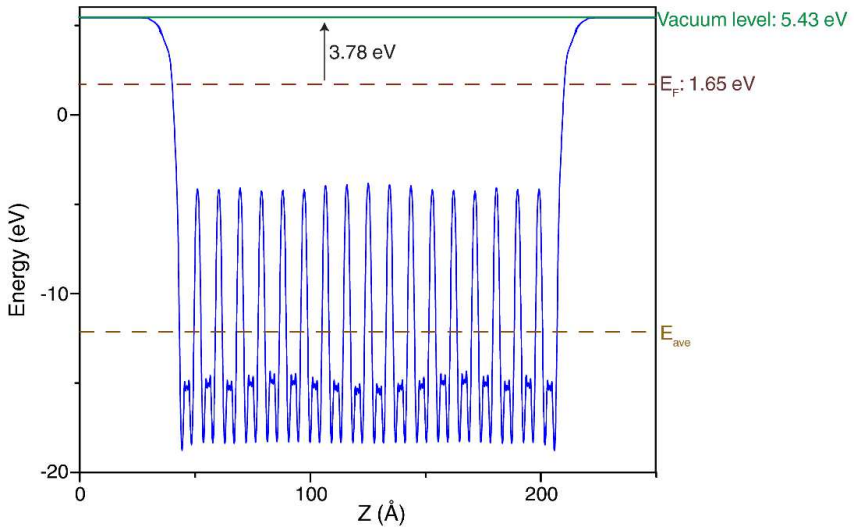


Figure A4-8. The calculated work function of Sc_2C for (0001).

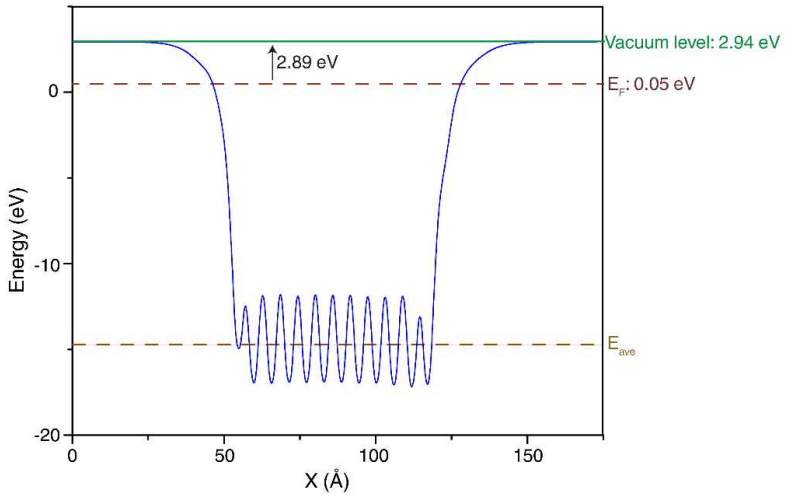


Figure A4-9. The calculated work function of Sc2C for (11$\bar{2}$0).

We calculated the mechanical properties of Sc_2C as it compares to Y_2C to understand its potential for exfoliation. A comparison between the intralayer and interlayer is included in Table A4-2. Compared to Y_2C, the Sc_2C values indicate a greater degree of anisotropy because the intralayer stiffness tensor of Sc_2C is 110% greater than its interlayer counterpart, whereas the intralayer tensor of Y_2C is only 44% larger. A comparison between Sc_2C and Y_2C of other mechanical properties is included in Table A4-3, and a deeper analysis of these values is included in the main text.

Table A4-2. Interlayer and Intralayer stiffness tensors for Sc_2C and Y_2C.

	Sc_2C	Y_2C[4]
Intralayer stiffness (GPa)	286.8	150
Interlayer stiffness (GPa)	136.7	104

Table A4-3. Various moduli of Sc_2C and Y_2C.

	Sc_2C	Y_2C[5]
Bulk Modulus (GPa)	82.7	68
Shear Modulus (GPa)	16.5	42
Young's Modulus (GPa)	46.3	104.5
Poisson's Ratio	0.407	0.24
Bulk/Shear Ratio	5.027	1.62

To experimentally test whether Sc_2C could be exfoliated, we performed a liquid exfoliation process before TEM imaging. In previous work, the electride Ca_2N was shown to form two-dimensional sheets after exfoliation[6]. We carried out the same exfoliation process on Sc_2C by sonicating in 1,3-dioxolane for 800 minutes under anhydrous and oxygen-free conditions. Three microliters were suspended on a lacey carbon TEM grid and dried in a vacuum chamber for 2 hours. When 2D sheets are observed in TEM, they are essentially transparent to the electron beam and have a constant thickness contrast throughout the particle. No Sc_2C particles were found that exhibited these properties after exfoliation. Figure A4-10a shows a low-magnification image of many Sc_2C particles, and no 2D sheets can be seen. Figure A4-10b shows a higher-magnification image of a thinner Sc_2C particle, but the thickness contrast of the particle shows a 3-dimensional "wedge" shape, rather than a 2D sheet. The diffraction patterns in Figures A4-10c and A4-10d show two sides of the same crystal, showing that the crystal domains are, on average, greater than 1 μm.

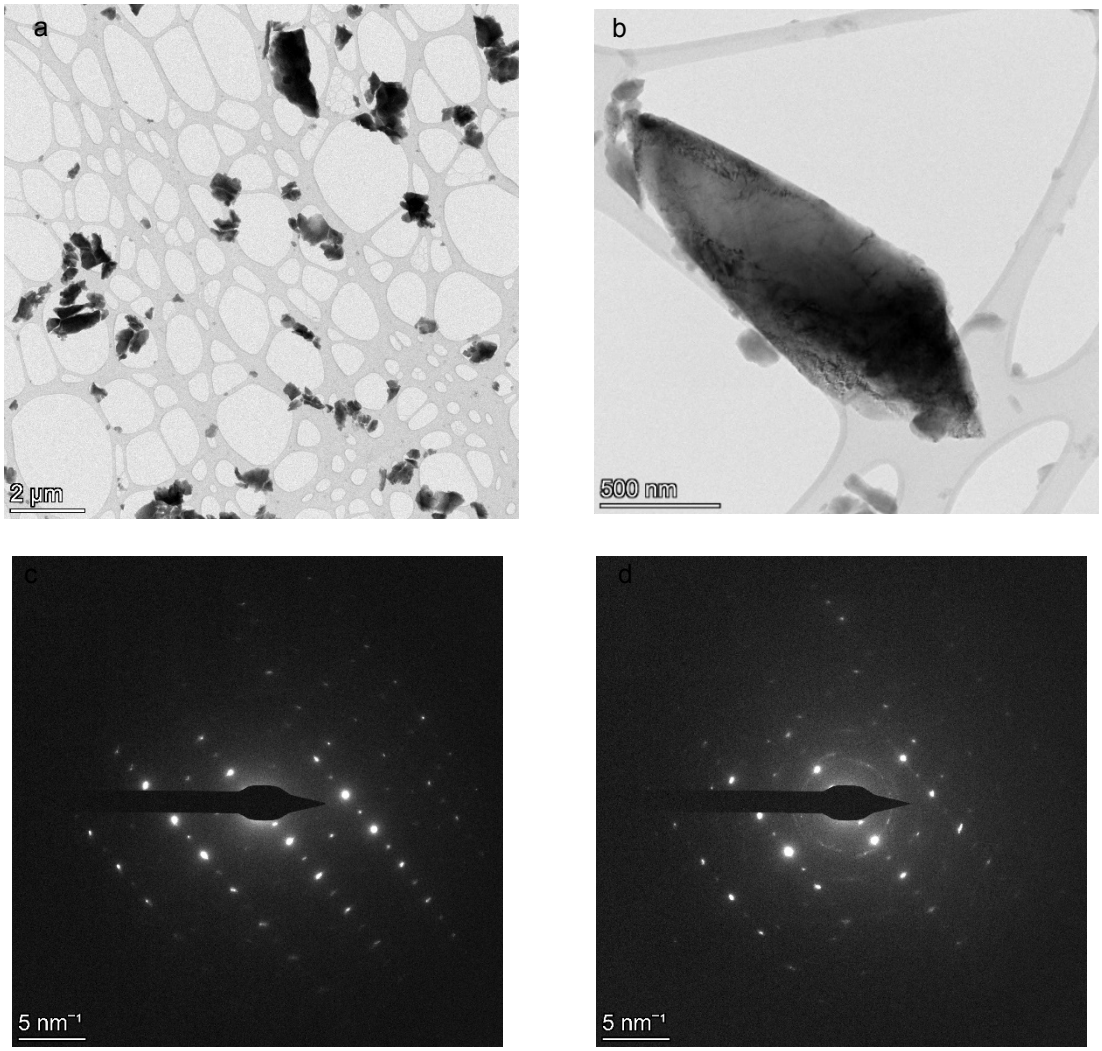


Figure A4-10. TEM images of sonication experiments.

In the main text, we explore the oxidation of Sc_2C through XPS experiments. In addition to obtaining high-resolution spectra for Sc and C, we also took spectra of oxygen after 0, 1, and 11 days of the product sitting in air (Figure A4-11). In the oxygen spectra, there are two peaks present at the initial timepoint, where the peak at 528.5 eV likely corresponds to Sc_xO_y or related species. The peak at 531.0 eV is in a binding energy region where many oxide species are possible, so we cannot associate this peak with any specific oxygen-type[7]. However, the oxygen spectrum indicates that the amount of Sc_xO_y is not changing with exposure to air, as the intensity of the peak associated with the metal oxide does not change intensity with time.

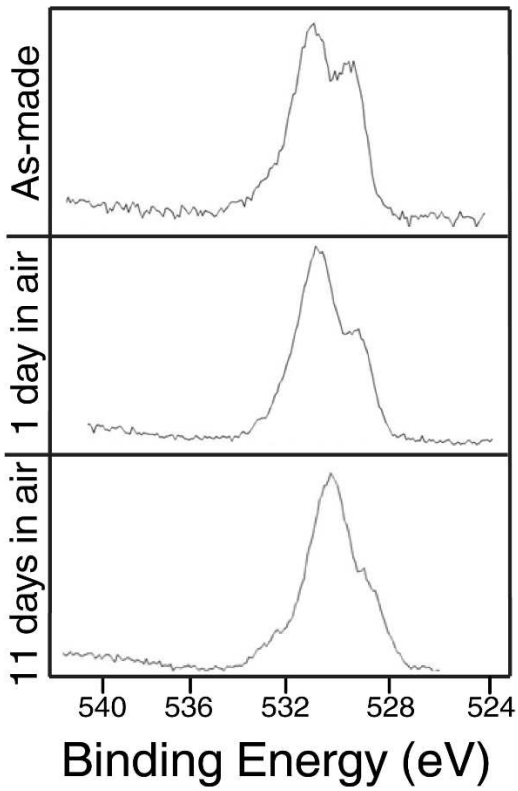


Figure A4-11. High-resolution XPS spectra of oxygen after 0, 1, and 11 days of sitting in air.

REFERENCES

(1) Rassaerts, H.; Nowotny, H.; Vinek, G.; Benesovsky, F. Zum System Scandium. *Inorg, Struct and Phys Chem* **1967**, *61*, 460–468.

(2) Langet, K.; Schreyer, W. Infrared and Powder X-Ray Diffraction Studies on the Polymorphism of Cordierite, $Mg_2(Al_4Si_5O_{18})$. *Am Mineral* **1969**, *54*, 1442–1459.

(3) Koopmans, von T. Uber Die Zuordnung von Wellenfunk-Tionen Und Eigenwerten Zu Den, Einzelnen Elektronen Eines Atoms. *Physica* **1934**, *1* (1–6), 104–113.

(4) De Jong, M.; Chen, W.; Angsten, T.; Jain, A.; Notestine, R.; Gamst, A.; Sluiter, M.; Ande, C. K.; Van Der Zwaag, S.; Plata, J. J.; Toher, C.; Curtarolo, S.; Ceder, G.; Persson, K. A.; Asta, M. Charting the Complete Elastic Properties of Inorganic Crystalline Compounds. *Sci Data* **2015**, *2*, 150009.

(5) He, Y. The Structural, Electronic, Elastic and Thermodynamics Properties of 2D Transition-Metal Electride Y_2C via First-Principles Calculations. *J Alloys Compd* **2016**, *654*, 180–184.

(6) Druffel, D. L.; Kuntz, K. L.; Woomer, A. H.; Alcorn, F. M.; Hu, J.; Donley, C. L.; Warren, S. C. Experimental Demonstration of an Electride as a 2D Material. *J Am Chem Soc* **2016**, *138* (49), 16089–16094.

(7) Dupin, J.-C.; Gonbeau, D.; Vinatierb, P.; Levasseurb, A. Systematic XPS Studies of Metal Oxides, Hydroxides and Peroxides. *Phys Chem Chem Phys* **2000**, *2*, 1319–1324.

APPENDIX: SUPPORTING INFORMATION FOR CHAPTER 5

A5.1 Band structure of Sc_2CF_2

As part of a project to explore fluorination on Sc_2C, I performed a band structure calculation on Sc_2CF_2 (Figure A5-1). The structure studied is analogous to our previously synthesized Y_2CF_2[1] and Sc_2CH_2. While we could not synthesize this product through initial experiments, we find that the band gap of this material should be 2.11 eV. Additionally, the valence band is dominated by scandium and carbon orbitals while the conduction band contains mostly scandium.

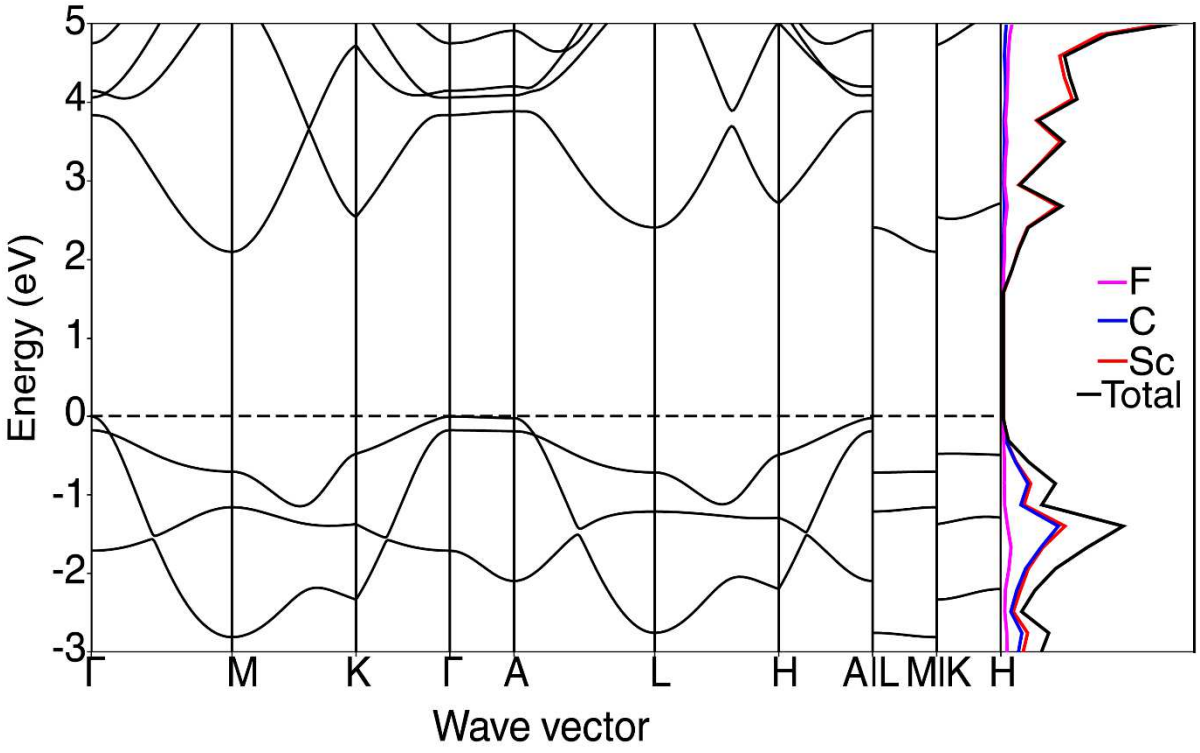


Figure A5-1. Band structure calculation of Sc_2CF_2. We find that this material is an indirect band gap semiconductor with a 2.11 eV band gap.

REFERENCES

(1) Druffel, D. L.; Lanetti, M. G.; Sundberg, J. D.; Pawlik, J. T.; Stark, M. S.; Donley, C. L.; McRae, L. M.; Scott, K. M.; Warren, S. C. Synthesis and Electronic Structure of a Crystalline Stack of MXene Sheets. *Chem Mater* **2019**, *31* (23), 9788–9796.